A Ground Experiment to Simulate a Free-floating Robot Capturing a Spacecraft

Facoltà di Ingegneria Civile e Industriale

Corso di Laurea Magistrale in Ingegneria Astronautica

Candidate

Marko Jankovic
ID number 1292565

Thesis Advisor

Prof. Fabio Curti
Dipartimento di Ingegneria Astronautica, Elettrica ed Energetica
ARCAlab

Co-Advisors

Ing. Roberto Lampariello
Jordi Artigas Esclusa
Institute of Robotics and Mechatronics
German Aerospace Center, DLR

Academic Year: 2010/2011

Thesis defended on 26 January 2012
in front of a Board of Examiners composed by:

Prof. Silvano Sgubini (chairman)
Prof. Mario Marchetti
Prof. Paolo Teofilatto
Prof. Fabio Curti
Prof. Giovanni B. Palmerini
Prof. Antonio Paolozzi
Prof. Maurizio Parisse
Prof. Augusto Nascetti
Ing. Fabio Celani
Ing. Giovanni Laneve
Ing. Susanna Laurenzi
Ing. Silvano Tizzi
Ing. Emiliano Ortore

Marko Jankovic. *A Ground Experiment to Simulate a Free-floating Robot Capturing a Spacecraft.*
Master thesis. Sapienza – University of Rome
© 2023

VERSION: 20 August 2023
EMAIL: marko.jankovic@outlook.com

I would like to dedicate this thesis to my father Ljubisa, my mother Divna and my brother Dimitrije without whom this important milestone would be impossible to accomplish and whom I will never be able to thank enough for all the support and love that I received during all this years of study.

Acknowledgment

This work is the result of six months of internship (from January to July 2011) at the Institute of Robotics and Mechatronics of the German Aerospace Center (DLR) in Oberpfaffenhofen, Germany.

Therefore, I would like first of all to express my greatest gratitude to Ing. Roberto Lampariello, my co-advisor and supervisor at DLR, and Prof. Fabio Curti, my advisor, for giving me the opportunity to participate and give my modest contribution to the DEOS project with this thesis. I would also like to thank them for their patience and countless meetings whenever I needed assistance and guidances during my internship.

I wish to turn my most sincere thanks also to Jordi Artigas Esclusa for his assistance and support without which the completion of the work presented in this thesis would be impossible.

My thanks and appreciation also goes to Marco De Stefano a true friend and adventure companion at DLR. His help and continuous support were essential to me not only during my stay in Germany but also during my studies at Scuola di Ingegneria Aerospaziale.

A special thank of mine goes to all the friends that I made in Germany whose friendship, hospitality, knowledge, and wisdom have made my stay abroad enjoyable and inspiring. Some of them are: Giuseppe Parrella, Stefano Caizzone, Valentina Catalano , Matteo Pradini, Christian Nissler, Karan Sharma and Genny Scalise.

I would also like to express my greatest gratitude to the family Gerbecks that welcomed me as a family member and made me fill at home.

I must acknowledge as well the many friends, colleagues, students, professors and employees of the faculty who assisted, advised and supported my studies for all these years.

Finally, I would like to sincerely thank my parents Ljubisa and Divna Jankovic and my brother Dimitrije for their continuous support and inspiration.

Acknowledgment

Without them I would not be the person who I am today.

Marko Jankovic, Pesaro

Abstract

The dynamic coupling between the manipulator and its base, considered to be free-floating in the microgravity environment, could lead to a different position of its end-effector compared to that of a structurally similar fixed-based robot, for the same joint input command. Therefore, to ensure the successful completion of a challenging in-orbit task, such as the capture maneuver of a target spacecraft, the verification on ground of the planning and control algorithms of the robotic system proves to be necessary. In this respect, the following thesis presents the ground simulation facility developed at the DLR Institute of Robotics and Mechatronics able to simulate the motion of a robot in space relative to a tumbling target spacecraft. The system was particularly designed having in mind the requirements of the Deutsche Orbitale Servicing Mission (DEOS). The laboratory setup is based on a hybrid method which combines the virtual model of the free-floating system with the real hardware, composed of two Light-Weight Robots (LWRs) fixed to a rigid platform. This way, the dynamical behavior of the whole system is simulated using appropriate dynamic models, while the physical motions of the space manipulator and client satellite are accomplished by two LWRs. The emulation of the free-floating base is performed through the motion of the target spacecraft based on its relative position with respect to the servicer satellite. This way, the developed laboratory simulator provides, on ground, an environment similar to what an astronaut or a remote operator would observe form the servicer spacecraft during the capture maneuver. Moreover, the system proves to be extendible by small hardware and software modifications and to be relatively simple and cheap in contrast to laboratory setups currently being developed around the world for the same task.

Riassunto

L'accoppiamento dinamico tra il manipolatore e la sua base, considerata mobile nell'ambiente di microgravità, potrebbe portare ad una posizione diversa del suo organo terminale rispetto a quello di un manipolatore strutturalmente simile a base fissa, per lo stesso comando di input ai giunti. Pertanto, per garantire il successo di un compito impegnativo in orbita, come ad es. la manovra di cattura di un veicolo bersaglio, la verifica a terra degli algoritmi di pianificazione e controllo del sistema robotico si rivela necessaria. A tal proposito, la seguente tesi presenta l'impianto di simulazione sviluppato presso l'Istituto di Robotica e Meccatronica del DLR in grado di simulare il moto relativo di un robot nello spazio rispetto ad un veicolo bersaglio in avaria. Il sistema è stato particolarmente progettato avendo a mente i requisiti della Deutsche Orbitale Servicing Mission (DEOS). Il setup di laboratorio si basa su un metodo ibrido che combina il modello virtuale del sistema flottante con l'hardware vero e proprio, composto di due Light-Weight Robot (LWR) fissati ad una piattaforma rigida. In questo modo, il comportamento dinamico di tutto il sistema è simulato utilizzando appropriati modelli dinamici, mentre i movimenti fisici del manipolatore spaziale e del satellite cliente sono eseguiti dai due LWR. L'emulazione della base flottante è eseguita attraverso il movimento del veicolo bersaglio in base alla propria posizione relativa rispetto al satellite di servizio. In questo modo, il simulatore sviluppato realizza a terra un ambiente simile a quello che un astronauta o un operatore remoto osserverebbe dal satellite di servizio durante la manovra di cattura. Inoltre, il sistema dimostra di essere estensibile con delle piccole modifiche hardware e software e di essere relativamente semplice e poco costoso rispetto ai setup di laboratorio attualmente in fase di sviluppo in tutto il mondo per la stessa funzione.

Contents

List of Figures

List of Tables

Nomenclature

Acronyms

A&R	*Automation and Robotics*
ADR	*Active Debris Removal*
AOCS	*Attitude and Orbit Control System*
ARAMIS	*Automation, Robotics, and Machine Intelligence Systems*
ASAT	*Anti-Satellite Weapon*
ASTRO	*Autonomous Space Transport Robotic Operations*
CAD	*Computer Aided Design*
CFRP	*Carbon Fiber Reinforced Polymer*
c.g.	*Center of Gravity*
c.m.	*Center of Mass*
COPUOS	*United Nations Committee on the Peaceful Uses of Outer Space*
DARPA	*Defense Advanced Research Projects Agency*
DEBIE	*Debris In-Orbit Evaluator*
DEOS	*Deutsche Orbitale Servicing Mission*
DLR	*Deutsches Zentrum für Luft- und Raumfahrt e.V. - German Aerospace Center*
DOF	*Degrees Of Freedom*

ETS	*Engineering Test Satellite*
EVA	*Extra-Vehicular Activity*
FEA	*Fnite Element Analysis*
GEO	*Geostationary Earth Orbit*
GETEX	*German Technology Experiment on ETS-VII*
GPS	*Global Positioning System*
HIL	*Hardware-In-the-Loop*
HMI	*Human Machine Interface*
HMI2010	*Human Machine Interface 2010*
HST	*Hubble Space Telescope*
HTV	*H-II Transfer Vehicle*
IAA	*International Academy of Astronautics*
IADC	*Inter-Agency Space Debris Coordination Committee*
IRMC	*Institute of Robotics and Mechatronics*
ISO	*International Organization for Standardization*
ISS	*International Space Station*
JAXA	*Japan Aerospace Exploration Agency*
JEM	*Japanese Experiment Module*
JEMRMS	*Japanese Experiment Module Remote Manipulator System*
LDEF	*Long Duration Exposure Facility*
LED	*Light Emitting Diode*
LEGEND	*LEO-to-GEO Environment Debris model*
LEO	*Low Earth Orbit*
LIDAR	*Light Detection and Ranging or Laser Imaging Detection and Ranging*

Li-ion	*Lithium-ion*
LWR	*Light Weight Robot*
LWR	*Light-Weight Robot*
MBS	*Mobile Base System*
MDA	*MacDonald, Dettwiler and Associates Ltd.*
MIT	*Massachusetts Institute of Technology*
MSFC	*Marshall Space Flight Center*
NASDA	*National Space Development Agency*
NEXTSat	*Next Generation Serviceable Satellite*
OBSS	*Orbiter Boom Sensor System*
OE	*Orbital Express*
OOS	*On-Orbit Servicing*
ORU	*Orbital Replacement Unit*
PD	*Proportional-Derivative (control)*
PMD	*Post-Mission Disposal*
R.U.R	*Rossum's Universal Robots*
RADAR	*Radio Detection And Ranging*
RF	*Radio Frequency*
ROKVISS	*Robotic Components Verification on the ISS*
RORSAT	*Radar Ocean Reconnaissance Satellite*
ROSCOSMOS	*Russian Federal Space Agency*
ROTEX	*Robot Technology Experiment*
RTFX	*Ranger Telerobotic Flight Experiment*
RTSX	*Ranger Telerobotic Shuttle Experiment*
S/A	*Solar Array*

SIS	*Space Infrastructure Servicing*
SM^2	*Self-Mobile Space Manipulator*
SPDM	*Special Purpose Dexterous Manipulator*
SRMS	*Shuttle Remote Manipulator System*
SSN	*Space Surveillance Network*
SSRMS	*Space Station Remote Manipulator System*
STSC	*Scientific and Technical Subcommittee*
UN	*United Nations*
US	*United Stations*
VES	*Vehicle Emulation System Model*

Roman Symbols

$\boldsymbol{c}_b$	Nonlinear Coriolis and centrifugal forces of the base
$\boldsymbol{c}_m$	Nonlinear Coriolis and centrifugal forces of the manipulator
$\boldsymbol{e}$	Pose error between the end-effectors of the chaser and target robots, $[\mathrm{m};\mathrm{rad}]$
$\boldsymbol{F}_b$	External forces and moments exerted on the centroid of the base, $[\mathrm{N};\mathrm{N}\cdot\mathrm{m}]$
$\boldsymbol{F}_c$	Generalized control force applied to the end-effector, $[\mathrm{N};\mathrm{N}\cdot\mathrm{m}]$
$\boldsymbol{F}_e$	External forces applied on the centroid of the target satellite, $[\mathrm{N}]$
$\boldsymbol{F}_h$	External forces and moments exerted on the end-effector of the manipulator, $[\mathrm{N};\mathrm{N}\cdot\mathrm{m}]$
$\boldsymbol{F}_{max}$	Maximum generalized control force applied to the end-effector, $[\mathrm{N};\mathrm{N}\cdot\mathrm{m}]$
$\boldsymbol{g}$	Standard gravity acceleration vector, $[\mathrm{m/s^2}]$
$\boldsymbol{H}_b$	Inertia matrix of the base, $[\mathrm{kg}\cdot\mathrm{m}^2]$

$\boldsymbol{H}_{bm}$	Coupling inertia matrix between the base and the manipulator, $[\mathrm{kg} \cdot \mathrm{m}^2]$
$\boldsymbol{H}_m$	Inertia matrix of the manipulator, $[\mathrm{kg} \cdot \mathrm{m}^2]$
$\boldsymbol{I}$	Moment of inertia matrix, $[\mathrm{kg} \cdot \mathrm{m}^2]$
I_0	Moment of inertia about the x and y axis of a symmetrical body, $[\mathrm{kg} \cdot \mathrm{m}^2]$
I	Moment of inertia about the z axis of a symmetrical body, $[\mathrm{kg} \cdot \mathrm{m}^2]$
$\boldsymbol{I}_n$	Identity matrix
$\boldsymbol{I}_{sat}$	Inertia matrix of the satellite, $[\mathrm{kg} \cdot \mathrm{m}^2]$
$\boldsymbol{J}$	Jacobian matrix of the manipulator
$\boldsymbol{J}_b$	Jacobian matrix dependent on the base motion
$\boldsymbol{J}_m$	Jacobian matrix dependent on the motion of the manipulator
$\boldsymbol{J}^\dagger$	Right pseudo-inverse Jacobian of the manipulator

$\boldsymbol{K}_d$	Derivative gain of the PD control
$\boldsymbol{K}_p$	Proportional gain of the PD control
$\boldsymbol{L}$	Angular momenum vector, $[\mathrm{N} \cdot \mathrm{m} \cdot \mathrm{s}]$
$\mathcal{L}$	Lagrangian of a dynamical system
$\boldsymbol{M}$	Vector of external moments, $[\mathrm{N} \cdot \mathrm{m}]$
m_{sat}	Mass of the satellite, [kg]
m	Mass of a body, [kg]
$\boldsymbol{M}_e$	External moments applied on the centroid of the target satellite, $[\mathrm{N} \cdot \mathrm{m}]$
P_r	Reflected power, [W]
${}^k\boldsymbol{p}_{ij}$	Position vector from the origin of the reference frame Σ_i to that of Σ_j, with respect to the frame Σ_k, [m]

${}^{i}\boldsymbol{p}_{cm_i \to j}$	Position vector from the origin of the reference frame Σ_i, centered in the cm of the link i, to that of Σ_j, centered in the joint j, with respect to the frame Σ_i, [m]
${}^{i}\boldsymbol{p}_{i \to cm_i}$	Position vector from the origin of the reference frame Σ_i, centered in the joint i, to the cm of the link i, with respect to the frame Σ_i, of the joint, [m]
$\boldsymbol{p}_{sat}$	Absolute position of the body reference frame of the satellite, [m]
$\boldsymbol{q}$	Vector of joint variables of the space manipulator, [rad]
q_i	Generalized coordinate of a dynamical system
$\boldsymbol{q}_c$	Vector of joint angles of Robot C, [rad]
$\boldsymbol{q}_d$	Desired vector of joint angles, [rad]
q_{iM}	Maximum joint limit, [rad]
q_{im}	Minimum joint limit, [rad]
$\bar{q}_i$	Middle value of the joint range, [rad]
$\boldsymbol{q}_m$	Measured vector of joint angles, [rad]
$\boldsymbol{q}_t$	Vector of joint angles of Robot T, [rad]
R	Range, distance form the transmitter to the target, [m]
${}^{i}\boldsymbol{R}_j$	Rotation matrix of the frame Σ_j with respect to the frame Σ_i
$\mathcal{T}$	Kinetic energy of a body, [J]
${}^{i}\boldsymbol{T}_j$	Homogeneous transformation matrix describing the pose of the frame Σ_j with respect to the frame Σ_i
$\mathcal{V}$	Potential energy of a body, [J]
$w(\boldsymbol{q})$	Secondary objective function of the joint variables
${}^{0}\boldsymbol{x}_1$	Absolute position and orientation vector of the base, [m; rad]
${}^{0}\boldsymbol{x}_2$	Absolute position and orientation vector of the target spacecraft, [m; rad]

$\boldsymbol{x}_b$	Position and orientation vector of the centroid of the base, [m; rad]
$\boldsymbol{x}_e$	Position and orientation vector of the end-effector, [m; rad]
$\boldsymbol{x}_{sat}$	Absolute pose of the body reference frame of the satellite, [m; rad]

Greek Symbols

$\boldsymbol{\alpha}$	Parameter of the PD controller for the fine tunning
${}^1\boldsymbol{\phi}_2^1$	Orientation vector of the reference frame Σ_1 to that of Σ_2, expressed in Σ_1, [rad]
$\boldsymbol{\omega}$	Angular velocity vector, [rad/s]
ϕ	Angle of precession, [rad]
$\boldsymbol{\phi}_{sat}$	Absolute orientation of the body reference frame of the satellite, [rad]
ψ	Angle of rotation, [rad]
Σ_i	Reference frame i
$\boldsymbol{\tau}_0$	Additional control torque, $[\mathrm{N} \cdot \mathrm{m}]$
$\boldsymbol{\tau}_c$	Vector of control joint torques of the manipulator, $[\mathrm{N} \cdot \mathrm{m}]$
$\boldsymbol{\tau}_c^{'}$	Vector of control joint torques of the manipulator generated by the admittance controller, $[\mathrm{N} \cdot \mathrm{m}]$
θ	Angle of nutation [rad]
$\boldsymbol{\tau}_m$	Vector of joint torques of the manipulator, $[\mathrm{N} \cdot \mathrm{m}]$

Introduction

Fifty years after the launch of Sputnik 1, satellites have become an integral part of human society powering numberless services like cell phones, television, weather forecasting, navigation, unprecedented astronomical observations and better understanding of our home planet. Although they are taken largely for granted these modern devices are constantly in danger, due to potential collisions with a growing number of debris left by decades of space exploration. Just as human activities on Earth generate mountains of waste, the increasing number of lunches performed every year has created growing amounts of debris that are in constant danger of colliding with active satellites and interrupting the services that we greatly depend on.

In May 1998, the malfunctioning of a single satellite abruptly cut off communications services in North America, silencing about 40 million pagers, blocking automated teller machines and credit card payments, and forcing radio and television networks off the air [1].

Space debris has rapidly evolved from science fiction's subject to a serious problem for the functioning satellites, as well for the human space activity. In fact, the International Space Station (ISS), the Space Shuttle Orbiter and many commercial satellites were often obliged to carry out orbital maneuvers to avoid collisions with the incoming space junk and to include heavy debris shields around the sensitive equipment and manned modules.

In almost 50 years of space activities, approximately 4 900 launches have placed all man-made objects into orbit, of which only eleven are responsible for 32 % of all detectable fragmentation debris.

There would be no such risk of collisions, or at least it would be significantly smaller, if only the operational satellites were on orbit. We need to consider that they have to share space with thousands of abandoned or nonfunctional satellites, spent rocket upper stages and with millions of debris objects of all sizes, traveling at speeds of roughly 10 km/s. Indeed, more than 12 000 objects, with the diameter larger than 10 cm in low Earth orbit (LEO, i. e. the region from the beginning of the space environment up to an altitude of 2 000 km) and 1 m in geosynchronous Earth orbit (GEO, i. e. a geosynchronous orbit 35 786 km above the equator), are regularly tracked by the United States (US) Space Surveillance Network (SSN) and maintained in their catalogue. Of that number only 6 % represents the operational population of spacecrafts, while the remaining 94 % is made up decommissioned satellites, mission-related objects and on-orbit fragmentations that have occurred since 1961 [2].

The emerging space debris problem has concerned the international space community since the early stages of space exploration. Many studies and policies have been developed world wide to address this issue being the global dimension of the problem internationally recognized. For example in 2008 countries at the United Nations (UN) adopted space debris mitigation guidelines to limit the debris released in outer space and promote international consensus on acceptable spacecraft operations so that outer space may be used in a sustainable way [1]. However at altitudes above the levels where atmospheric drag is significant, the time required for orbital decay may require centuries or millennia. In particular in LEO recent numerical studies indicate that the density of the debris populations has reached a critical point where it will continue to increase exponentially even if all future launches are suspended. This self-sustained process caused by the increased mutual collisions among orbiting objects, which is particularly critical for the LEO region, is known as the *Kessler syndrome* [3, 4].

In reality the break-up of the Fengyun-1C spacecraft (i. e. the Chinese anti-satellite demonstration) in 2007, at an altitude of 862 km, and the collision between the defunct Russian satellite Kosmos 2251 and the operational US satellite Iridium 33, at an altitude of 789 km, have greatly increased the number of orbiting fragments confirming that in the near future, even with a full implementation of currently proposed mitigation measures, the growth of space debris in LEO appears to be inevitable.

To mitigate this kind of instability, various measures have been adopted and proposed by international organizations. However all of them prove to be inefficient because the only effective long-term means of stabilizing the space debris environment is through the concept of active debris removal (ADR) or through the concept of on-orbit servicing (OOS) of spacecrafts. Studies suggest that removing five to ten large objects per year from the LEO region can prevent the Kessler syndrome and preserve the near-Earth environment for future space generations [3, 4]. Ideally each satellite could perform a controlled de-orbit at the end of its life although in reality this practice is sometimes impossible or not cost-effective. Rolling out an electrodynamic tether from a spacecraft or augmenting its frontal area by inflating special surfaces is one idea to decrease the perigee of an orbit. But another more effective idea is a robotic re-orbit or de-orbit. These concepts aren't new but in the past any effort to actively remove debris from the orbit always had a risk of creating more debris than it could be cleaned up. Other issues, such as ownership, policy, and liability, also prevented ADR from being seriously considered in the past but now, given the current situation, this option is more and more reconsidered by the international space community [5].

A good example of a changing policy in space environment is the recent agreement between Intelsat S. A. and MacDonald, Dettwiler and Associates Ltd. (MDA) for servicing Intelsat's satellites via the Space Infrastructure Servicing (SIS) vehicle to be provided by MDA. The SIS vehicle is expected to be the precursor of the OOS concept, performing not only the on-orbit refueling, but also some critical maintenance and repair tasks, such as releasing jammed deployable arrays and stabilizing or even removing smaller space objects or debris [6]. This approach can replace the disposable character of today's geosynchronous satellites paving the way to a reusable kind of future spacecrafts that can be reconfigured or refueled in orbit. This way their operational lifetime would be extended leading to a more sustained use of outer space.

Within this context the German Aerospace Center (Deutsches Zentrum für Luft- und Raumfahrt e.V. - DLR) is developing an on-orbit servicing technology demonstration mission Deutsche Orbitale Servicing Mission (DEOS). The primary goal of this mission is the capture, with the on-board manipulator, and a controlled de-orbit of a tumbling and non-supportive client satellite in low Earth orbit. Both spacecrafts, named Client and Servicer (or Target and Chaser), will be injected together into an initial orbit by the same launcher. Starting with the mated configuration the complexity of the experiments will be stepwise increased over one year mission period.

In this respect, this thesis proposes an experimental approach to simulate a free-floating manipulator capturing a space target using two innovative Light Weight Robots (LWRs) of third generation. Made having in mind the human arm, LWR manipulator has seven degrees of freedom (DOF) resulting in advanced flexibility and dexterity in comparison to standard industrial robots used in the past to develop similar laboratory simulators [7, 8, 9]. The fundamental idea is to use a method which combines the mathematical model of the dynamic system with the physical model of manipulators. This means that the dynamical behavior of the whole system (i. e. manipulator, it's base and the target) is simulated using appropriate algorithms and software while the motion of the end-effector of the free-floating manipulator and of the target is accomplished by precise movements of the LWRs. The proposed method was used to evaluate more realistically the control algorithms developed for the free-floating manipulator [10] as well as to underline the limits of this kind of simulator. Indeed the performance of proposed space robotic systems can be greatly deteriorated due to the dynamic coupling between space manipulator and its base. As a result the end-effector of the free-floating manipulator could exhibit a completely different motion of the one mounted a top of a fixed base leading to failure of the mission, i. e. the capture of the space target.

Structure of the thesis

The structure of the thesis consist of four chapters and two appendices. Each chapter is introduced by a brief preamble providing the background of the presented study and the summary of the chapter itself. The appendices have the purpose to provide the reader with details regarding the topics presented in the main text.

Chapter 1 introduces the concepts of on-orbit servicing and active debris removal as the only effective solutions to the growing number of space debris objects in orbit around the Earth. In the first part of the chapter, the problem of the space debris is illustrated, starting from its origins, continuing with the number of objects and their distribution in space and concluding with the brief description of the current mitigation measures and the long-term projections of the number of objects. The second part of the chapter examines the concept of orbital robotics by describing its historical background and future implementations that could eventually lead to the concept of a reusable spacecraft and help to maintain the space debris population at a safe level for future space operations.

Chapter 2 describes the Deutsche Orbitale Servicing Mission (DEOS) and the methods that could be used to perform the simulation of the mission on ground. To accomplish that, the first part of the chapter is dedicated to the overview of the mission. Particular attention is given to the specifications of the two spacecrafts along with the description of the robotic arm of the Servicer's Automation and Robotics payload. The second part of the chapter analyzes microgravity simulation methods on ground, necessary to evaluate control and planning algorithms of the manipulator, thus avoiding in orbit system performance degradation due to the dynamic interaction between the manipulator and its base spacecraft. The examined simulation methods include air beatings, neutral buoyancy, parabolic flights, drop facilities and suspension systems. Within this context, the suspended rotating platform is considered as a possible way to simulate the motion of a tumbling spacecraft. Finally, the robotic simulation system is described evidencing among the possible realization modes the one used at the DLR Institute of Robotics and Mechatronics (IRMC).

Chapter 3 deals with the realization process of the robotic ground setup based on the existing multimodal haptic Human Machine Interface (HMI). Therefore, an overview of the developed system, composed of two Light-Weight Robots fixed to the rigid platform opens the chapter. Subsequently, the dynamic equation of the free-floating robot is analyzed and the virtual models of the DEOS Chaser spacecraft are introduced. Than, the realization of the Simulink model of the system is tackled, evidencing two possible control schemes. In the end, the development of the new optimized mockup of the target satellite is described.

Chapter 4 illustrates the numeric simulations performed to test the ability of the ground setup, before any use of the real hardware, to emulate the free-floating behavior of the space manipulator, during the approach phase, and evidence its limits. With this aim, the first part of this chapter is dedicated to the general description of the performed simulations while the second part describes in detail the characteristics of the single simulations and their relative results. In particular, three set of simulations were performed based on the relative motion of the manipulator with respect to the body frame of the base and on the models used to emulate the dynamic coupling between the manipulator and its base.

Chapter 5 is dedicated to the experimental validation of the ground-based, hardware-in-the-loop, space-robot simulation facility. To this end, the section entitled "Cause and Objective" introduces the reader to this chapter by explaining the necessity and the purpose of the experimental validation process. Next, the basic setup of the robotic hardware-in-the-loop system is described. In particular, the mechanical configuration and the control architecture of the facility are outlined. Detailed description of the performed test cases is addressed in the following section. In the end, the validation criteria is defined and the results of the test cases are evaluated according to the established criteria.

Appendix A is devoted to the detailed description of the inertial parameters of the chaser spacecraft, used for the development of its numerical models. As in Chapter 3, two different sets of parameters are considered based on the type of the manipulator mounted on the base satellite. Moreover, various mass cases of the carrier spacecraft are presented depending on weather its dimensions are considered fixed or variable.

Appendix B presents the technical drawings of the mockup models developed during the study mentioned in Chapter 3. The drawings are developed using the 3D mechanical computer-aided design program, SolidWorks.

Appendix C describes in detail the procedures and precautions that are necessary to follow in order to correctly start up the robotic hardware-in-the-loop system and perform a simulation of the approach phase of the DEOS mission.

1 Space Robotics: Active Debris Removal and On-Orbit Servicing

Currently the number of space debris resulting form fragmentation of in-orbit artifacts dominate over the natural flux of meteoroids. In a *business-as-usual* scenario in few decades the mutual collisions will increase exponentially the number of fragments creating a belt of debris around the Earth [11, 2]. To prevent this a set of mitigation guidelines and more costly active debris removal (ADR) concepts must be implemented. At present the most efficient way to achieve this is using robotic systems.

This chapter is structured as follows: Section 1.1 illustrates the problem of space debris describing its origins, distribution and the future trend. Section 1.2, on the other hand, examines the concept of orbital robotics illustrating its historical background and future implementations such as on-orbit servicing (OOS) and active debris removal (ADR).

1.1 Space Debris

1.1.1 Historical background

More than half a century of space flight exploration, since October 4, 1957, has generated a significant amount of non-functional man-made earth-orbiting objects denoted as: *space debris*. Term that indicates, according to an internationally accepted definition developed by the International Academy of Astronautics (IAA), [12]:

> Any man-made earth-orbiting object which is non-functional with no reasonable expectation of assuming or resuming its intended function or any other function for which it is or can be expected to be authorized, including fragments and parts thereof.

The first ever origin of space debris occurred in June 1961 with the explosion of the Ablestar upper stage of the rocket Thor-Ablestar increasing instantaneously the total debris population by more than 400 %. Since than the fragmentation (unintentional or intentional) of in-orbit objects have been the major origin of all catalogued debris. Approximately 50 % of the catalogued space debris population emerged from few collisions and about 200 in-orbit explosions of discarded rocket bodies, fuel tanks or battery packs. Moreover, about 25 % of the catalogued in-orbit items are active and inactive payloads, about 13 % are spent rocket bodies and the remaining 12 % are mission-related debris.
Other important debris sources were [2]:

- 16 reactor core ejections from BUK reactors of Russian Radar Ocean Reconnaissance SATellite (RORSAT) during which approximately 128 kg of a low-melting sodium potassium alloy ($\mathrm{NaK} - 78$) escaped from the primary coolant system generating a multitude of dangerous droplets in the 1980s;
- more than 1 000 solid rocket motor firings, which released aluminum oxide (Al_2O_3) in the form of micrometer-sized dust and mm- to cm-sized slag particles;
- the first-ever accidental in-orbit collision, in 2009, between the defunct Russian satellite Kosmos 2251 and the operational US satellite Iridium 33, at an altitude of 789 km. As they collided, at a relative speed of 11.7 km/s, they were both disintegrated and furthermore the collision generated a large amount of debris.

In addition to the previously unintentional events recent chinese anti-satellite weapon test (ASAT), in 2007, alone increased by one-third the population debris which had taken 50 years to accumulate. Although there were previous ASAT test in the 1980s, conducted by US and former Soviet Union, this event is considered the worst single fragmentation event in the history of the space age. The disintegration of the Fengyun-1C spacecraft took place at an altitude of 860 km, region considered to be the most densely populated with satellites [13]. Figure 1.1 proves this statement since it is clearly visible the substantial increase of catalogued objects corresponding to the year 2007. Other visible instantaneous growths of the number of cataloged objects are due to the intentional destruction of malfunctioning American spy satellite USA-193 in 2008 and the collision between Kosmos 2251 and Iridium 33 satellites.

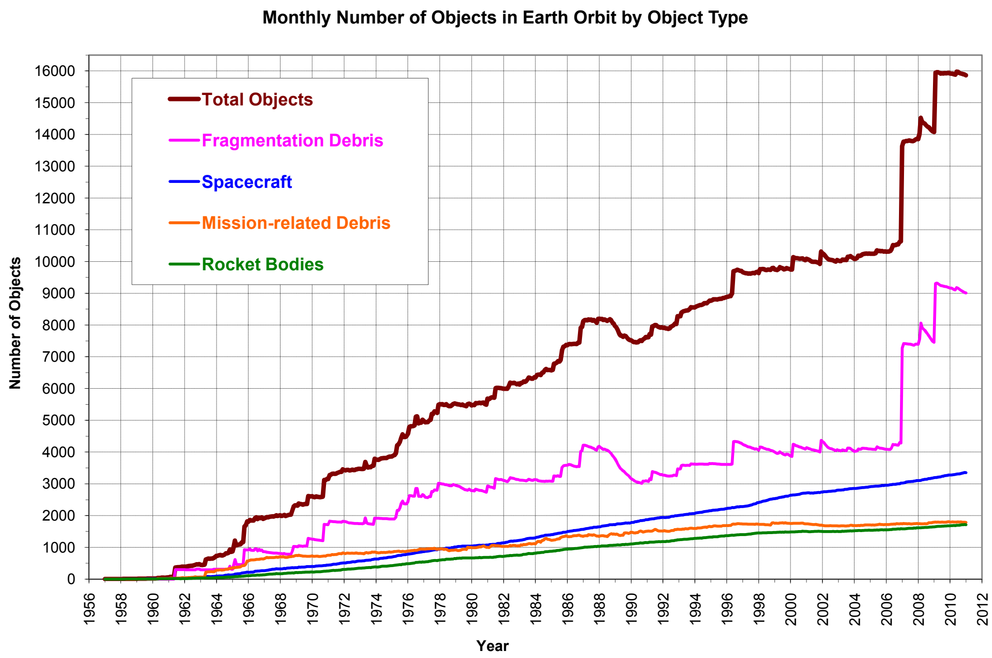

Figure 1.1: Monthly number of cataloged objects in orbit [14]

Table 1.1: Estimated population of space debris objects [2]

Size	Number of objects	Potential risk to satellites
$>$ 10 cm	20 000	Complete destruction
1-10 cm	60 000	Complete/partial destruction
$<$ 1 cm	300 million	Locale damage/degradation

1.1.2 Number of objects and their distribution

Since the start of the space age around 6 000 satellites have been injected into orbit resulting form 4 800 launches. As of February 20, 2009 only a minor fraction of these satellites, around 13 % (with a total mass of about 5 500 t), are still operational. On the other hand those 800 intact spacecrafts represent only 6 % of 12 500 objects that are daily tracked by the US Space Surveillance Network (SSN). Furthermore 38 % of catalogued objects is made of decommissioned satellites, spent upper stages and various mission-related objects. The remaining 56 % has its origin form 200 in-orbit explosions recorded since the dawn of the space era. Nevertheless these objects are just the tiny cataloged portion of the whole space debris population, indicated in Table 1.1. Generally the dimensions of catalogued objects are restricted to 5 to 10 cm in low Earth orbit (LEO) and 30 cm to 1m in geostationary Earth orbit (GEO).

Space debris catalogues are generally limited to larger objects, typically greater than 10cm in LEO and greater than 1m in GEO. This limited capacity is due to a compromise between system cost of space surveillance networks and their performance. RADAR measurements are most suitable for observations in LEO, below 2 000 km, since the reflected power from space debris is inversely proportional to the fourth power of its distance or in this case altitude: $P_r \simeq 1/R^4$. Telescopes on the other hand are mainly suited for GEO and high-altitude debris observations given that the incident illumination is essentially independent of the altitude and the reflected power is inversely proportional to the square of the distance on the contrary form the radar measurements: $P_r \simeq 1/R^2$. Information about the population of few mm in size is given or in statistical manner or through analysis of spacecraft surfaces brought back from space or through in-situ impact detectors like Long Duration Exposure Facility (LDEF) or Debris in-Orbit Evaluator (DEBIE) [2].

From a statistical point of view most of the mentioned orbital debris resides within 2 000 km of the Earth's surface (i. e. in LEO) as it can be noticed in Figure 1.2. Within this volume debris concentrations varies greatly with altitude although the altitudes of 800, 900 km, and near 1 400 km present the peak of the maximum spatial density equal to 3×10^{-8}, 2×10^{-8}, 1.5×10^{-8} objects/km^3 respectively [15]. Furthermore the region from 600 to 1 000 km has also the highest mass distribution. In particular the altitude of 600 km is dominated by spacecrafts while the regions around 800 and 1 000 km are dominated by spent rocket bodies, as it could be aspected.

In LEO objects are continuously exposed to aerodynamic forces that extracts their orbital energy causing the continuous reduction of their altitude and finally their re-entry in Earth's atmosphere. Depending on the altitude and on the air density, driven mainly by the Sun's activity, the re-enter will occur after a few weeks, years or even centuries. At higher altitudes, i. e. above 800 km, air drag becomes less effective causing the objects to remain for many decades. The result is the chaotic situation illustrated in Figure 1.3. Considering that the depicted situation represents only 1.5 % of the orbits catalogued by the US SSN, the protection of a spacecraft, besides shielding it and performing collision avoidance maneuvers, means mainly to rely on statistical data and pure chance, hoping that the orbital objects will not collide.

The collision assessments have become an extremely important aid in the design of manned and unmanned spacecraft since they can indicate the proper placement of critical subsystems and protective shielding. Table 1.2 highlights the studies made in this field indicating, in particular, the mean time elapsing between two impacts on a 100 m^2 satellite (e. g. a satellite with solar panels, or a

Figure 1.2: Distribution of catalogued objects in space based on actual density data [2]

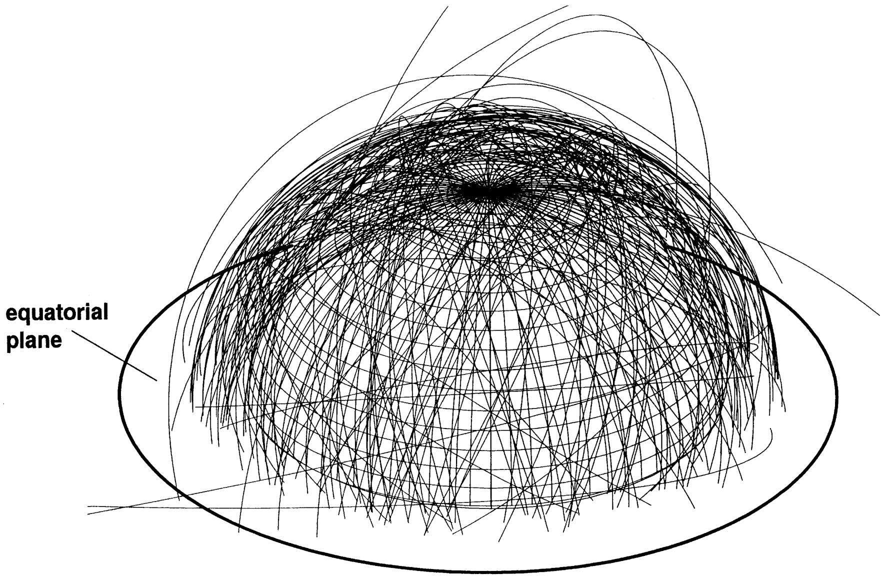

Figure 1.3: 1.5 % of LEO orbits occupied by objects larger than 10 cm [12]

Table 1.2: Mean time intervals between collisions [12]

Circular orbit altitude	Objects size		
	0.1-1 cm	1-10 cm	>10 cm
500 km	1-10 years	350-700 years	15 000 years
1 000 km	0.3-3 years	70-140 years	2 000 years
1 500 km	0.7-7 years	100-200 years	3 000 years

module of ISS) at different orbital altitudes. Choosing for example the altitude of 1 000 km and the 1 cm size object the probability of a 100 m^2 satellite being hit, and destroyed, is about 10 % within its 10-year mission [12]. Hence for the time being the risk of in-orbit collision in LEO is not extremely high, but it should not be forgotten that this risk has been greatly increased by two recent events: the 2007 break-up of the Fengyun-1C spacecraft and the 2009 collision between two satellites.

In GEO and near the orbits of navigation satellite constellations the spatial density is much smaller, generally by two to three orders of magnitude than the one in LEO. Nevertheless since at those altitudes the Earth's atmosphere has almost no effect on debris' orbital energy all objects placed or generated, through fragmentation, will accumulate and stay there for ever. This explains why these regions are so highly sensitive to permanent overcrowding. In particular if ever the geostationary orbit were to become highly overpopulated by space debris it would be lost for ever since the collision risk, to whom the satellites would be exposed, would be to high. The risk assessment situation at these altitudes is more complicated since the exact number of space debris with diameter of less than 1 m is unknown. Moreover, since there is no natural removal mechanism for satellites generally it is assumed that an annual collision probability of 10^{-5} between an average operational satellite and other catalogued objects.

1.1.3 Mitigation measures and long-term perspective

Half a century ago the near-Earth space seemed limitless. Nevertheless, in relatively short amount of time, the orbits around the Earth got overcrowded. The rising probability of mutual collision forced the spacefaring nations to recognize the global nature of the problem. It became evident that the only way to ensure safe future space flights is through international cooperation. To address the issue many policies and procedures were established while others are currently matter of study. Debris mitigation principles were first put into practice by the

US in the 1980s. Other countries and organizations followed, including various space agencies like the European Space Agency (ESA), the Russian Federal Space Agency (ROSCOSMOS), Japan Aerospace Exploration Agency (JAXA), developing their own set of voluntary, non-binding debris mitigation guidelines. In 2002, after a multi-year effort, the Inter-Agency Space Debris Coordination Committee (IADC), comprising 11 space agencies, adopted a set of recommendations for debris mitigation. In February 2007, the Scientific and Technical Subcommittee (STSC) of the United Nations' Committee on the Peaceful Uses of Outer Space (COPUOS) developed these recommendations into a set of guidelines which were adopted by the UN in 2008 [16]. Still space debris mitigation guidelines provide just an example of what needs to be done while how to implement them must be specified via international standards that are currently studied by the International Organization for Standardization (ISO).

The mitigation measures of space debris population can be divided in two main categories:

1. protection of a spacecraft by shielding structures (against particles of 0.1-1 cm size) and by collision avoidance (against those larger than 10 cm);

2. prevention of the collisional cascading process, known as Kessler syndrome, by reducing the amount of new debris created and, in the longer term, removing existing in-orbit mass.

The protection of an unmanned spacecraft can be successfully achieved by reallocating the sensitive equipment away from the most probable impact direction, and/or by shielding sensitive parts with protective fabric layers. Such expedient can significantly increase the survivability of a spacecraft against particles up to 0.1 cm in size. However it adds more mass to a spacecraft increasing its launch cost. For larger particles, that can be tracked by the US SSN, collision avoidance maneuver is used since the damage inflicted to a spacecraft would be catastrophic (refer to the Table 1.1). However the simulations has suggested that the close approaches will rise from 13 000 a week in 2009 to 20 000 by 2019 and more than 50 000 by 2059 making the collision avoidance procedure unfeasible in couple of years.

In the long term the only solution to the problem of orbital debris is to stabilize the space debris environment, by reducing the amount of debris created by future missions, and subsequently removing the existing in-orbit material.

The reduction of the future amount of debris have been codified by IDAC as a set of the following guidelines [17, 2]:

- limit debris release during normal operations;

- minimize the potential for break-ups and accidental collisions during operational phases;
- avoid intentional destruction of spacecrafts and other harmful activities (such as ASAT tests);
- minimize the potential for post-mission explosions resulting from stored energy. This implies *passivation* of satellites and rocket bodies at the end of their useful life;
- reduce the presence of spacecrafts and launch vehicle orbital stages in the LEO region after the end of their mission. Objects in LEO should be designed to re-enter the Earth's atmosphere within 25 years of ending their mission;
- reduce the interference of spacecraft and launch vehicle orbital stages with the GEO region after their end of mission. In other words re-orbit the objects into the *graveyard orbits* having the altitude about 300 km above the GEO ring.

The future trend of the debris issue will depend upon whether the creation or removal rate dominates. At present, the only mechanism for reducing the amount of debris is orbital decay through atmospheric drag and thus reentry in to the Earth's atmosphere. This mechanism is only effective in a restricted range of low Earth orbits and its effectiveness changes greatly with periodic variations of air density. At higher orbits, it may take hundreds to thousands of years for objects to reenter, augmenting the number of objects in space. With today's annual launch rates of 60 to 70 launches, the creation rate of debris has outpaced the natural removal rate causing the net growth in the debris population in LEO at an average rate of approximately 5 % per year. This means that in a *business-as-usual* scenario and at mean historic rates of fragmentation of four to five per year, the number of objects in space will increase exponentially [2]. Moreover the first-ever accidental in-orbit collision between Kosmos 2251 and the operational Iridium 33 in 2009, mentioned in Subsection 1.1.1, evidenced the conclusion of several recent modeling studies. Those studies indicate that that even with no future launches the degree of fragmentation in LEO has reached a self-sustaining level, predicted by Kessler and Cour-Palais in 1978 [11, 3, 4]. Even with the almost complete adoption of the aforementioned measures the growth of the debris population in LEO is inevitable. This can be seen in Figure 1.4 that shows the cumulative number of accidental collisions in LEO form the simulations. The top two curves of Figure 1.4 indicate that for the next 40 years the difference between

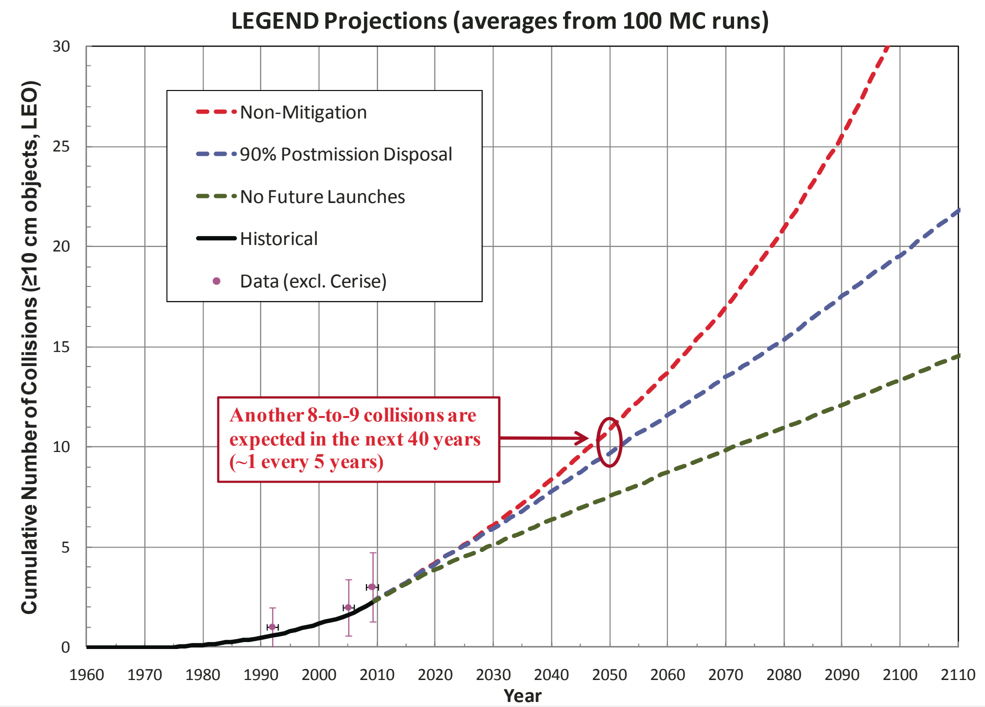

Figure 1.4: Predicted accidental collisions in LEO [14]

the non-mitigation and 90 % post-mission disposal scenarios is small resulting in about 8 or 9 collisions among the cataloged objects (about one every 5 years). Approximately 50 % of the predicted collisions are catastrophic collisions. Current trends lies somewhere between the upper and middle lines.

Therefore, to permanently stabilize the space debris environment in the next 200 years, active debris removal (ADR) of existing objects should be considered despite many challenges of technical and non-technical nature. To accomplish that an effective removal strategy must be developed selecting the potential targets based on their mass and collision probability [5].

The benefits of ADR can be appreciated in Figure 1.5 which is the result of simulations carried out with the NASA long-term debris evolutionary model (LEGEND). The top curve indicates that in a *business-as-usual* scenario with 90 % of post-mission disposal (PMD) measures applied the orbital population of debris will increase up to ~75 % during the next 200 years. Only applying the ADR concept, starting from 2020 for example, the growth of the previously mentioned population will be reduced by half, if two objects per year are removed, or completely stabilized, if five objects per year are removed. However, if the final goal is instead to restore the space environment as it was before the Fengyun-1C break-up in 2007 the removal of more than five objects per year must be considered.

The impact of the three scenarios on to the expected rate of catastrophic

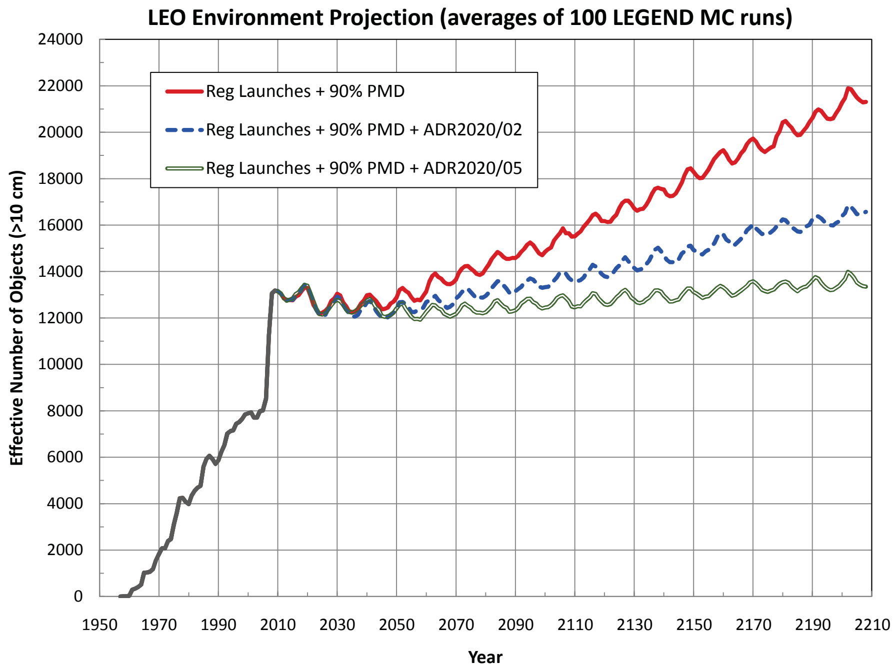

Figure 1.5: Benefits of using ADR to limit the LEO population [18]

Table 1.3: Predicted catastrophic collisions in LEO [18]

Scenarios	i-i collisions	i-f collisions	f-f collisions	Total collisions
90 % PMD	10.2	10.9	3.0	24.1
90 % PMD+ADR2020/2	8.2	7.0	1.9	17.1
90 % PMD+ADR2020/5	6.5	5.5	1.8	13.8

collisions in the next 200 years can be observed in Table 1.3. In it the collisions are separated into three categories: those involving two intact objects (i-i), those involving one intact and one fragment (i-f), and those involving two fragments (f-f). In general, an intact-intact collision is more likely to generate more debris than an intact-fragment collision.

The ADR methods that have been proposed, until now, to the international space community are based on the concept of de-orbiting or re-orbiting a spacecraft by:

- decreasing its orbital velocity by using high-powered ground based laser;
- increasing the drag force exerted on a spacecraft by rolling out an electrodynamic tether;
- using a momentum exchange tether acting as a swing;

- using another spacecraft equipped with robotic grappling device;
- attaching a propulsion device to a target spacecraft.

Only the combination of mitigation measures and, most of all, active removal of space debris, which today lacks, will maintain the space debris population at a safe level for future space operations. However, there are still many challenges ahead and the most difficult one are of political, legal economic and cultural nature [17].

1.2 Orbital Robotics

1.2.1 Background

Robotics can be defined as [19]:

> The study of those machines that can replace human beings in the execution of a task, as regards both physical activity and decision making.

Over the course of centuries, human beings have always dreamed to create intelligent and skilled substitutes that would be able to interact with the surrounding environment in the same way as humans do. In fact the term *robot* derives from the word "robota" which means subordinate labor in Slav languages and was first introduced in 1920 by Czech playwright Karel Čapek in his play "Rossum's Universal Robots (R.U.R)". Despite this man's greatest ambition it wasn't until 1960s that the early robots appeared thanks to the convergence of two technologies: numerical control and teleoperation. Today robots have substantial effect on many aspects of modern life ranging from industrial manufacturing to healthcare, transportation, exploration of the deep space and sea. While tomorrow robotic presence will be as widespread as personal computers are today [20].

An ultimate application of robotics is outer space since it represents for humans the extreme and hazardous environment par excellence with its drastic temperatures, vacuum, radiation, absence of gravity, and great distances. Indeed robotic manipulators, although remotely controlled, have played over the past few decades increasingly important role assisting human activities in space for the construction and maintenance of space modules and structures. Human beings are of course by far more skillful than present-day robots but if the comparison is made between an astronaut during an extra-vehicular activity (EVA) and the best available robot, then the difference is really small [21]. Human intuition

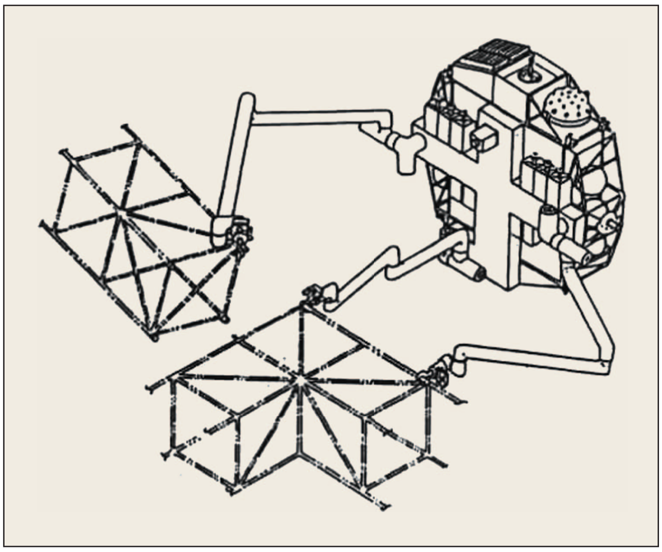

Figure 1.6: Free-flying space robot discussed in the Automation, Robotics, and Machine Intelligence Systems (ARAMIS) report [22]

and intelligence makes astronauts irreplaceable in non-nominal and unpredictable situations. Even so the transport and the infrastructure (e. g. life support) that they require is expensive and sometimes it exposes them to needless risks. Robotic systems on the other hand, while having many limitations, can perform certain tasks with less risk and occasionally with improved performance over humans. Since they have lower cost, require minimal support infrastructure, and have an "indefinite" work life in orbit they can be sent into situations that are to risky for humans or, as it was done until present, as precursors of planetary exploration. The popular NASA Mars rovers Spirit and Opportunity are just the latest examples of robots that allowed scientists to make breakthrough discoveries that otherwise would be impossible.

A robotic spacecraft is considered by the space community any unmanned spacecraft. Nevertheless with the term *space robots* are considered specifically those devices that can assist astronauts or extend human exploration of space [20]. In addition in this section the emphasis will be placed on systems involving robotic arms for manipulation and having the flexibility to perform different tasks.

1.2.2 History of orbital robotics

Concepts of in-orbit assembly or servicing of spacecrafts and space structures by a robotic free-flyer have their origins back in early 1980s when NASA published the Automation, Robotics, and Machine Intelligence Systems (ARAMIS) report. Figure 1.6 is an illustration of the free-flyer described in the aforementioned report.

An appealing scenario was to use tele-operated or autonomous free-flying robots to build in-orbit structures and in particular a space station. In reality, the construction of current International Space Station (ISS) has required many hours of EVAs and the assistance of the remotely controlled Shuttle Remote Manipulator System (SRMS, better know as Canadarm) and Space Station Remote Manipulator System (SSRMS, better know as Canadarm2).

Another important area of application is to use autonomous space robots to perform servicing tasks of failing spacecrafts or even to actively remove those that are irreparable. At present, unmanned servicing missions have not yet become operational even though there were several technology demonstration missions, such as Engineering Test Satellite (ETS)-VII and Orbital Express [22].

Space Shuttle Remote Manipulator System

The *Shuttle Remote Manipulator System* (SRMS), or *Canadarm* was the first robotic manipulator arm used in Earth's orbital environment. It made its space debut on the Space Shuttle Columbia (STS-2) on November 13, 1981 and was successfully used for 30 years retiring along with the Space Shuttle program after the mission STS-135, which marked the robotic arm's 90th flight. It was a mechanical arm 15 m long with 6 degrees of freedom (DOF) and, similarly to a human arm, it had shoulder yaw and pitch joints, an elbow pitch joint and wrist pitch, yaw, and roll joints. Its purpose was mainly to maneuver a payload from the payload bay of the Space Shuttle orbiter to its final position and than release it. It was also used to catch an in-orbit spacecraft and berth it to the payload bay of the orbiter as well as to assist human EVAs by attaching a foothold at the end point of the arm. Servicing and maintenance missions of the Hubble Space Telescope (HST) and the construction of the International Space Station (ISS) are just some of the most remarkable missions that used SRMS as a tool. Figure 1.6 shows the Canadarm and the Canadarm2 (SRMS' sibling on the ISS) work together to unload cargo from the payload bay of Space Shuttle Endeavour on August 15, 2007.

After the accident of the Space Shuttle Columbia (STS-107) on February 1, 2003 SRMS played another important role being used, along with the Orbiter Boom Sensor System (OBSS), to inspect the external thermal shield of the orbiter for eventual damage that might occurred during the launch [23].

Figure 1.7: Team work of the Canadarm and Canadarm2 to unload Space Shuttle Endevour (credit: NASA)

ISS-Mounted Manipulator Systems

As of August 2011, 135 launches have been made to the International Space Station since the launch of the first module, Zarya, on November 20, 1998: 74 Russian vehicles, 37 space shuttles, two European and two Japanese vehicles [24]. It represents the largest human outpost in orbit and as well a flying international laboratory and as such it has been equipped with several robotic systems in order to facilitate various activities on the station while others are planed in near future.

The *Space Station Remote Manipulator System* (SSRMS) or *Canadarm2*, launched in April 2001, is the next generation of the Space Shuttle's original SRMS, used on the ISS. Since its installation, during the STS-100, it has played a major role alongside the SRMS in the construction and maintenance of the ISS both by assisting EVAs of astronauts and taking over the payload from the Shuttle's SRMS (see Figure 1.7). Canadarm2 is 17.6 m long, when fully extended, and has seven joints. Furthermore it is self-relocatable using an inch-worm-like movement or using a mobile base system (MBS) to cover wider ares of the ISS.

The *Special Purpose Dexterous Manipulator* (SPDM), or *Dextre*, is dual-arm manipulator system, much smaller than the previously mentioned SSRMS and capable of performing delicate maintenance work and repairs currently done by astronauts. It was launched in March, 2008 and on February 4, 2011 it completed successfully its first assignment which consisted in unpacking two critical pieces of equipment delivered by Japan's Kounotori2 spacecraft. As it can be seen in

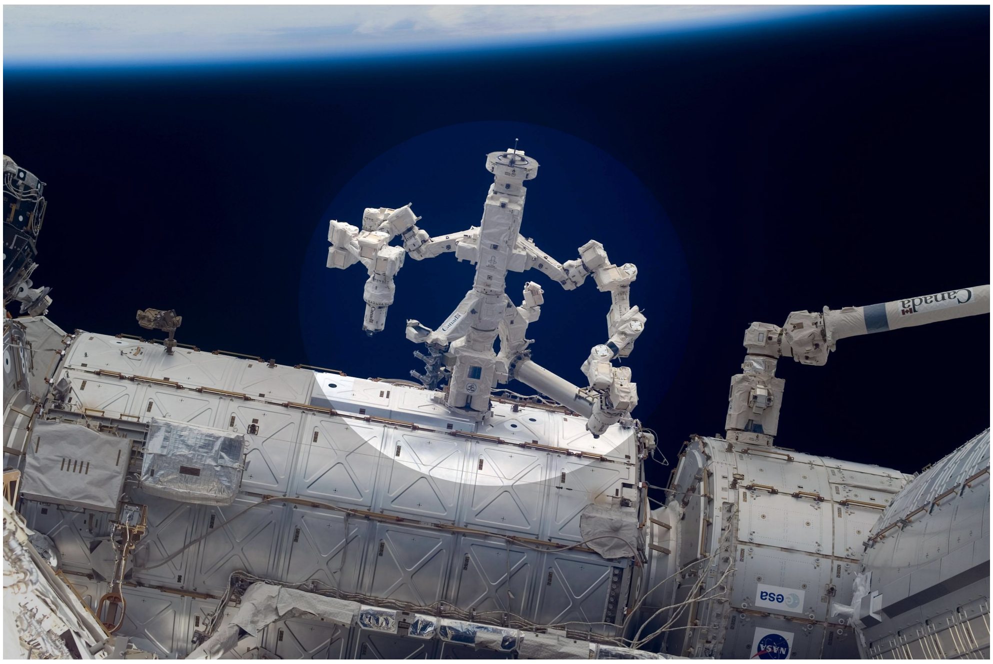

Figure 1.8: Special Purpose Dexterous Manipulator (SPDM) or Dextre (credit: NASA)

Figure 1.8 the SPDM resembles a headless torso equipped with two extremely agile, 3.35 m arms each of which has seven degrees of freedom. The body has just one degree of freedom and can be attached at the end of the SSRM or it can be positioned by the latter at the various orbital replacement unit (ORU) worksites around the space station.

The *Japanese Experiment Module Remote Manipulator System* (JEMRMS) is a robotic manipulator system developed by JAXA. Its is intended for supporting experiments conducted on the exposed facility of the Japanese Experiment Module (JEM) or for supporting its maintenance tasks. The JEMRMS is composed of two arms having both six degrees of freedom: the main, 9.9 m, arm and the small fine, 1.9 m, arm. The main arm was launched on May 2008 alongside the Kibo Pressurized Module while the small fine arm was launched a year after on September 2009 aboard the unmanned H-II Transfer Vehicle (HTV).

The *Robotic Component Verification on the ISS* (ROKVISS) was a six degrees of freedom, 0.5 m long manipulator arm with a dedicated test bench, installed, on January 2005, on the outer wall of the Russian service module of the ISS, Zvezda. It was developed by the German Aerospace Agency (DLR) in cooperation with major German space companies and close collaboration of the Russian Federal Space Agency. ROKVISS was proposed to verify and demonstrate the performance and capabilities of future modular light-weight robots under real space conditions as well to verify the feasibility of direct tele-manipulation through a series of experiments of telepresence. On September 2011, after six years, ROKVISS was brought back to Earth for analysis and after a series of tests it confirmed that the current design of robots developed at DLR Institute of Robotics and Mechatronics is perfectly capable of dealing with the harsh space environment [23].

ROTEX

The *Robot Technology Experiment* (ROTEX), developed by the German Aerospace Agency (DLR), represents one of the important milestones of space robotics. The first remotely controlled multi-sensory robotic arm was flown on the Space Shuttle Columbia (STS-55) in 1993 with the Spacelab-Mission D2. The ROTEX manipulator was a small robot arm with six degrees of freedom and able to reach in all directions and grasp objects within the enclosed work cell. Even so, the experiments proved several key technologies, such as a multi-sensory gripper, teleoperation from the ground and by the astronauts, shared autonomy, and time-delay compensation by the use of a predictive graphic display.

Engineering Test Satellite

Engineering Test Satellite (ETS)-VII, shown in Figure 1.9, is considered to be another milestone in the development of robotic technology in space, particularly in the area of on-orbit servicing. ETS-VII was an unmanned spacecraft equipped with a 2 m long, six degrees of freedom manipulator arm, developed and launched by the National Space Development Agency of Japan (NASDA, currently JAXA) in November 1997. The mission goal of ETS-VII was to test free-flying robotics technology and demonstrate the feasibility of unmanned orbital operations. Autonomous randevous/docking operations and robot experiments were the two subtasks of the principal mission objective.

The ETS-VII consisted of two main parts (Figure 1.9): the main satellite was named Hikoboshi and performed as a chaser while the smaller satellite was named Orihime and acted as a target for randevous/docking experiments. During a two year mission both R-bar and V-bar approaching and docking scenarios were considered and successfully completed using: the global positioning system (GPS), rendezvous laser radar, vision-based proximity sensor, and onboard autonomy [22].

The robot experiments were conducted using the onboard 6 DOF manipulator allowing to obtain important flight data used subsequently to verify the studies regarding the free-flying space robot. These experiments included:

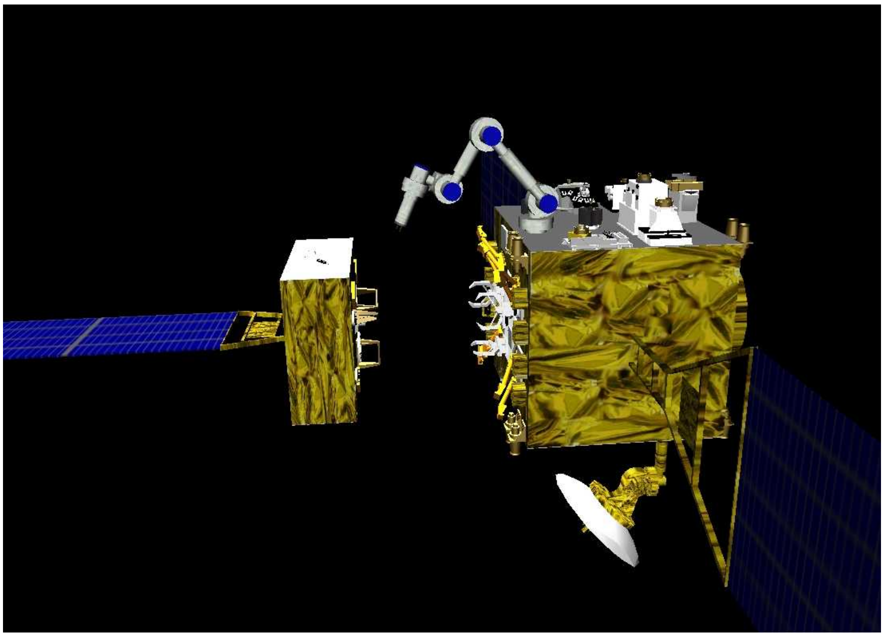

Figure 1.9: Japanese Engineering Test Satellite (ETS-VII) (credit: Space Robotics Laboratory, Tohoku University)

- remote observation of the spacecraft's surface using video cameras attached at the shoulder and hand of the manipulator arm;
- robotic servicing tasks, under teleoperation from the ground, such as the exchange of an ORU, fuel (water) transfer and handling delicate equipment like a flexible wire or a solar cell sheet;
- testing of the dexterity of the manipulator arm using the task board;
- autonomous capture and berthing of a target satellite even though for safety reasons, Orihime was freely floating inside the open space made by partially released docking mechanisms on Hikoboshi;
- dynamically coordinated control between the manipulator reaction and the satellite attitude response.

Ranger

Ranger is a teleoperated dexterous robotic servicing system developed under the founding from NASA at the University of Maryland's Space Systems Laboratory. The design of Ranger is based largely on the requirements for robotic servicing of HST which previously required human EVAs.

Ranger consists of two dexterous manipulators each having ten actuators for eight degrees of freedom, plus two actuation motions for the interchangeable end effectors. Originally designed, in 1993, for a free-flying experiment, the

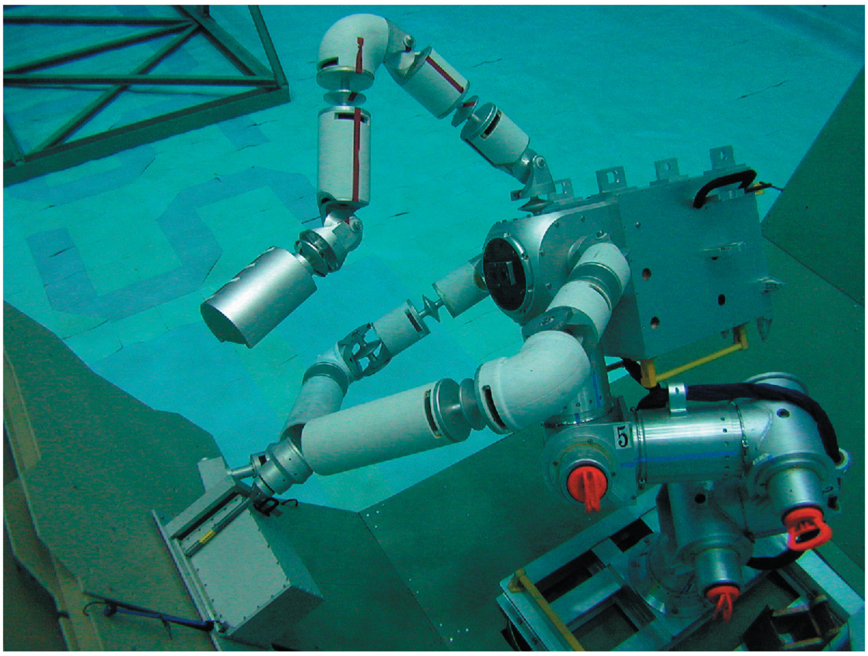

Figure 1.10: Neutral buoyancy test of the Ranger Telerobotic Shuttle Experiment (credit: Space Systems Laboratory, University of Maryland)

Ranger Telerobotic Flight Experiment (RTFX) evolved into the Ranger Telerobotic Shuttle Experiment (RTSX), in 1996, when a potential launch opportunity came up [25]. Despite several tests and demonstrations for servicing missions in neutral buoyancy facility of the University of Maryland (Figure 1.10) the effectiveness of the robot have still to be tested in space.

Orbital Express

Orbital Express was a space mission managed by the United States Defense Advanced Research Projects Agency (DARPA) and a team led by engineers at NASA's Marshall Space Flight Center (MSFC). The Orbital Express program was developed to validate a safe and cost-effective approach to autonomously service satellites in orbit. The system was launched in March 2007 and consisted of two spacecrafts (Figure 1.11): an Autonomous Space Transport Robotic Operations (ASTRO) vehicle, developed by Boeing Integrated Defense Systems, and a prototype of modular Next Generation serviceable Satellite (NEXTSat), developed by Ball Aerospace & Technologies Corp. Furthermore the ASTRO vehicle was equipped with a 3 m long robotic manipulator arm developed by MacDonald, Dettwiler and Associates Ltd. (MDA).

During the three month mission eight scenarios were conducted establishing for the first time in history the autonomous on-orbit servicing of a spacecraft. Although similar technologies and approaches were used 10 years before during

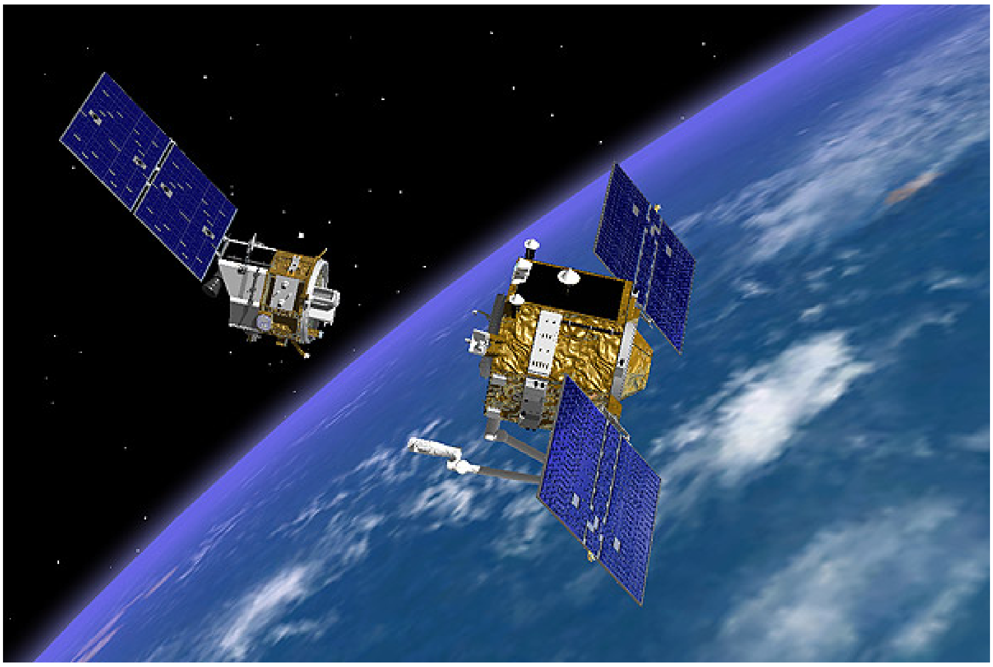

Figure 1.11: Orbital Express mission during unmated operations (credit: Boeing)

the ETS-VII mission, Orbital Express demonstrated higher level of autonomy. The mission proved that the autonomous rendezvous and docking systems could become a viable alternative to human-piloted missions in the next decade.

The last scenario, for example, required ASTRO to separate from NextSat to a distance of 7 km, then return, perform a forced motion fly around inspection, and finally approach and grapple the NextSat with the robotic arm. After that, ASTRO approached within 1 m of NextSat, grappled it with with the robotic arm and then berthed with it. After successful mating, propellant transfer, battery and computer replacement activities followed achieving the first unassisted component exchange in space history. However, it must be highlighted that during both autonomous docking and manipulator capturing/berthing the target satellite was stabilized and cooperative meaning that it was equipped with a dedicated fixture and optical marks to be detected by the chaser vehicle [22]. In reality this won't always be the case since unstabilized or noncooperative targets are quite recurrent, which requires a higher level of technology and further missions.

1.2.3 Active debris removal and on-orbit servicing

On-orbit Servicing

The launch and subsequent deployment of a satellite unfortunately isn't always successful. Traditionally, the most common source of failure, in the past, was a launch failure. However, in recent years on-orbit failures have prevailed for the first time. Orbit insertion failure is now a common failure mode, particularly for GEO satellites. However, even after a successful insertion, spacecrafts may face other types of failure. The simplest (and quite common) on-orbit failure mode is the deficiency of mechanisms to deploy. This kind of malfunction could fairly compromise the whole mission while relatively simple robotic system could disengage and unblock the jammed mechanisms reestablishing the operational condition of a spacecraft [26].

Robotic on-orbit maintenance and servicing represents a long-awaited dream in the space robotics community since the conceptual designs of such a mission in ARAMIS report in early 1980s. Although ROTEX, ETS-VII, Ranger, and ASTRO, mentioned in the previous subsection, are technological demonstrations pointing in that direction, robotic on-orbit servicing (OSS) missions have not become routinely operational yet. Instead, for many years, human EVAs in addition to teleoperated robots such as Canadarm and Canadarm2 have been used to service expensive spacecrafts such as HST or ISS [23].

Nevertheless, in light of currently planned missions, the future will only show major application of space robotics. The autonomous robotic OOS of failed or failing spacecrafts is becoming more and more attractive since it could sensibly extend its lifetime of a spacecraft or perform a its rescue. In addition robotic OOS could perform a re-orbit or a de-orbit of a spacecraft at the end of its life decreasing the amount of space debris. MacDonald, Dettwiler and Associates's Space Infrastructure Servicing (SIS) vehicle and the German Orbital Life Extension Vehicle (OLEV) are just two recent projects of this kind. These projects could extend the operational lifetime of current geosynchronous satellites leading to a more cost-effective and flexible use of them and thus preserve the outer space environment for future generations.

Active Debris Removal

Space debris has become in recent years a growing concern of the space community, as it was evidenced in Subsection 1.1.2. Recent on-orbit collisions as well as few uncontrolled reentries of non functional spacecrafts acted as a remainder of a problem that has yet to be solved. Furthermore, due to a potential onset of the *Kessler syndrome* in the space environment, the future projections of cumulative number of accidental collisions in LEO (Figure 1.4) indicate that the debris population will just grow exponentially even with no future launches. Therefore to stop this kind of instability, that would eventually lead to a belt of debris around the Earth, active debris removal (ADR) should be considered (see Figure 1.5) [2].

This can be most efficiently done by removing objects that have the greatest likelihood of generating big amounts of fragments in the future, i. e old spacecrafts and rocket stages which alone represent most of the on-orbit mass. Taking into account that the major mass repositories are located around 600, 800 and 1 000 km altitudes, out of reach of current human missions, the most promising idea of ADR concept is the one of a robotic spacecraft equipped with a grappling device.

Even though this kind of spacecraft could also be used to rescue a satellite that happens to be in an unexpected orbit, due to an anomaly of a launch vehicle or of an orbital transfer system, ADR systems are very different from OOS systems. Satellite capture and servicing involves grasping a relatively large, well known, cooperative object, without damaging it. The debris removal, on the other hand, involves targets which mass properties and size are largely unknown and the damage, that could occur during the capture, is of less importance [27]. In addition, some spacecrafts may contain leftover propellant and/or have significant tumble rates evidencing the non-trivial problem of capturing those targets. These problems along with the nonholonomic behavior of the free-floating system and, most of all, problems of non-technical nature such as ownership, policy, and liability of abandoned spacecrafts have limited the development of ADR systems.

ETS-VII and Orbital Express mission are two outstanding examples even though their primary goal was to demonstrate the feasibility of the OOS concept and not of the ADR concept. Nevertheless as the international community gradually agrees on the need for ADR, the attention will shift from environment modeling to technology development, engineering, and operations. The future Deutsche Orbitale Servicing Mission (DEOS), promoted by the German Aerospace Center (DLR), is one excellent example since the objectives of the mission are to demonstrate the capture of a tumbling and non-supportive client satellite and a controlled de-orbiting of the mated system within a predefined orbit corridor.

Robotic ADR missions are attractive means for reducing the population of debris because of the dangers associated with this type of mission. However given the unknown shape and properties of the debris prior to rendezvous the problem is more challenging than the capture of a cooperative spacecraft highlighting the proportions of the challenge that ADR involves.

2 DEOS: Space Robotics Mission

The future trend of space activities indicates that space robotic systems will play an increasingly important role in the next decade. Deutsche Orbitale Servicing Mission (DEOS) is a proof of this future tendency. Its primary objectives are the capture of a non-cooperative satellite by means of a manipulator and controlled re-entry of the rigidly coupled configuration within a given re-entry corridor. In order to accomplish successfully those objectives, experimental evaluation of control and planning algorithms is needed as the dynamic interaction between a space robotic manipulator and its base could lead to system performance degradation.

The structure of this chapter consists of two sections and few subsections. Section 2.1 describes the objectives of the DEOS mission and the robotic payload of the servicer spacecraft while Section 2.2 illustrates different simulation methods of the microgravity environment. The examined simulation methods include air beatings, neutral buoyancy, parabolic flights, drop facilities, suspension systems and active robotic gravity compensation systems. Particular attention is given to the preliminary study of the suspended rotating platform, usable to simulate on ground the motion of a tumbling spacecraft, and to the description of the robotic simulation concept developed at the DLR Institute of Robotics and Mechatronics.

2.1 DEOS Mission

2.1.1 Overview

The interest in space robotics for in-orbit servicing, assembly of large structures and debris mitigation has increased substantially over the past few decades (see Section 1.2) making the OOS and the ADR missions an integral part of space programs of the US, Japan, Canada, Germany and many other countries. Within this context the German Aerospace Agency (DLR) is developing the on-orbit servicing technology demonstration mission (see Figure 2.1), DEOS, following

Figure 2.1: DEOS mission concept with the Client (left) and the Servicer (right) (credit: SpaceTech GmbH)

the footsteps of former on-orbit robotic missions such as the Japanese ETS-VII and the American Orbital Express (OE) missions. Currently the project is in the phase-B study indicating that the specification of technical requirements of the system is undergoing the preliminary definition stage and that the selected solution will be later evaluated according to the schedule, the budget, the target cost and the organization requirements [**?**].

The DEOS space segment consists of two spacecrafts, named Client and Servicer (or Target and Chaser), having the specifications, as of January 2011, indicated in Table 2.1. The design of both spacecrafts has been chosen according to different tasks that will be performed during the one year mission. In particular, the client spacecraft is designed to perform different attitude maneuvers in order to simulate a behavior of a non-cooperative client satellite. At the beginning, it will have an Earth-oriented attitude mode, then, increasing gradually the complexity of the experimental program, it will change to a spinning mode and finally it will change to a tumbling attitude behavior. Even though both Client and Servicer are equipped with GPS receivers they will be used just as a reference for subsequent evaluation or in case of a collision avoidance maneuver. Instead the vision based system, using mono and stereo cameras, will be used for the nominal approach navigation [28].

The primary objectives of the DEOS mission are [29]:

Table 2.1: Specifications of the Client and Servicer satellites

Spacecraft	Client	Servicer
Dimensions (H×W×L) [m]	$1.3 \times 1.3 \times 1.9$	$1.74 \times 1.74 \times 2$
Dry mass [kg]	268	610.10
Propellant mass [kg]	14.5 of N_2 126 of N_2H_4	114 of N_2
Total mass [kg]	409	724.10
Power bus type	Unregulated 28 V (26 ~ 33.6 V)	
Avg. satellite power [W]	120 - 240 (sun-to-orbit angle dependent)	280 - 700 (sun-to-orbit angle dependent)
S/A cells	GaAs Triple Junction	
Battery (Li-ion) Capacity [Ah]	2×24	4×24
AOC sensors	Coarse Earth/Sun Sensors, Magnetometer, Gyroscope, GPS Receiver	Coarse Earth/Sun Sensors, Magnetometer, 2 Star Sensors, Gyroscope, GPS Receiver
AOC actuators	Magnetorquer (3-axis), cold gas and hydrazine propulsion	Magnetorquer (3-axis) and cold gas propulsion
RF Comm.	S-Band	S-Band, Ka-Band
Payloads	Holding devices; passive part of the docking and berthing mechanism including LED light pattern	Instrument Control Unit; camera system and LIDAR for relative navigation; manipulator system; active part of the docking and berthing mechanism

- rendezvous with and capture of a tumbling and non-cooperative client satellite by means of a manipulator system, accommodated on a servicing spacecraft;
- execution of a controlled re-entry (de-orbit) of the rigidly coupled configuration within a predefined orbit corridor at the end of the mission.

The expression *"non-cooperative"* means that there is no cooperation with respect to attitude and orbit control system (AOCS) of the client spacecraft, i. e. the client's AOCS will not be operational during its capture and berthing.

For the purpose of the mission, both spacecrafts, Client and Servicer, rigidly connected to each other will be injected together in an initial polar orbit with an altitude of 600 km, an inclination between 85° and 90° and an eccentricity of 0°. The orbit will be than stepwise decreased down to an altitude of 400 km in order to increase the operational complexity caused by reduced contact time with the ground segment. The re-entry (de-orbit) within a predefined re-entry corridor will be initiated from about $\sim$ 400 km. The near polar inclination was chosen because it offers variable illumination conditions during each orbit thus increasing even more the challenge of the mission. Depending on the nodal drift, identical illumination conditions will repeat every 4.3 to 6 months [?].

Similarly to previous missions of this kind (e. g. ETS-VII and OE) the philosophy of DEOS is to subsequently "crawl, walk and run" [28]. This means that the complexity of the experiments will be stepwise increased over the duration of the whole mission. This is especially true for the environmental conditions during which the experiments will be conducted since at the beginning of the operational phase they will be as far as possible favorable. For example tasks that use cameras for navigation or client motion estimation will be first conducted under favorable illumination conditions and than the difficulty of same tasks will be increased worsening the illumination conditions.

In order to reach the aforementioned objectives the set of following tasks must be completed in the order presented hereafter [29].

1. *Far range formation flying.* During this initial mission phase Servicer and Client will fly in formation at constant distance (of at least 2 km) from each other using just GPS sensors or angle measurements provided by different ground stations for navigation. In this configuration the two spacecrafts could stay in orbit for several months without the risk of mutual collision and even without the communication from the ground control. Thus the phase of far range formation flying can be considered sort of safe mode functionality. Furthermore during this period the dynamical behavior of each

spacecraft will be accurately determined evidencing in particular eventual residual spinning and tumbling rates of Client. The end of this phase represents simultaneously the beginning the rendezvous maneuvers.

2. *The rendezvou*s. Starting from the formation flying the main goal of the rendezvous phase is to reduce the initial distance between the client and servicer spacecrafts and enable the latter to capture and berth the former. The entire phase is divided in few sub-phases that include also the hold points which are mandatory when the navigation approach to an unknown target spacecraft is done by camera based navigation. At first, Servicer will reduce the distance to the client spacecraft executing several Hohmann-like orbit maneuvers while the final approach to the mating position will be performed via a v-bar maneuver. At this point the distance between the two spacecrafts will have to be maintained automatically by the Servicer's AOC system which will also have the duty to start automatically the collision avoidance maneuver if the predefined distance isn't respected. Finally, before the capture and berthing of Target, Servicer will again take its distance from it and perform a forced fly-around maneuver for inspection of the latter.

3. *The capture and berthing of a non-cooperative target.* The beginning of the capture phase will be marked by the closer approach of the servicer spacecraft to Client and acquisition of several images of the latter for the estimation of its exact position and relative motion. To achieve this, based on the same principle used for the ROTEX mission described in Section 1.2.2 on page 22, the images will be downloaded to the ground station and used either by the ground operator or by the Servicer's ground control software. Next, Servicer will approach even more the target spacecraft until its grappling fixture is inside the workspace of the manipulator of the former spacecraft. At this point the structural element will be approached and tracked with the manipulator either by an operator in telepresence mode or in automatic mode using the motion planning algorithm (more about these two approaches can be found in Subsection 2.1.2). Finally, the grappling tasks will be tackled grasping the dedicated fixture with the end-effector of the manipulator. During this phase two major control strategies of Servicer will be investigated: *free-flying* and *free-floating*. In the first case, during the motion of the manipulator, the spacecraft will be kept still in the operational space by the Servicer's AOCS. In the second case, on the other hand, the motion of the spacecraft in reaction to the movement of the ma-

nipulator will be allowed. Note however that the experience made during the Dynamic Motion Experiments of the German Technology Experiment on ETS-VII (GETEX), in 1999, highlighted that the complete shutdown of the AOCS during the free-floating mode is completely unrealistic, since the external forces acting in LEO on the spacecraft can not be neglected. Thus, even during the free-floating mode the spacecraft's AOCS must be active to counteract the effects of environmental disturbances while permitting the motions of spacecraft due to that of the manipulator [30, 31].
After closing the gripper, the stabilization of the captured Target will occur to eliminate the residual relative velocity between the two satellites (see Subsection 2.1.2 for more details about the stabilization methods) [30].
The steering and subsequent latching of the Client, in order to obtain a rigidly coupled configuration, are additional mission goals that will be performed once that the primary objective has been reached. During the latching phase, the servicing spacecraft will approach the Client and by inserting the docking interface of the latter into the formers' docking port it will latch it.

4. *The docking with a cooperative target.* This task differs from the previous one since the Client will be actively controlled in order to be approached slowly by the Servicer and perform the autonomous or tele-presence docking without the use of the manipulator. The individual steps of the docking procedure are: acquisition of docking axis, reception, capture and finally latching.

5. *Flight in coupled configuration and re-entry.* The beginning of this phase is tightly bound with the successful completion of the previous ones since its precondition is that the two spacecrafts are in a coupled configuration. There are two types of coupled configurations between client and servicer spacecraft. A rigid coupled configuration can be obtained either using the docking port or the manipulator mechanism, as a mechanical fixture (see Figure 2.2), while a dynamically coupled configuration can be possible only with the manipulator arm (see Figure 2.1). Once that the mentioned precondition is met different flight maneuvers are scheduled in order to perform attitude and orbit maneuvers, the identification of dynamical parameters of the coupled configuration and finally an on-orbit servicing tasks. At last, starting from an altitude of 400 km, a controlled de-orbiting of the rigidly coupled configuration (see Figure 2.2) is expected, as a result of a sequence of maneuvers designed to gradually lower the perigee of the initial orbit.

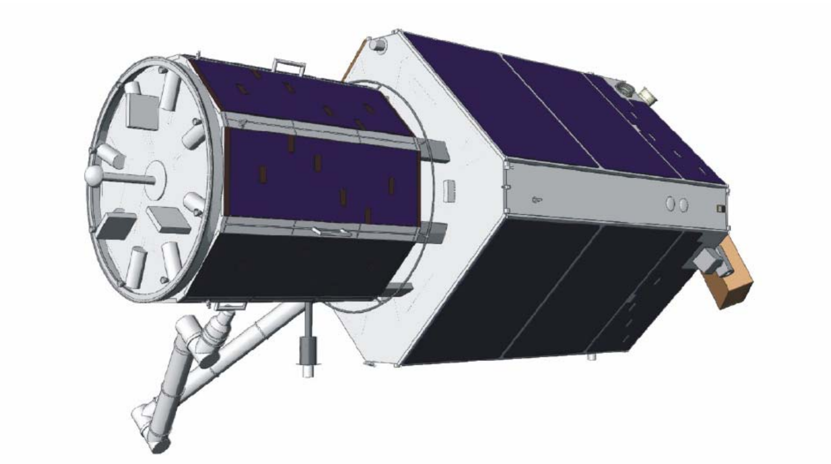

Figure 2.2: DEOS re-entry configuration (credit: SpaceTech GmbH)

2.1.2 Robotic arm

Automation and Robotics (A&R) payload will play an important part during the DEOS mission being highly involved in the capture, stabilization, orbit maneuvers and de-orbiting. The A&R payload consists of the manipulator system, the berthing and docking mechanism and the instrument control unit which will control the A&R payload space segment and the communications with the on-board computer of the Servicer. Furthermore the manipulator system is composed of the manipulator arm, cold redundant stereo cameras and a target illumination system. Among all the A&R systems planned on the Servicer the robotic arm will certainly play the main role given that it will be directly involved in most of the aforementioned tasks. In particular it will have to track the predefined structure part of the Client, grasp it and finally eliminate the relative motion between both satellite bodies.
To achieve this the manipulator of the DEOS has to fulfill certain requirements:

- the kinematics of the robotic arm has to provide wide working space and dexterity in order to perform the capture of the Client independently of its main spinning axis;
- the robotic arm has also to present kinematical redundancy in order to avoid joint-singularities during the mission;
- the robotic arm has to be stowable during the launch phase within the given space on the Servicer.

These top level requirements led to a manipulator having the design shown in Figure 2.3. It has the overall length of 3.227 m (measured from base to the end-

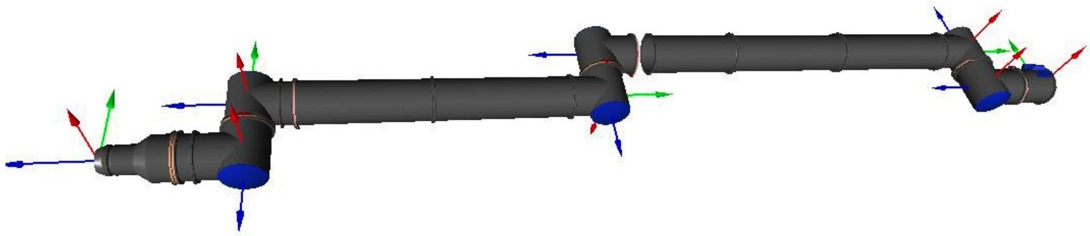

Figure 2.3: DEOS robotic arm (credit: DLR)

effector) and 7 DOF. Additionally it has the mass of 27.1 kg (without the gripper) and a max power consumption of $\sim$ 100 W, during operation, while it consumes only 50 W during a stand-by phase.

The joint elements for the DEOS manipulator are based on the joints developed for the ROKVISS mission, mentioned in Section 1.2. Although the reliability of the ROKVISS joint elements was successfully proven in space the requirements of the DEOS mission, as well as the experience gained during ROKVISS, imposed some modifications such as: electronics redundancy, new gear output position sensor and interconnecting joints bus interface and introduction of a new parking brake [32].

The operational modes of the manipulator that will be used during the mission can be divided into:

- telepresence or active ground control mode during which a ground operator will command directly the manipulator using video informations provided by stereo cameras;
- automatic or passive ground control mode where the role of a ground operator will be confined to initiate the planned operation, monitor it and intervene only in case of anomalies or unexpected behaviors.

In telepresence mode, a human operator will completely immerse himself into the remote environment, using audio, video and haptic feedback by means of the multimodal human machine interface (HMI), visible in Figure 2.4. With it, a human operator will be able to control a teleoperated device on a motion/force level while perceiving and acting as in the real world [33].

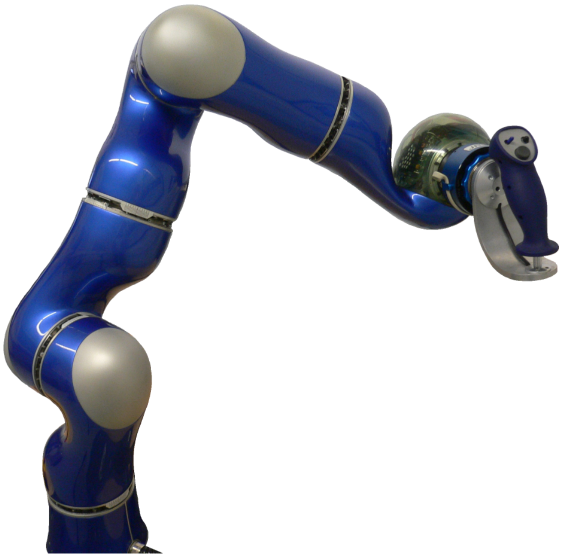

Figure 2.4: Human Machine Interface of the tele-presence control mode (credit: DLR)

Dynamic singularities in telepresence mode can be tackled by informing properly the operator of their existence within the workspace with an additional algorithm. For example, using a graphical representation of the manipulator's singularities in the 3D Cartesian space. This way the operator could decide himself how to proceed in order to avoid the singularities and accomplish the grasping task. However, this is not an elementary task since the singular configurations of a manipulator are defined in joint space $\mathbb{R}^n$ and generally their three dimensional Cartesian representation isn't possible. Nevertheless, even if it were possible, given the very limited joint rates of free-floating systems (e. g. $5\,^{\circ}/_{s}$), such representation would be worthless if those limits were exceeded for a generic end-effector velocity of the manipulator. Thus, an optimization algorithm must be used to optimize the initial configuration of the manipulator/chaser satellite, with respect to the target satellite, in order to avoid the singularities for a longer path while remaining within the joint rate limits.

Therefore, a workspace analysis prior to the telepresence manipulation tasks appears to be necessary to determine the singularity-free workspace, in which the operator can move safely.

The stabilization of the compound system in telepresence mode will be performed directly by an operator by means of tactile and visual feedback [30, 34].

In autonomous mode the singularities will be automatically avoided by the motion planning algorithm since it works in joint space where the singularities of the robot are fixed. But first, it will be necessary to perform the motion estimation and the dynamic model identification of the free-floating target spacecraft by means of range data collected by stereo vision or a laser range sensor [35]. Moreover, the fuel consumption of the free-floating chaser spacecraft could lead to a variation of its initial inertial parameters (measured on-ground), namely the mass, centre of mass position and inertia. Thus, their in orbit identification using accelerometers could be required to improve the path planning and tracking capabilities of the space robot, as well as its efficiency in energy consumption [36, 31].

The stabilization of the compound system in automatic mode, to date, is still object of study. Thus, the precise method of achieving this is unavailable at the moment. However, a good way of addressing this problem could be that to make the robot compliant for the capture phase and once that Target has been captured follow a given trajectory to eliminate any residual motion of the target spacecraft with respect to the chaser spacecraft. In the end, the stiffness of the robot could be slowly increased until the stable condition of the system is reached [30, 37].
The advantage of such impedance control mode is twofold [37]:

- the uncertainty in the inertial properties of the target spacecraft can be neglected;
- the inertia characteristics of the end-effector can be made similar to those of the target thus reaching the so-called mechanical impedance matching that allows us to treat impacts with uncertainty;

2.2 Microgravity Simulation Methods

The capture and berthing phase of the DEOS mission or in general of any other ADR/OOS mission represents one the most critical and complex tasks since the dynamics modeling and motion planning of a space robot are much more complicated than those of a fixed-base manipulator. Moreover, a free-floating system, which will be considered from now on the only control strategy of a space robot, presents nonholonomic behaviors as a result of the non-integrability of the angular momentum equations [38]. In such system, the motion of the spacecraft is exclusively due to the dynamic coupling between the manipulator and its spacecraft. As ti was pointed out in Subsection 2.1.1, the Servicer's AOCS can be used to compensate for these disturbances, but its extensive usage could severely limit the useful lifetime of the spacecraft. Therefore, in a free-floating mode the AOCS will be used only to compensate the external torques acting in LEO while the spacecraft will be permitted to translate and rotate in response to its manipulator motions [30, 31]. Adding to this circumstances the difficulties in communications that will arise, given the Low Earth Orbit of the DEOS mission, it becomes clear that the capture and berthing phase shouldn't be performed in space for the first time. All maneuvers have to be thoroughly analyzed, simulated and verified on the ground under utmost realistic conditions of the space environment in order to explore the capabilities and limitations of the planning and control algorithms. However, experimental evaluation of these algorithms isn't straightforward. The whole system, including its base, must be permitted to have six degrees of freedom and the microgravity environment can be reproduced with limitations.

2.2.1 Standard simulation methods

To this day, standard methods to create microgravity conditions on the ground are the following:

1. *Air-bearings*. Air bearings have played a vital role in the development of unmanned spacecrafts for more than 50 years. Depending on the type of air bearing (i. e. flat or spherical), an almost force-free translational motion or a nearly torque-free rotational motion can be achieved. This is accomplished by creating a thin film of air between the moving and the fixed element of the bearing by means of pressurized air that passes through small holes. In this way the friction between the two segments is virtually inexistent crating the condition of weightlessness and providing one rotational and two translational degrees of freedom. Spherical air bearings, on the other hand, are made of two concentric spheres machined and lapped to small tolerances. One spherical section rotates on an air film bounded by the other section in three degrees of freedom. In this way it is possible to obtain nearly three rotational degrees of freedom. To achieve instead almost all 6 DOF the combination of several types of bearings must be considered complicating considerably the design of the simulator and raising the cost of the system [39]. Nevertheless the flat bearing, despite its inherent characteristic of being a planar testbed, is one of the most useful methods for testing space robots. In the past air-bearing tables have been extensively used especially for studying flexible manipulators and multi-arm space robots, such as the SRMS, SSRMS, JEMRMS and Standford's dual-arm free-flying robotic system [9].

2. *Neutral buoyancy*. Using specially designed underwater versions of spacecraft, robots, and spacesuits the force of buoyancy acting on the hardware can be exactly equal to the force of gravity. In this way the microgravity environment of space can be achieved for an almost unlimited amount of

time. However, generally space designed robots cannot be directly used under water. Instead custom-built neutral buoyancy vehicles, hybrids of space and submersible robots, must be used to simulate the characteristics of on-orbit robotics [40]. Ranger Neutral Buoyancy Vehicle II, illustrated in Figure 1.10, is an example of such kind of prototype since it was designed to be essentially identical to the Ranger TSX flight unit and to be used in the underwater environment. Furthermore, the reaction forces of the surrounding fluid, such as fluid damping and inertia, should be taken into account during experiments since they could alter the dynamics characteristics of the tested system leading to wrong conclusions [9].

3. *Parabolic flights and drop facilities.* Microgravity, which is the condition of relative near weightlessness, can also be achieved on Earth by putting an object in a state of free fall using drop towers or parabolic flights. The latter are conducted on specially-configured aircrafts, which fly in parabolic arcs to create microgravity environment that lasts approximately 20 s. During a flight campaign, which normally consists of three individual flights, around 30 parabolas are flown on each flight, i. e. around 90 parabolas in total. On each parabola, there are two periods of increased gravity (1.8 to 2 g), the pull-up and pull-out phases, which last for about 20 s, immediately prior to and following the 20 s period of reduced gravity ($\sim$ 0.02 g) [41]. Another possible way to create weightlessness is through a free-fall of a drop capsule with the experimental setups on board. The NASA's Zero Gravity Research Facility (see Figure 2.5), located at the Glenn Research Center in Cleveland, Ohio is a 143 m vertical steel vacuum chamber, largely below the ground, in which experiments can experience weightlessness for a 5.18 s, during the 132 free-fall inside the drop vehicle. The experiment vehicle is than stopped in approximately 4.6 m of pellets of expanded polystyrene and experiences a peak deceleration rate of 65 g. The typical drop vehicle is generally cylindrical having the diameter of 1 m and the overall length of 4 m (see Figure 2.5) [42].
   Even though these two methods can provide microgravity test environment for a fraction of the cost of conducting an experiment in space they present two major drawbacks for testing space robots: 1) the dimension and weight of the space robot must be compatible with those of the aircraft cabin or of the drop vehicle; 2) the duration of the microgravity environment and thus of the experiment is very limited, generally of few seconds which most of the time is inappropriate.

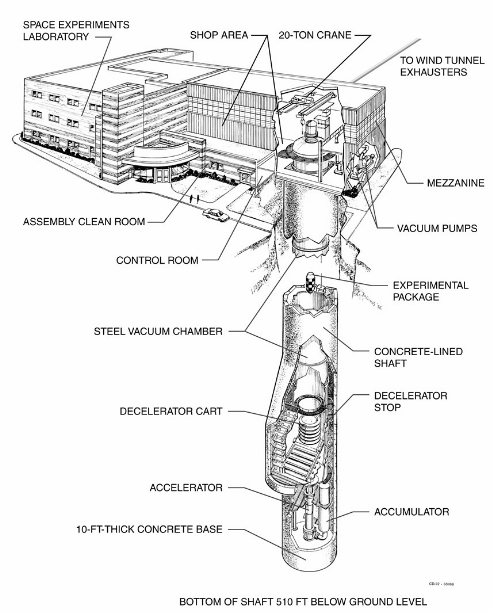

(a) Diagram of the Zero Gravity Research Facility

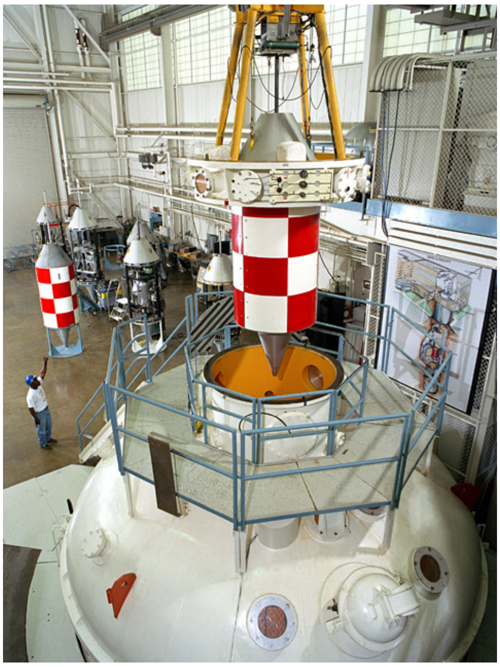

(b) Positioning a drop vehicle on top of the vacuum chamber

Figure 2.5: Zero Gravity Research Facility at NASA Glenn Research Center (credit: NASA)

4. *Suspension systems.* An on-ground suspension system is another possibility for testing a free-flying robots before their use in space missions. In order to generate a weightless conditions a testbed must be able to generate forces of the same amplitude and in the opposite direction of the gravity force acting on each component of a robotic system. This compensating force should be applied in the center of mass of each subsystem and remain constant in amplitude during the three-dimensional motion of a manipulator. Additionally, suspension systems should not apply other forces on the free-flying platform since both joint actuators and control algorithm of the robot are designed for microgravity environment [43]. An example of such testbed was developed, in 1994, by Xu et al. in order to counteract gravitational effects during the laboratory experiments of the Self-Mobile Space Manipulator (SM^2). This gravity compensation system, illustrated in Figure 2.6, consisted of a passive, vertical counterweight system, and an actively controlled, horizontal system. The passive system of counterweights, cables and pulleys provided a constant, vertical balance force to the end of the support cable while the powered overhead carriage was controlled to keep the support point directly above the robot. With this kind of system a weightless environment of 0.01 g can be achieved by accurately tuning

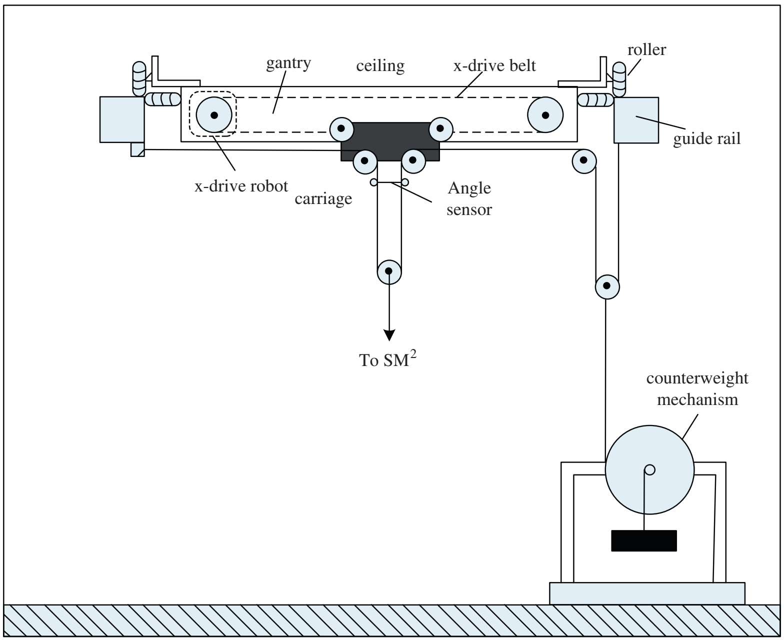

Figure 2.6: Gravity compensation system of the SM^2 [45]

the control parameters [44]. Nevertheless, this kind of system architecture presents two major drawbacks which limit its applications: 1) the identification of kinetic friction and its compensation is very difficult making the system prone to instabilities and worsening the dynamical response of the system; 2) the system may become unstable due to the coupled vibration of the space manipulator and suspension system [45].

Each method illustrated previously has its own advantages and disadvantages. Air-bearing and neutral buoyancy test-beds, although widely used for testing new concepts and control algorithms, require custom-built prototypes of space robots. Suspension systems, on the other hand, can be used for flight hardware but they are more prone to induce disturbances on the attitude of free-floating robots or to cause instabilities. Parabolic flights and drop facilities are particularly attractive for being able to recreate microgravity environment although the size of robotic systems and the time available to perform an experiment are extremely limited [43]. In addition all these conventional microgravity simulation methods have difficulties in testing full 6 DOF contact dynamics of large and complex space systems such as DEOS. Thus a robotics-based active gravity compensation system is considered the most suitable candidate for simulating the capture and berthing phase of the DEOS mission and it will be introduced in Subsection 2.2.3.

2.2.2 Suspended rotating platform

Standard microgravity simulation technologies, illustrated in Subsection 2.2.1, are generally limited regarding the simulation of full 6 DOF contact dynamics between large and complex space systems. Nevertheless they are irreplaceable if we are just interested in spacecraft's attitude variation due to a physical contact.

An active robotic gravity compensation system is a valid alternative to the aforementioned ground-based simulation methods since it does not present limits on the complexity of the space system to be simulated or tested while still affording a full 6 DOF motion condition. Moreover, since it consists of real hardware the modeling of the physical contact is unnecessary and thus it is more accurate than any mathematical contact dynamics model used in computer-based simulations. The concept of such testbed consists generally of two or more robots (see Figure 2.7) controlled to simulate the motion of both client and chaser satellites based on a real-time satellite simulator. When a physical contact occurs, the contact force and moment generated by the docking hardware or by the manipulator arm is fed back to the satellite simulator which than predicts the dynamic responses of the two spacecrafts. Nevertheless, given that robots are used to simulate the dynamics of spacecrafts, the mentioned change will occur with a time delay which will vary from robot to robot. For example the known responding time of the robots of the European Proximity Operations Simulator (EPOS) facility, developed at DLR, is around 4-8 command cycles and each command cycle takes about 4 ms. In other words, the time gap between control command and the physical reactions of the robots can be up to 8 command cycles or 32 ms which is a large time delay for controlling a robot to perform contact motion. Thus a special process control must be developed to handle the time delay problem [46]. Otherwise a passive simulation system, such as an air-bearing testbed or a suspended system, must be used. In this case the dynamic response of the system to a physical contact is instantaneous given that the dynamics of a spacecraft isn't predicted by a mathematical model or simulator. Nevertheless in this case a full 6 DOF on-orbit dynamic motion is difficult to achieve and thus we must be aware of this limitation.

This subsection describes the preliminary study of the ground-based suspended rotating platform for emulating free motion dynamics of a tumbling spacecraft and its subsequent dynamic response during a generic capture phase. In particular, it tackles the motion analysis of the suspended system and the conditions necessary to obtain a regular or uniform precession of the system. Figure 2.8 illustrates the concept of the emulation system consisting of:

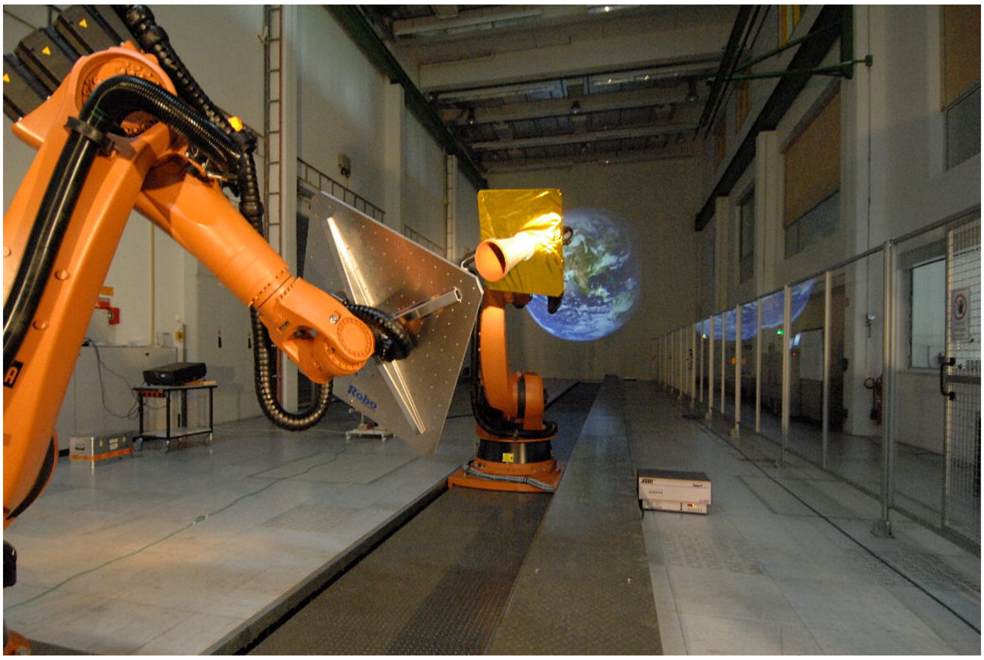

Figure 2.7: European Proximity Operations Simulator (credit: DLR)

- a long rigid cable attached to the ceiling with a spherical joint;
- a short shaft attached to the cable by means of a spherical joint;
- a rotating platform fixed to the shaft and inclined to the vertical by a small angle.

The system presents specific features, that will be emphasized later on, in order to achieve a forced, regular, torque-induced precession of the platform and thus simulate the general motion of a non-cooperative rigid spacecraft in absence of external forces. The dynamics of the system is determined considering it identical to a gyroscopic pendulum rotating about a fixed point, in inertial space, in the presence of gravity. This is justified by the fact that the end-point of the cable, to which the platform is attached, presents small planar oscillations around the initial point during the motion of the platform.

In order to fully comprehend the behavior and the dynamics of a gyroscopic pendulum in the gravitational field let us first determine the equations of motion and the conditions necessary to obtain the regular precession of a similar, yet more familiar case: a symmetric spinning top.

The geometry of a symmetric spinning top in a gravitational field, as illustrated in Figure 2.9, consists of a "heavy" wheel, on a narrow stem whose bottom point is fixed to the origin, but is free to rotate. Since we consider a symmetric body the principal moments of inertia about two axis are equal $I_{xx} = I_{yy} = I_0$ and the moment of inertia about z axis is $I_{zz} = I$. The length of the stem is l

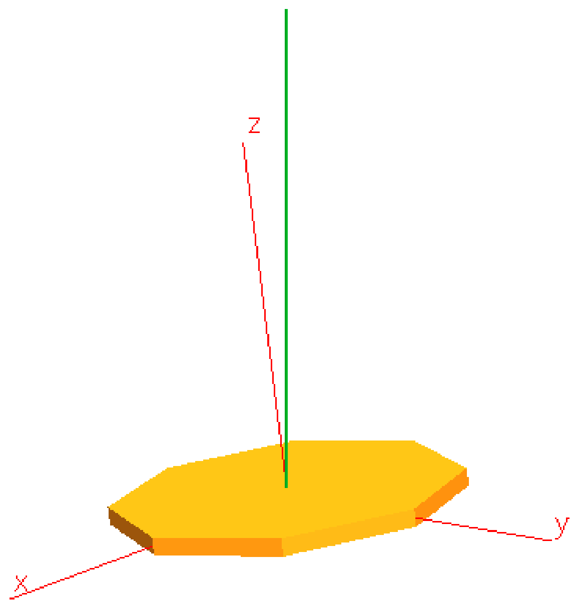

Figure 2.8: Suspended rotating platform

and we assume that its mass is negligible with respect to that of the wheel. The acceleration due to gravity is $\boldsymbol{g}$ and is assumed to point "downwards" along the Z axis. The angular momentum vector is not aligned with the Z axis, but precesses about the Z axis due to the applied moment generated by the force of gravity.

The z axis of the body-fixed reference frame passes through the center of rotation of the top and the motion of the top can be expressed in body-fixed axis by means of Eulerian angles 313 (ϕ, θ, ψ). Referring to the Figure 2.9, the variable ϕ, is the angle of precession, the variable θ is the angle of nutation while the variable ψ is the angle of rotation. Since our top is circularly symmetric, the choice of origin for ψ is arbitrary.

Dynamic equations of spinning top

The general motion of a symmetric top about about a fixed point O can be described by the Euler equations in body-fixed axes, indicated in Figure 2.9 with x, y, z coordinate system, rotating with the body so that its moment of inertia tensor is constant in time. Furthermore, in this reference frame the angular momentum vector of the system is not aligned with the Z axis of the inertial reference frame, unlike in the case of free-body motion Instead it precesses about the Z axis due to the applied external moment. In this body-fixed coordinate system, the main law of attitude dynamics, about a fixed point O, is

$$\dot{\boldsymbol{L}} = \frac{d}{dt}(\boldsymbol{I}\boldsymbol{\omega}) = \boldsymbol{M} \tag{2.1}$$

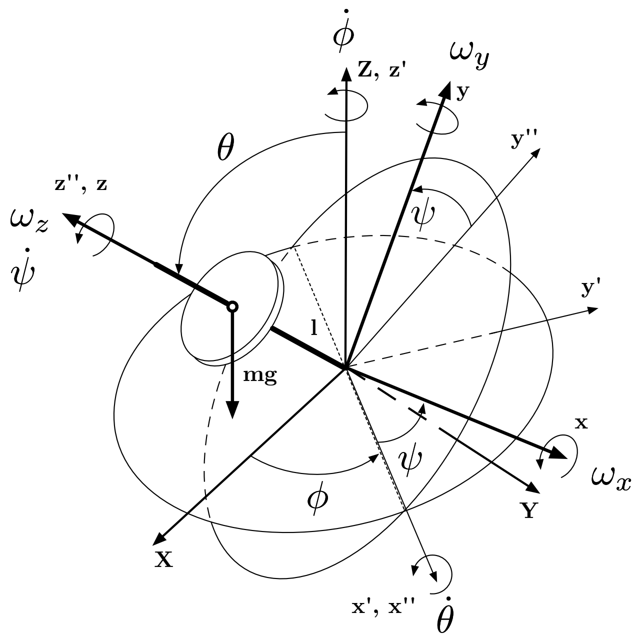

Figure 2.9: Illustration of a symmetric spinning top and its standard body-fixed axis

where $\dot{\boldsymbol{L}}$ is the time derivative of the angular momentum vector, $\boldsymbol{I}$ is the moment of inertia tensor, $\boldsymbol{\omega}$ is the angular velocity vector and $\boldsymbol{M}$ is the vector of external moments applied about a fixed point O. For body-fixed principle axis x, y, z, the components of the angular momentum vector $\boldsymbol{L}$ are

$$\begin{aligned} L_x &= I_0\omega_x \\ L_y &= I_0\omega_y \\ L_z &= I\omega_z \end{aligned} \tag{2.2}$$

while the relationships between the angular velocities along the x, y, z axes and the time rate of the Euler angles 313, ϕ, θ, ψ, shown in Figure 2.9, is

$$\begin{aligned} \omega_x &= \dot{\phi}\sin\theta\sin\psi + \dot{\theta}\cos\psi \\ \omega_y &= \dot{\phi}\sin\theta\cos\psi - \dot{\theta}\sin\psi \\ \omega_z &= \dot{\phi}\cos\theta + \dot{\psi} \end{aligned} \tag{2.3}$$

Given that we have chosen to formulate the equations of motion in an axis system fixed to the body, in order to have the inertia tensor independent of time in our reference frame, we must apply the Coriolis Theorem to (2.1). Thus the change in $\boldsymbol{L}$ due to the instantaneous rotation of the coordinate system will be equal to the actual time rate of change $\dot{\boldsymbol{L}}$ plus the effect of the instantaneous rotation of the body axis with the angular velocity $\boldsymbol{\omega}$

$$\dot{\boldsymbol{L}} = \boldsymbol{I}\dot{\boldsymbol{\omega}} + \boldsymbol{\omega} \times \boldsymbol{L} = \boldsymbol{M} \tag{2.4}$$

or in components

$$\begin{aligned} M_x &= \dot{L}_x - L_y\omega_z + L_z\omega_y \\ M_y &= \dot{L}_y - L_z\omega_x + L_x\omega_z \\ M_z &= \dot{L}_z - L_x\omega_y + L_y\omega_x \end{aligned} \tag{2.5}$$

This particular form of the equations of motion is valid for any set of body-fixed axes. If the axes chosen are principal axes, then we may express the conservation of angular momentum in terms of moments of inertia about the principle axes, obtaining the Euler equations [47]

$$\begin{aligned} M_x &= I_0\dot{\omega}_x - (I_0 - I)\,\omega_y\omega_z \\ M_y &= I_0\dot{\omega}_y - (I - I_0)\,\omega_z\omega_x \\ M_z &= I\dot{\omega}_z \end{aligned} \tag{2.6}$$

which solution provides several serious challenges. In order to obtain the equations of motion that we could use more easily, instead of considering the body-fixed axis indicated in Figure 2.9, we shall consider another coordinate system illustrated in Figure 2.10 that doesn't rotate with the body around its z axis. We are allowed to to that because of the symmetry of the body. Essentially to obtain this coordinate system from the inertial one only the rotation in ϕ and θ are preformed, leading to the geometry shown in Figure 2.10. In this coordinate system, since the ψ rotation did not occur, the angular velocity of the body is

$$\begin{aligned} \omega_x &= \dot{\theta} \\ \omega_y &= \dot{\phi}\sin\theta \\ \omega_z &= \dot{\phi}\cos\theta + \dot{\psi} \end{aligned} \tag{2.7}$$

Thus for this choice of coordinate system, the final form of Euler's equations, expressed in (2.6), becomes [47]

$$\begin{aligned} M_x &= I_0\left(\ddot{\theta} - \dot{\phi}^2\sin\theta\cos\theta\right) + I\dot{\phi}\sin\theta\left(\dot{\phi}\cos\theta + \dot{\psi}\right) \\ M_y &= I_0\left(\ddot{\phi}\sin\theta + 2\dot{\phi}\dot{\theta}\cos\theta\right) - I\dot{\theta}\left(\dot{\phi}\cos\theta + \dot{\psi}\right) \\ M_z &= I\left(\ddot{\psi} + \ddot{\phi}\cos\theta - \dot{\phi}\dot{\theta}\sin\theta\right) \end{aligned} \tag{2.8}$$

Furthermore, for this choice of axis the components of the vector of external moments applied in a fixed point O, $\boldsymbol{M}$, are $M_x = mgl\sin\theta$, $M_y = M_z = 0$ where

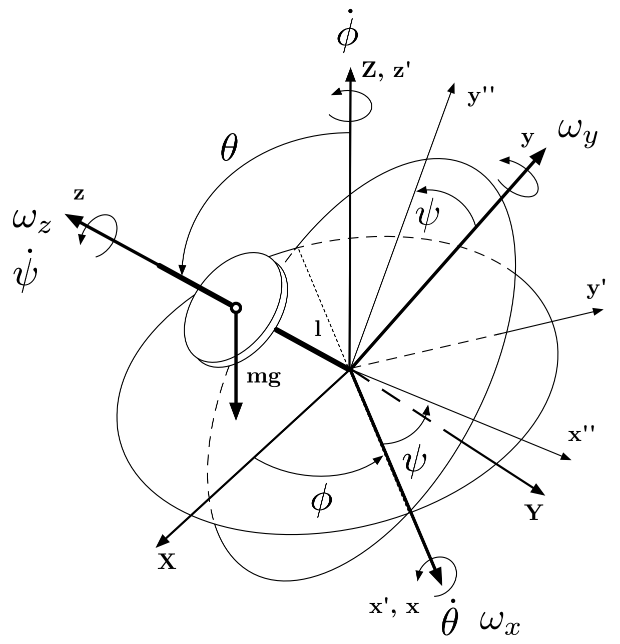

Figure 2.10: Illustration of a symmetric spinning top and of the new reference frame

m is the mass of a top, g is the magnitude of the acceleration due to gravity, while l is the distance from the fixed point O to the center of the mass of a spinning wheel.

Steady precession of a spinning top

The strange at first sight behavior of a spinning top during a regular torque-induced precession has always aroused the curiosity of all who observe it. Referring to Figure 2.11 during this kind of motion the axis of the rotating body generates in space a vertical cone whose aperture is constant with time. This behavior is called a *steady* or *uniform torque-induced precession* (see Figure 2.11) since the top undergoes it under the force of gravity. All points of the gyroscope that lie on its axis of symmetry move uniformly describing circular paths whose centers are located on the vertical line passing through the supporting pivot [48]. Figure 2.11 shows furthermore the circular trajectory of the axis of a top and the loopy trajectory of the end point of an arrow attached firmly to some fixed point displaced from the axis of rotation z.

The most remarkable feature of regular precession is that this kind of motion is actually one of the possible solutions to the dynamical equation of motion expressed in (2.6) or in (2.8) [48]. The criterion for steady precession is most easily obtained directly from (2.8) by imposing that the top rotates at constant speed $\dot{\psi} = \dot{\psi}_0$ about its principal axis, and precesses with constant angular velocity

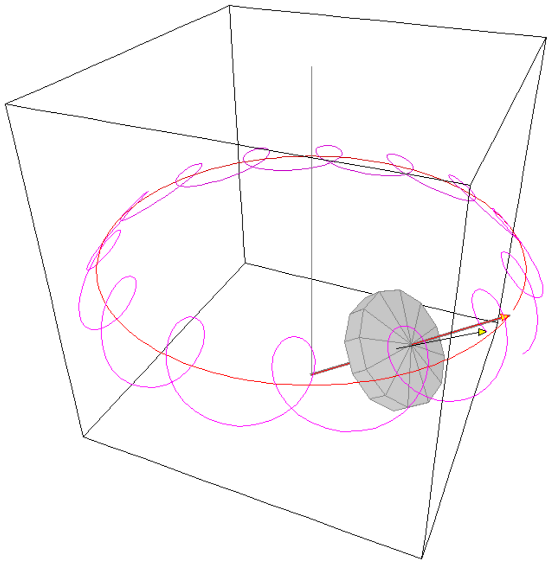

Figure 2.11: Regular precession of a gyroscope

$\dot{\phi} = \dot{\phi}_0$ while maintaining a constant angle of nutation $\theta = \theta_0$ and thus $\dot{\theta} = \ddot{\theta} = 0$. Hence Euler equations for a steady precession of a top reduce to [47]

$$\dot{\phi} \sin\theta \left(I \left(\dot{\phi} \cos\theta + \dot{\psi} \right) - I_0 \dot{\phi} \cos\theta \right) = M_x = mgl \sin\theta \tag{2.9}$$

or

$$I \dot{\phi} \dot{\psi} - (I_0 - I)\, \dot{\phi}^2 \cos\theta = mgl \tag{2.10}$$

form which it is possible to obtain the initial conditions necessary to achieve the regular precession. For example, in order to observe this regular behavior, we should make the top spin around its axis with desired angular velocity $\dot{\psi}$ and set to this axis a rotation about the vertical with a certain angular velocity $\dot{\phi}$, namely the velocity which is characteristic of the subsequent precession. Otherwise, given all the other variables, using the (2.10) we could calculate the distance l or the angular velocity $\dot{\psi}$ required obtain steady precession.

In the usual case for tops and gyroscopes, $\dot{\phi}^2$ in (2.10) can be ignored since in general $\dot{\psi} \gg \dot{\phi}$. Therefore, for steady precession, the relationship between the precession angular velocity and the spin angular velocity is [47]

$$\dot{\phi} = \frac{mgl}{I \dot{\psi}} \tag{2.11}$$

We can note that $\dot{\phi}$ is independent of the nutation angle θ. In this case we can assume that the total angular momentum of the system is aligned with the z axis of the body-fixed reference frame (see Figure 2.10) although we must comprehend that this is just an approximation due to the initial hypothesis that $\dot{\psi} \gg \dot{\phi}$. In the exact theory the angular momentum vector is not aligned with the Z axis as for free-body motion, but is in the plane of z, Z, and rotates around the Z axis according to the applied external moment which is constant.

The result obtained in (2.11) can be found by a less complex approach considering that the spin velocity of a top is much greater than its precessional velocity. In this case the angular momentum vector can be assumed to be directed along the spin or z axis, $\boldsymbol{L} = I\dot{\psi}\boldsymbol{k}$ while the vector of torques can be expressed as $\boldsymbol{M} = l\boldsymbol{k} \times m\boldsymbol{g}$ (where $\boldsymbol{k}$ is a unit vector in the z direction). Substituting in (2.1) and assuming that the friction is insignificant, and thus $\dot{\psi}$ = constant, we can differentiate only $\boldsymbol{k}$ in $\boldsymbol{L}$ obtaining

$$I\dot{\psi}\frac{d\boldsymbol{k}}{dt} = \boldsymbol{k}l \times m\boldsymbol{g} \tag{2.12}$$

resulting in

$$\frac{d\boldsymbol{k}}{dt} = \dot{\boldsymbol{\phi}} \times \boldsymbol{k} \tag{2.13}$$

Therefore the angular velocity vector $\dot{\boldsymbol{\phi}}$ is

$$\dot{\boldsymbol{\phi}} = -\frac{ml}{I\dot{\psi}}\boldsymbol{g} \tag{2.14}$$

in agreement with the result obtained in (2.11). Referring to Figure 2.10 and to equation (2.14) it follows that the vector of the angular velocity of precession, $\dot{\boldsymbol{\phi}}$, is directed upward or downward along the Z axis depending on the sign of if $\dot{\psi}$ and the precession induced by gravity will occur in the same sense as the axial rotation of a top. Furthermore, the magnitude of the angular velocity of precession is inversely proportional to the angular velocity of the axial rotation and directly proportional to the distance between the pivot and the centre of mass. It is also curious to note that $\dot{\phi}$ is independent of the nutation angle [48].

Unsteady precession of a spinning top

In the general case of a spinning top in a gravitational field, its motion is a superposition of *torque-induced regular precession* and *torque-free nutation* of its z axis about the instantaneous angular momentum vector. Nutation of a fast-spinning gyroscope or top reveals itself as (small) vibration and shivering of the precessing axis. It is caused by a possible small deviation of the vector of angular momentum of the top from the axis of symmetry. This deviation is absent only for carefully chosen specific initial conditions.

In the most general case, the motion of a top will present the angular velocities $\dot{\phi}, \dot{\theta}, \dot{\psi}$, all varying with time. The most convenient way to determine the main characteristics of this motion, without actually solving the equations seen in (2.8), consists in developing the dynamic equations of the system using the Lagrangian formalism. The kinetic energy of a spinning top can be written as

$$\mathcal{T} = \frac{1}{2} I_0 \left(\omega_x^2 + \omega_y^2 \right) + \frac{1}{2} I \omega_z^2 \tag{2.15}$$

where $\omega_x, \omega_y, \omega_z$ are the components about the three principal axis of the vector angular velocity (see Figure 2.9) having the form indicated in (2.3).

Therefore the (2.15) becomes

$$\mathcal{T} = \frac{1}{2} I_0 \left(\dot{\phi}^2 \sin^2\theta + \dot{\theta}^2 \right) + \frac{1}{2} I \left(\dot{\phi} \cos\theta + \dot{\psi} \right)^2 \tag{2.16}$$

while the potential energy for a top is

$$\mathcal{V} = mgl \cos\theta \tag{2.17}$$

so that the Lagrangian is

$$\mathcal{L} = \mathcal{T} - \mathcal{V} = \frac{1}{2} I_0 \left(\dot{\phi}^2 \sin^2\theta + \dot{\theta}^2 \right) + \frac{1}{2} I \left(\dot{\phi} \cos\theta + \dot{\psi} \right)^2 - mgl\cos\theta \tag{2.18}$$

We can observe that the Lagrangian does not depend on the variables ϕ, ψ or t. Thus the angular momenta about the Z and z axis (see Figure 2.9) p_ϕ and p_ψ are invariant with time. To be more exact p_ϕ and p_ψ are the generalized momenta conjugate to the coordinates ϕ and ψ.

The general form of Lagrangian equations of motion may be written as

$$\frac{d}{dt}\left(\frac{\partial \mathcal{L}}{\partial \dot{q}_i} \right) - \frac{\partial \mathcal{L}}{\partial q_i} = 0 \tag{2.19}$$

where q_i denotes the generalized coordinates of the system that in our case are ϕ, θ, ψ. Therefore applying (2.19) to (2.18), we deduce the following equations of motion [47]

$$\begin{aligned}
&I_0 \dot{\phi} \sin^2\theta + I \left(\dot{\psi} + \dot{\phi}\cos\theta \right) \cos\theta = p_\phi = \text{const.} \\
&I_0 \left(\ddot{\theta} - \dot{\phi}^2 \sin\theta\cos\theta \right) + I \left(\dot{\psi} + \dot{\phi}\cos\theta \right) \dot{\phi} \sin\theta - mgl\sin\theta = 0 \\
&I \left(\dot{\psi} + \dot{\phi}\cos\theta \right) = p_\psi = \text{const.}
\end{aligned} \tag{2.20}$$

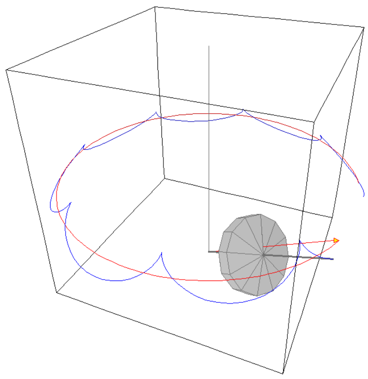

(a) Cuspidal precession

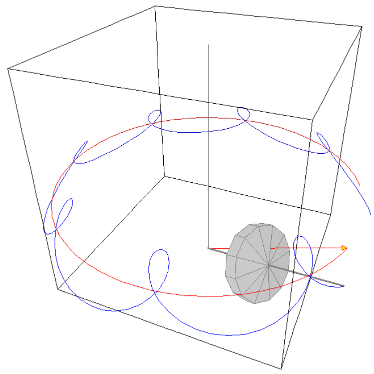

(b) Looping precession

Figure 2.12: Unsteady precession of a gyroscope

which can be rewritten in the following form

$$\dot{\phi} = \frac{p_\phi - p_\psi \cos\theta}{I_0 \sin^2\theta} \tag{2.21}$$

$$\dot{\psi} = \frac{p_\psi}{I} - \frac{p_\phi - p_\psi \cos\theta}{I_0 \sin^2\theta}\cos\theta \tag{2.22}$$

$$\ddot{\theta} = \frac{mgl}{I_0} - \left(\frac{\left(\frac{p_\phi}{I_0} - \frac{p_\psi}{I}\cos\theta\right)\left(\frac{p_\psi}{I} - \frac{p_\phi}{I_0}\cos\theta\right)}{\sin^3\theta}\right) \tag{2.23}$$

(2.23) can be solved using a numerical method while the the remaining equations are immediately solved given the initial conditions of the system and $\theta\,(t)$. We may therefore deduce that during this more general motion, all three Euler angles change with time, and the tip of the top traces out a motion, inscribed on the surface of a sphere, depending on the initial angular velocity of the top around the vertical, $\dot{\phi}$. If this angular velocity is zero than the tip of the top will trace a cycloid trajectory called cuspidal precession and illustrated in Figure 2.12. For different initial conditions the upper end of the axis will trace wavy or loopy trajectories referred to as unidirectional precession, looping precession observable in Figure 2.12. A wavy trajectory will fully straighten and transform itself into a circle only if the initial velocity of the axis is exactly equal to the velocity characteristic of regular precession or by the action of friction which could damp out the nutation with time.

Dynamics of a gyroscopic pendulum

In order to determine the main characteristics of the motion of a suspended rotating platform, illustrated in Figure 2.8, we shall consider the geometry of a

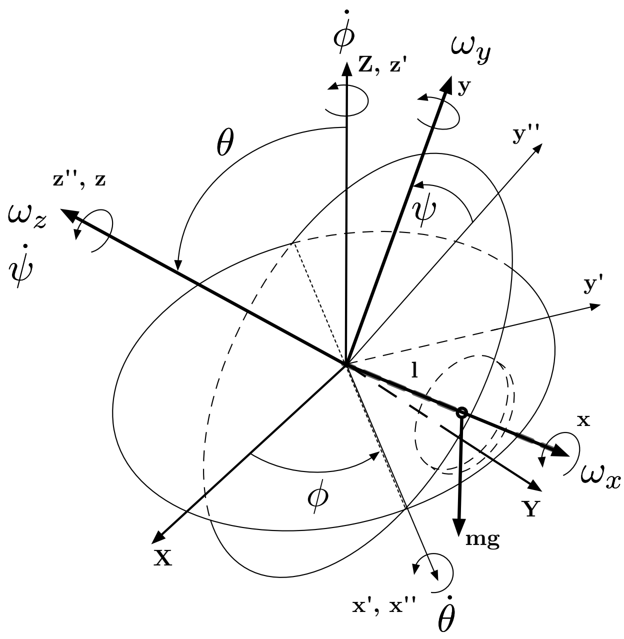

Figure 2.13: Illustration of a gyroscopic pendulum

gyroscopic pendulum depicted in Figure 2.13. It is essentially the same geometry of a symmetric spinning top, represented in Figure 2.9, with the only difference that this time the top is rotated 180° about the x axis. Hence the dynamics and the conditions for the regular precession of the platform about the vertical are almost identical to those already encountered in case of a symmetric spinning top.

The equations of motion of a gyroscopic pendulum can be readily obtained using the Lagrangian formalism and generalized coordinates, as it was done previously. Note that these equations will be similar to (2.20) given the almost identical geometry of the system.

Considering the expression of the kinetic energy given by (2.16) and choosing the potential energy to be zero when $\theta = 0$

$$\mathcal{V} = mgl\,(1 - \cos\theta) \tag{2.24}$$

the Lagrangian equations of motion become

$$\frac{d}{dt}\left[I_0\dot{\phi}\sin^2\theta + I\left(\dot{\psi} + \dot{\phi}\cos\theta\right)\cos\theta\right] = 0 \tag{2.25}$$

$$I_0\left(\ddot{\theta} - \dot{\phi}^2\sin\theta\cos\theta\right) + I\left(\dot{\psi} + \dot{\phi}\cos\theta\right)\dot{\phi}\sin\theta + mgl\sin\theta = 0 \tag{2.26}$$

$$\frac{d}{dt}\left(\dot{\psi} + \dot{\phi}\cos\theta\right) = 0 \tag{2.27}$$

From (2.27) we note that

$$\left(\dot{\psi} + \dot{\phi}\cos\theta\right) = \omega_z = \text{const.} = p_\psi \tag{2.28}$$

so that the remaining equations become

$$I\omega_z \cos\theta + I_0\dot{\phi}\sin^2\theta = \text{const.} = p_\phi \tag{2.29}$$

$$I_0\ddot{\theta} - I_0\dot{\phi}^2 \sin\theta\cos\theta + I\omega_z\dot{\phi}\sin\theta + mgl\sin\theta = 0 \tag{2.30}$$

The solution of equations (2.29) and (2.30) is not easy, even if we limit the variation of the nutation angle to small oscillations about the vertical. Nevertheless it is possible to analyze the motion of the gyroscopic pendulum without actually solving the previous equations.

First, we shall consider the case of pendulum displaced from the vertical through an angle θ_0 and having zero initial velocity around the Z axis, $\dot{\phi}_0 = 0$. In this case, with $\dot{\theta}_0 = 0 = \dot{\phi}_0$, and $\theta = \theta_0$, (2.29) now becomes [49]

$$I\omega_z\left(\cos\theta - \cos\theta_0\right) + I_0\dot{\phi}\sin^2\theta = 0 \tag{2.31}$$

We note that at first, after releasing the axis of the gyroscopic pendulum, it starts to fall toward the vertical under the influence of gravity, in accordance with our intuition. But from (2.31) we can notice that as soon as θ begins to differ from θ_0, $\dot{\phi}$ acquires a finite value, which will be positive or negative according to the sign of ω_z. As the pendulum approaches the vertical, the velocity of precession becomes greater and θ reaches its minimum value. We see, however, that the pendulum can never pass through the vertical since (2.31) cannot be satisfied by $\theta = 0$ unless $\omega_z = 0$. Once that θ has reached its minimum value it begins to increase again, and, in the absence of friction, it will finally reach its original value θ_0. This fact is proved by (2.30), which shows that, with decreasing θ and increasing $\dot{\phi}$, the acceleration $\ddot{\theta}$ passes through 0 and becomes negative, only to retrace its course when θ has passed its minimum. We may therefore conclude that the trajectory of the axis of symmetry of the wheel will consist of a series of oscillations toward the vertical, and back again, accompanied by a variable motion of precession. The greater the velocity of rotation of the wheel, the greater will be the frequency of these oscillations, as shown by the presence of the term $I\omega_z \sin\theta$ in (2.30). The variation of the precessional velocity will instead be confined between zero and a maximum value when θ has reached its minimum [49].

The type of motion just considered is illustrated in *a* and *b* figures of

Figure 2.14 which depicts the projections on a horizontal plane of trajectories of the upper end of the gyroscope axis. The red circle is the projection of the trajectory traced by the precessing angular momentum of a gyroscopic pendulum. The trace shown in a has been taken by imposing the maximum possible distance between the suspension point and the center of mass of the wheel, while the trace present in b was made with a much shorter pendulum. The greater effect of the gyroscopic action in the latter case is well marked by the small amplitude of the vibrations and the short distance between cusps. With a still shorter pendulum, the vibrations of θ might be so small that the motion could be indistinguishable from the regular precession. Theory indicates that when ω_z, is large, or l is small, the curve should consist of a series of infinitesimal cycloids. The sharply defined cusps show that the initial velocity of precession was zero.

If the initial value of $\dot{\phi}$, instead of being zero, is positive or negative, the velocity of precession can never become zero and thus instead of cusps at the end of each vibration, we shall have a smooth, wavy or loopy continuous curves as depicted in figures c and d of Figure 2.14 [49].

The effect of friction until now was always neglected since the presence of frictional forces inside the equations of motion would have made their analysis more complicated. But it is not necessary to enter into the analytical treatment in order to reach the conclusion that the effect of friction is to reduce the motion to one of steady precession. This result is accomplished by causing the increase of the velocity of precession. This paradoxical conclusion, that friction may produce an increased velocity of precession, represents only another of the puzzling peculiarities of the gyroscope. Noticing that the oscillatory motion of the axis of a gyroscopic pendulum is quite rapid as compared with its motion of precession, we see that frictional forces are much more important in the former case than in the latter. The effect of friction will thus make the average value of θ smaller by damping out its fast vibrations. But when θ diminishes, $\dot{\phi}$ must increase, as shown in (2.29), since the angular momentum about the vertical, p_ϕ , must remain constant during the motion. So as long as the opposition to precession is small compared to the other frictional forces, the results will therefore be as stated above. Figure 2.15 allows us to observe this behavior due to friction. It shows that the trajectory at first loopy is gradually tending to a circle corresponding to the steady forced precession [49].

The criterion for the steady precession of a gyroscopic pendulum is most easily obtained directly from (2.30) by imposing that the platform has a constant rotational speed $\dot{\psi} = \dot{\psi}_0$ about its principal axis, and that it precesses with constant angular velocity $\dot{\phi} = \dot{\phi}_0$, while maintaining a constant angle of nutation

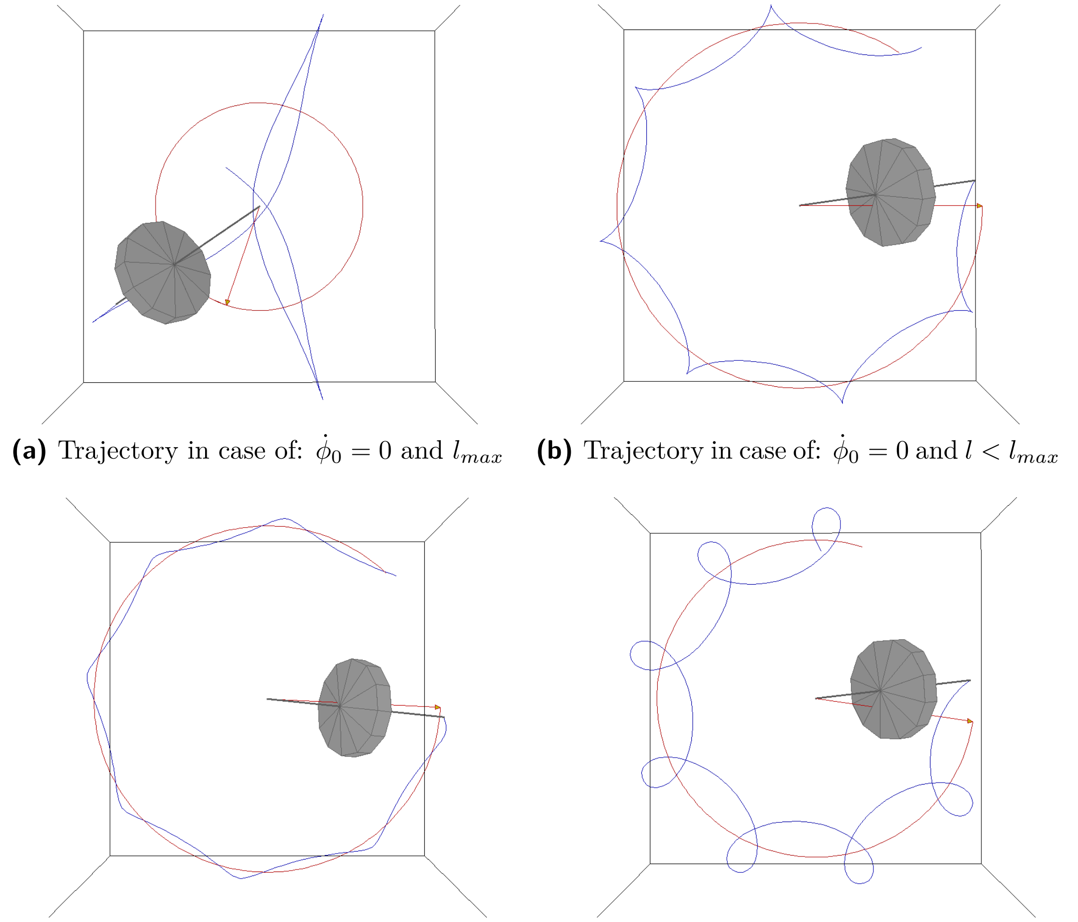

(a) Trajectory in case of: $\dot{\phi}_0 = 0$ and l_{max} **(b)** Trajectory in case of: $\dot{\phi}_0 = 0$ and $l < l_{max}$

(c) Trajectory in case of: $\dot{\phi}_0 > 0$ and $l < l_{max}$ **(d)** Trajectory in case of: $\dot{\phi}_0 < 0$ and $l < l_{max}$

Figure 2.14: Traces of a gyroscopic pendulum

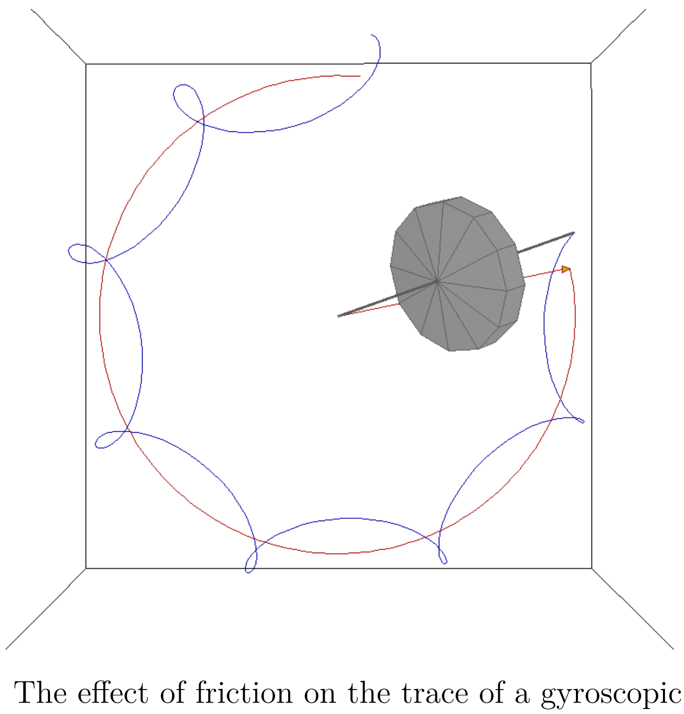

Figure 2.15: The effect of friction on the trace of a gyroscopic pendulum

$\theta = \theta_0$ and thus $\dot{\theta} = \ddot{\theta} = 0$. Therefore (2.30) reduces to

$$(I_0 - I)\,\dot{\phi}^2 \cos\theta - I\dot{\phi}\dot{\psi} = mgl \tag{2.32}$$

form which it is possible to obtain the initial conditions necessary to achieve the regular precession of a gyroscopic pendulum, similarly to the studied case of a symmetric spinning top. For example, considering $\dot{\psi}_0 = \dot{\phi}_0 = 0.0698\,\mathrm{rad/s}$, $\theta_0 = 0.1745\,\mathrm{rad/s}$, $m = 15\,\mathrm{kg}$ and the radius of the platform $r = 1\,\mathrm{m}$, the condition necessary to obtain the regular precession of the platform, around the rigid cable, is represented by the distance l between the suspension point of the platform and its center of mass and it has to be $l = 1.3012 \times 10^{-4}\mathrm{m}$.

Furthermore if $\dot{\psi} \gg \dot{\phi}$, as in case of a spinning top, the term $\dot{\phi}^2$ in (2.32) can be ignored and the relationship between the precession angular velocity and the spin angular velocity becomes

$$\dot{\phi} = -\frac{mgl}{I\dot{\psi}} \tag{2.33}$$

which is identical to (2.11), a part from the minus sign, given the almost identical geometry of the problem.

In conclusion, we can say that the regular precession of a suspended rotating platform (object of study) will occur only if precise initial conditions are imposed. The desired criterion for steady precession of the system can be obtained from (2.32) or, if $\dot{\psi} \gg \dot{\phi}$, from (2.33) although in order to obtain reasonable distances (of order of few centimeters) higher spinning velocities of the platform must be considered. The frictional forces, that are not taken into account inside previous equations, could pose a problem in particular cases but in general they will just contribute to the dumping of the nutation and thus contribute to the desired motion of the platform.

2.2.3 Robotic simulation system

An active robotic gravity compensation system represents a valuable simulation method of difficult operations in the microgravity environment, such as the capture phase of DEOS, since it uses the combination of the numerical model of the system and its real hardware taking advantages of both in order to achieve a more realistic simulation conditions [46].

The concept of such simulation system for the DEOS mission consists basically of:

1. a multi-body dynamic model of the system used to predict the motion and

the dynamic responses of the spacecrafts during capture phase;

2. a 6 DOF robotic system to perform the dynamic motion of the two spacecrafts generated by the aforementioned model;

3. a mockup of at least the client spacecraft in order to achieve real physical contact during the simulation.

The conceptual representation of two possible laboratory setups of the hardware-in-the-loop (HIL) simulation method is depicted in Figure 2.16. In both concepts, the target satellite is mounted on the end-effector of Robot T while the manipulator of the chaser satellite, Robot C, is mounted either on the end-effector of Robot B or is fixed on the laboratory floor. In figure *a*, the dynamics of the Target, and thus the motion of Robot T, is given by a mathematical model which computes the state vector (position and attitude of the spacecraft) based on relevant environmental and control forces and torques. The free-floating Robot C is mounted on the end-effector of Robot B fixed to the laboratory floor. For a given input joint motion of Robot C, the dynamical coupling between the manipulator and its base causes the motion of the end-effector of Robot B computed using the equations of free-floating robot. This results, during the simulation, in the same motion of the robots that would experience an external observer of the scene while watching from the inertial reference frame. In figure *b*, on the other hand, the base of Robot C is fixed to the floor. Its motion is calculated, as before, using the equations of free-floating robot, for a given input joint motion of Robot C. The consequent different position of its end-effector is implemented either directly by Robot C, using the the aforementioned equations, or by Robot T, based on the motion of the target relative to the base of Robot C. The resulting motion of the robots in this latter case will be the same as the one that would experience an observer fixed with respect to the base of Robot C. Compared with the previous concept it is clear that the latter provides a natural way for training human operators for tele-presence control mode of the manipulator. Furthermore, it can be realized with off-the-shelf robot hardware while the first concept requires special design of two robots mounted in series [8].

The Vehicle Emulation System Model II (VES II) developed at Massachusetts Institute of Technology (MIT), in 1994, is an example of the first concept illustrated in figure *a* of Figure 2.16. The mechanical system was based on a Stewart platform, illustrated in Figure 2.17, with six position-controlled hydraulic actuators using admittance control [7]. Another example of this kind, is EPOS facility developed at DLR for simulating satellite rendezvous and capture operations (see Figure 2.7). This facility comprises a hardware-in-the-loop contact dynamics sim-

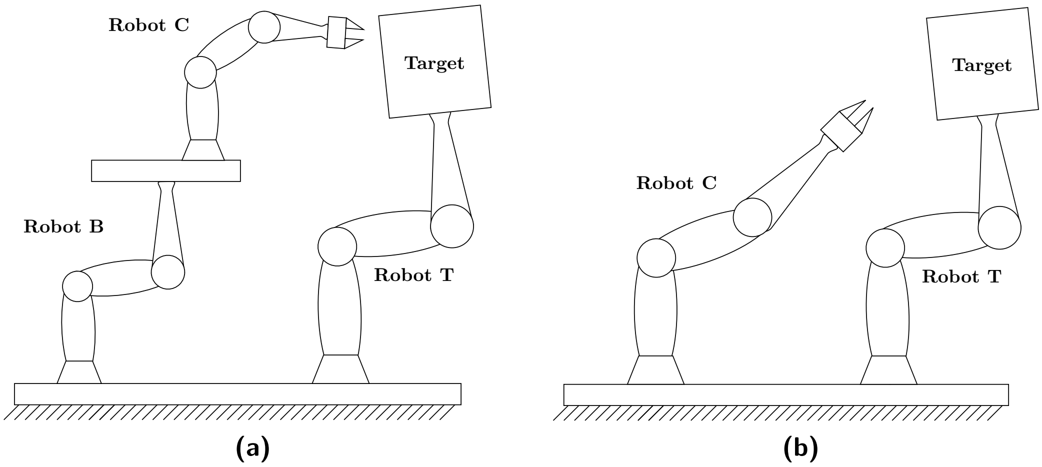

Figure 2.16: A schematic representation of two possible laboratory simulation concepts

ulator using two giant KUKA robots for physical simulation of full 6 DOF motion of spacecrafts [46]. The Task Verification Facility of SPDM [50] and the works of S. K. Agrawal et al. [8] , in 1996, and of W. Xu at al. [9], in 2006, are instead the examples of laboratory simulators developed having in mind the second concept of active robotic gravity compensation system depicted in figure *b* of Figure 2.16.

The design of the ground simulation facility considered by our group at the DLR Institute of Robotics and Mechatronics (IRMC) is based on the second concept of the HIL simulation method. It consists basically of two Light-Weight Robots (LWRs) of the third generation used to realize the motion of the end-

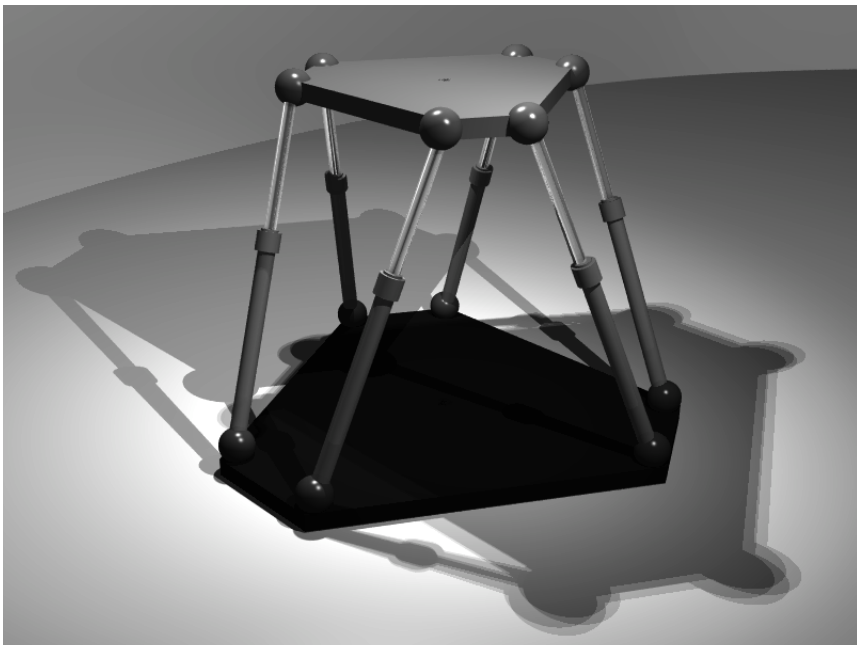

Figure 2.17: An example of a Stewart platform

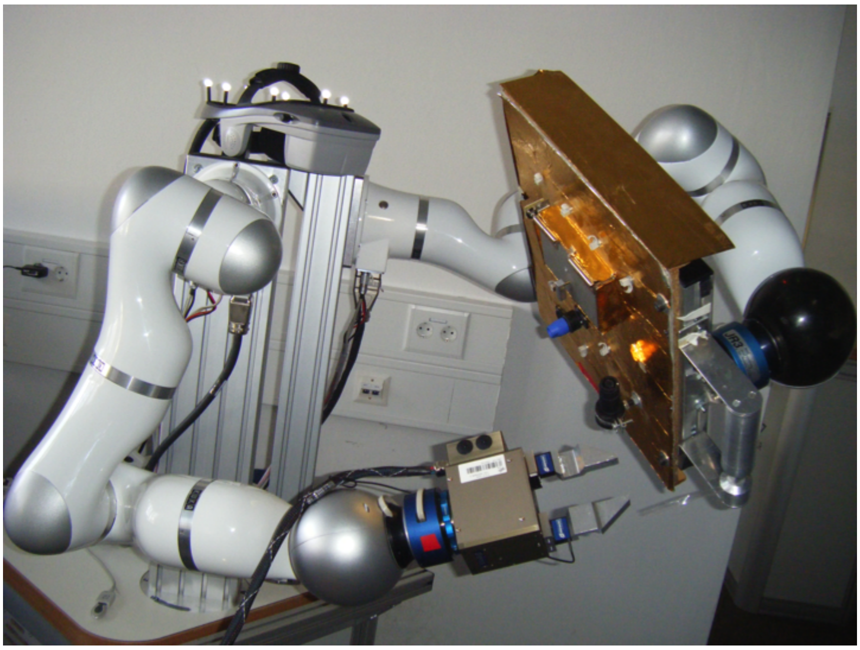

Figure 2.18: Laboratory setup of the ground simulation facility developed at DLR IRMC [10]

effector of the space manipulator and of the target satellite relative to the base of the space robot. This kind of setup, visible in Figure 2.18, was considered since it requires relatively simple hardware, already present in the tele-presence laboratory of DLR, and at the same time it offers significant flexibility as it is possible to verify different capture strategies of spacecrafts of almost any geometry and inertial parameters with small modifications.

The designed system depends on the notions of the dynamic emulation and the kinematic equivalence that require further explanation in oder to fully comprehend the basic idea behind the developed simulator. Dynamic emulation means that the behavior of the whole system, including the space manipulator, its base and the Target, are emulated by the equations of motion. Kinematic equivalence indicates that the motion of the end-effector of the space manipulator is achieved by the end-effector of the robot present in the laboratory and thus their motions are equivalent.

Figure 2.19 and Figure 2.20 illustrate two possible modes of the kinematic equivalence and thus two different simulation concepts based on the second concept of the HIL simulation method. In both, the motion of the end-effector of the space robot, represented by the dashed Robot S, is implemented by the chaser robot (Robot C) while the motion of the Target, represented by the mockup mounted on the end-effector of the target robot (Robot T) is performed by the motion of the latter. Before evidencing the difference between the two modes of

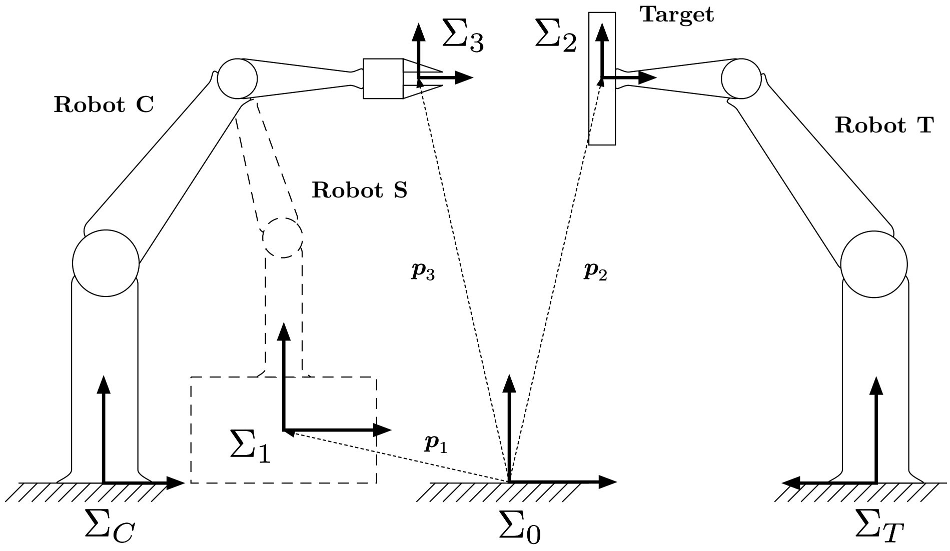

Figure 2.19: First mode of kinematic equivalence

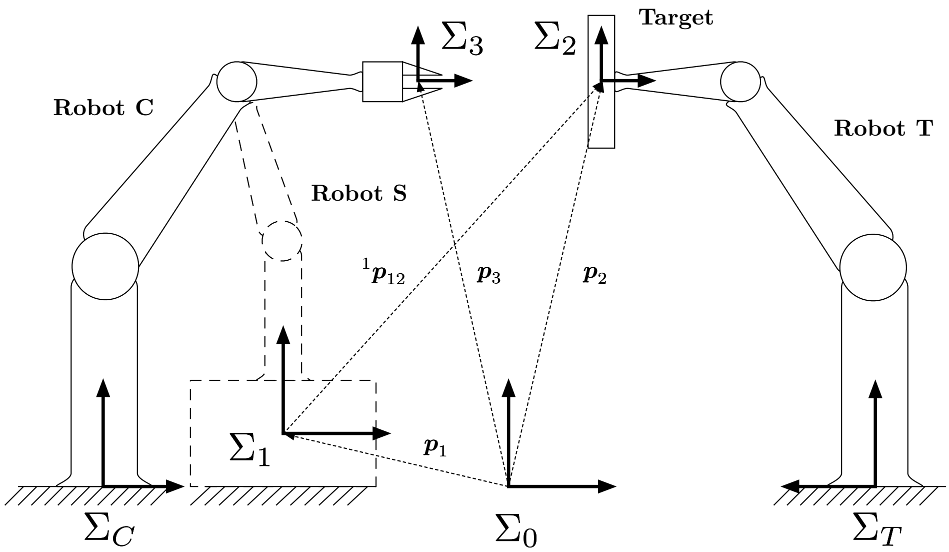

Figure 2.20: Second mode of kinematic equivalence

the kinematic equivalence it is necessary to define the frames and notations that will be used and that are visible in Figure 2.19 and in Figure 2.20.

Σ_i indicates the reference frames: of the laboratory (if $i = 0$), of the origin of the free-floating base of the Robot S (if $i = 1$), of the Target (if $i = 2$) and of the Chaser's end-effector (if $i = 3$); Σ_C, Σ_T on the other hand are the frames of the bases of Robot C and Robot T respectively;

${}^k\boldsymbol{p}_{ij} \in \mathbb{R}^{3\times1}$ represents the position vector from the origin of Σ_i to that of Σ_j, expressed with respect to the coordinate frame Σ_k; if Σ_k is the laboratory frame, the superscript k can be omitted;

${}^i\boldsymbol{R}_j \in \mathbb{R}^{3\times3}$ denotes the rotation matrix of the frame Σ_j with respect to the frame Σ_i;

${}^i\boldsymbol{T}_j \in \mathbb{R}^{4\times4}$ identifies the homogeneous transformations matrix describing the position and orientation of the frame Σ_j with respect to the frame Σ_i.

The first of the two modes of the kinematic equivalence is depicted in Figure 2.19. In this case Robot C and Robot T are controlled to implement the absolute motion (i. e. in the laboratory coordinate system, Σ_0) of the end-effector of Robot S and of the Target causing the motion of the system that would perceive an external observer while watching from the laboratory reference frame. The absolute pose (position and orientation in the coordinate system of the laboratory, Σ_0) of the space robot's end-effector is determined according to the dynamics of the space robot while the absolute motion of the Target is calculated according to its equations of motion. Then Robot C and Robot T are controlled to implement the motion of the end-effector and of the Target, respectively. In the end it is important to stress that in this mode the bases of Robot C and Robot T are considered fixed in the laboratory coordinate frame (i. e. Σ_C and Σ_T are considered to be fixed with respect to Σ_0) while the base of Robot S is free to move due to the dynamic coupling between the manipulator and its spacecraft (i. e. Σ_1 is considered to be free-floating relative to Σ_0) [9].

Differently, in the second mode of the kinematic equivalence, illustrated in Figure 2.20, Σ_C and Σ_T are considered to be fixed with respect to Σ_1, which in turn is considered to be fastened in the inertial coordinate system. Furthermore, at $t = 0\,\mathrm{s}$, $\Sigma_1 \equiv \Sigma_0$. On the other hand, the laboratory coordinate system, Σ_0 , is considered to be mobile with respect to the inertial reference frame so that Robot C and Robot T are used to realize the motion of the end-effector and of the space target relative to the space base. In other words, the experiment system should simulate the capturing process observed from the base of the space robot. In order to achieve this, at first, the pose of Σ_0 relative to Σ_1 ($[{}^0\boldsymbol{T}_1]^T$) is determined by the dynamic model of the free-floating manipulator. Than, given the pose of the target spacecraft with respect to Σ_0 (${}^0\boldsymbol{T}_2$), calculated as in the first mode of the kinematic equivalence, the position and the orientation of the Target with respect to the coordinate frame of the base (${}^1\boldsymbol{T}_2$) is determined and used as an input for Robot T. Mathematically this consists in finding the variables ${}^1\boldsymbol{p}_{12}$ and ${}^1\boldsymbol{R}_2$ in the following manner

$$ {}^1\boldsymbol{p}_{12} = \left({}^0\boldsymbol{R}_1\right)^{-1}(\boldsymbol{p}_2 - \boldsymbol{p}_1) = {}^1\boldsymbol{R}_0\,(\boldsymbol{p}_2 - \boldsymbol{p}_1) \tag{2.34} $$

$$ {}^1\boldsymbol{R}_2 = \left({}^0\boldsymbol{R}_1\right)^{-1}{}^0\boldsymbol{R}_2 = {}^1\boldsymbol{R}_0{}^0\boldsymbol{R}_2 \tag{2.35} $$

so that in the end we can obtain

$$ {}^1\boldsymbol{T}_2 = \begin{bmatrix} {}^1\boldsymbol{R}_2 & {}^1\boldsymbol{p}_{12} \\ \boldsymbol{0}^T & 1 \end{bmatrix} \tag{2.36} $$

where $\boldsymbol{0}^T = [0,0,0]$ vector.

Note that the pose of Σ_3 with respect to Σ_1 is obtained directly from the control algorithms of Robot C and it doesn't take into account the motion of the base which is simulated directly by Robot T, differently from the first mode.

The ground simulation facility developed by the DLR IRMC rests its foundations on this second mode of the kinematic equivalence thus satisfying the need for a relatively simple and inexpensive hybrid simulation system that could conveniently be used also for the training human operators of future OOS missions.

3 Realization of the Hardware-in-the-Loop Simulation Concept

The HIL simulation concept developed at the DLR IRMC is a hybrid method that combines the math model of the system with the real hardware in order to emulate the motions of the space robot, in microgravity environment, during the capture phase of the DEOS mission. The system is based on the multimodal haptic Human Machine Interface (HMI), composed of two Light-Weight Robots fixed to the rigid platform, in a configuration similar to the human torso. Therefore, this chapter starts with Section 3.1, where the overview of the ground experimental setup can be found. Than, in the first part of Section 3.2, dynamic equation of the free-floating robot is analyzed while the second part illustrates the virtual models of the space robot developed with the 3D multi-body simulation software SIMPACK. Section 3.3 outlines two Simulink models of the experimental system together with preliminary analysis of the adopted simulation concept. In the end, Section 3.4 describes the realization process of the new Target's mockup starting from the design of the old one.

3.1 System Overview

The ground experiment system developed at the DLR IRMC, for the simulation of the capture maneuver of the DEOS mission, is composed of: two Light-Weight Robots (LWRs), of the third generation, fixed to a rigid platform by means of a supporting structure made of aluminum, a target satellite mockup and a gripper.

The configuration of two LWRs is visible in figure a of Figure 3.1 while the figure b illustrates the position of the reference frames Σ_1, Σ_2 and Σ_3 in a virtual model of the hybrid system. For the definition of the reference frames see

Figure 2.20 on page 60. In this setup, for a joint input command of Robot C and thus of Robot S, the motion of its base is computed using the model of the free-floating robot. The latter is than used to evaluate the joint input command of Robot T in order to obtain the motion of the target satellite relative to the base of the space robot, assumed fixed. Furthermore, during a physical contact, forces and moments generated by the manipulator of the chaser spacecraft will be measured by sensors mounted on the wrist of Robot T and fed back to the satellite simulator affecting the motion of the Target. Note that during this phase the space robot's base is assumed to be fixed in inertial reference frame. This hypothesis can be satisfied by an AOC system capable of generating external forces and moments to actively counteract any motion of the servicer spacecraft during the contact phase of the capture maneuver.

The chosen HIL system design presents several advantages over the similar robotic systems mentioned in Subsection 2.2.3 on page 56:

1. it uses two advanced light-wight robots making the whole system less complex, more reliable and relatively inexpensive for the verification of the planning and control algorithms of free-floating robots;
2. the time interval between system design and its realization, generally present and most of the time considerable, was almost inexistent given that the conceived HIL system uses the human-scale bimanual haptic interface setup already present in the telepresence laboratory of the DLR IRMC;
3. the geometry and inertial parameters of space robot are almost unlimited, given that the motion of its base is obtained from its dynamic model;
4. it provides a natural way for training human operators for tele-presence control mode;
5. the system is extendable by small modifications of the implemented dynamic models of the spacecrafts.

However, it must be noted that the selected design exhibits few shortcomings:

1. the motion of the target satellite cannot be completely arbitrary since the workspace of the system is limited;
2. the workspace of the Robot C isn't equal to that of the DEOS space manipulator since their dimensions aren't the same;
3. the mockup of the target satellite has to be as light as possible and in any case it cannot exceed 14 kg;

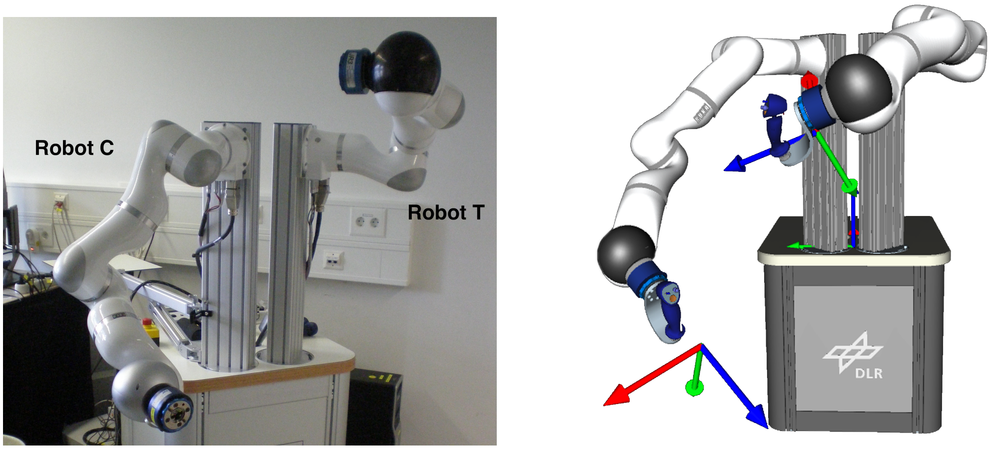

(a) Real system **(b)** Virtual system

Figure 3.1: Ground experiment system developed at the DLR IRMC

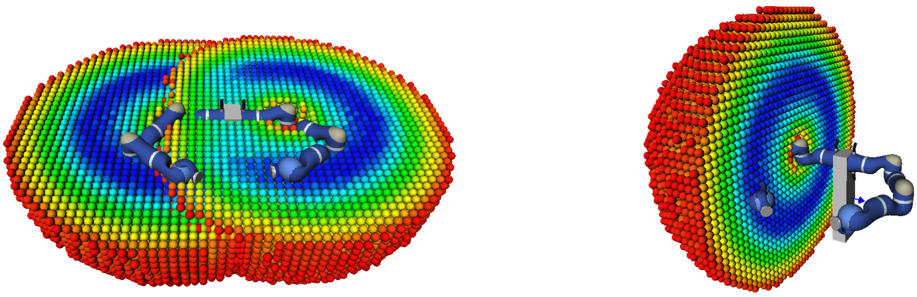

(a) Horizontal workspace **(b)** Vertical workspace

Figure 3.2: Workspace of the HMI system [51]

Since the system was originally designed as a haptic Human Machine Interface (HMI), the workspace of the HIL system is similar to that of human arms and can be seen in Figure 3.2. The figure represents two sectional drawings of the workspace of the haptic HMI system of the first generation, similar to the hybrid experiment system developed. The spheres represent possible end-effector positions in the overlapping workspaces of the two manipulators. Blue spheres indicate points inside the workspace at which the robot can reach more than 75 % of all possible three dimensional orientations, whereas red spheres mark points with less than 8 % respectively [51].

The specifications of the HIL system are indicated in Table 3.1 evidencing higher agility and highly dynamic behavior compared to standard industrial robots usually employed for this kind of facility.

The core of the system is represented by the LWR III, visible in Figure 3.3. The LWR is a light-weight, flexible, revolute joint robot, especially suited for tasks that require high manipulation capabilities in a changing workspace with

Table 3.1: Specifications of the ground experiment system [51]

Dynamic mass [kg]	2×14
Max. payload [kg]	2×14
Max. Span [mm]	2×936
N° of joints	2×7
Sensors (each wrist)	6 DOF Force/Torque sensor
Sensors (each joint)	2 Position, 1 Torque sensor
Sampling Rates [kHz]	Current control: 40 Joint internal: 3 Cartesian: 1
Motors	DLR-Robodrive
Gears	Harmonic Drive

unpredictable obstacles. The light-weight robot of the third generation has a modular design featuring individual joints connected via carbon-fiber structures. Furthermore, the robot can be connected to a tool by a standard robot interface flange and it can also be operated over internal supply lines [52]. The kinematics of the robot, with its seven degrees of freedom, allows it advanced flexibility, in comparison to standard industrial robots. In addition, the redundant kinematics allows the null-space movement, similarly to the human arm, which is valuable for avoiding collisions and optimizing the robot's configuration. This means that the robot is able to maintain a fixed pose of its end-effector, while moving freely its elbow. Other features of this third generation of LWR are: very light gears, powerful motors and weight optimized brakes. These brakes require power supply to be released and they are activated as soon as the power is off. The electronics is integrated in each joint, including the power converters so that no bulky external rack, known from standard industrial systems, is needed. An outstanding ratio of payload to total mass of the robot is another characteristic of the new LWR. The robot itself has a total mass of 14 kg and is able manage loads up to 14 kg achieving 1:1 load to weight ratio. Each of the LWRs joints has a motor position sensor and a sensor for joint position and joint torque enabling the control of the robot in position, velocity and torque [51]. Being able to control the robot at an update rate of 1 kHz allows a highly dynamic behavior and reduces the responding time of the robots making it perfect candidate for a HIL simulator. An additional 6 DOF force-torque sensor is mounted on the wrist of each robot allowing to measure precisely external forces applied to the end-effector, e. g. the

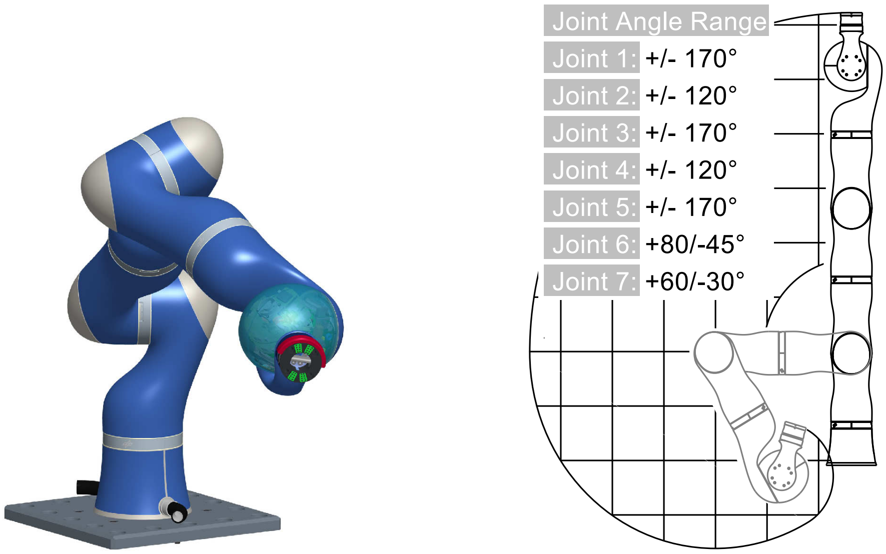

(a) CAD model **(b)** Joint angle range

Figure 3.3: DLR Light Weight Robot III (credit: DLR)

forces applied by a manipulator during the capture phase.

3.2 Free-floating Robot Model

3.2.1 Dynamic equation

The dynamic equation of a space robot, considering as the generalized coordinates the absolute linear and angular velocities of the base $\dot{\boldsymbol{x}}_b = \left[\boldsymbol{v}_b^T, \boldsymbol{\omega}_b^T\right]^T \in \mathbb{R}^{6\times 1}$ with respect to the inertial reference frame and the motion rate of the joints $\dot{\boldsymbol{q}} \in \mathbb{R}^{n\times 1}$, is generally expressed in the following form [23]

$$\begin{bmatrix} \boldsymbol{H}_b & \boldsymbol{H}_{bm} \\ \boldsymbol{H}_{bm}^T & \boldsymbol{H}_m \end{bmatrix} \begin{bmatrix} \ddot{\boldsymbol{x}}_b \\ \ddot{\boldsymbol{q}} \end{bmatrix} + \begin{bmatrix} \boldsymbol{c}_b \\ \boldsymbol{c}_m \end{bmatrix} = \begin{bmatrix} \boldsymbol{F}_b \\ \boldsymbol{\tau}_m \end{bmatrix} + \begin{bmatrix} \boldsymbol{J}_b^T \\ \boldsymbol{J}_m^T \end{bmatrix} \boldsymbol{F}_h \tag{3.1}$$

The kinematic relationship between the pose of the end-effector, the centroid of the base and the joint velocity of the manipulator, is expressed as follows

$$\dot{\boldsymbol{x}}_e = \boldsymbol{J}_m \dot{\boldsymbol{q}} + \boldsymbol{J}_b \dot{\boldsymbol{x}}_b \tag{3.2}$$

$$\ddot{\boldsymbol{x}}_e = \boldsymbol{J}_m \ddot{\boldsymbol{q}} + \dot{\boldsymbol{J}}_m \dot{\boldsymbol{q}} + \boldsymbol{J}_b \ddot{\boldsymbol{x}}_b + \dot{\boldsymbol{J}}_b \dot{\boldsymbol{x}}_b \tag{3.3}$$

where the used symbols are defined as:

$\boldsymbol{H}_b \in \mathbb{R}^{6\times 6}$ inertia matrix of the base;

$\boldsymbol{H}_m \in \mathbb{R}^{n\times n}$ inertia matrix of the manipulator arm having n joints;

$\boldsymbol{H}_{bm} \in \mathbb{R}^{6\times n}$ coupling inertia matrix between the base and the manipulator;

$\boldsymbol{c}_b \in \mathbb{R}^{6\times 1}$ nonlinear Coriolis and centrifugal forces of the base;

$\boldsymbol{c}_m \in \mathbb{R}^{n\times 1}$ nonlinear Coriolis and centrifugal forces of the manipulator;

$\boldsymbol{F}_b \in \mathbb{R}^{6\times 1}$ external forces and moments exerted on the centroid of the base;

$\boldsymbol{F}_h \in \mathbb{R}^{6\times 1}$ external forces and moments exerted on the end-effector of the manipulator;

$\boldsymbol{\tau}_m \in \mathbb{R}^{n\times 1}$ joint torques of the manipulator;

$\boldsymbol{J}_b \in \mathbb{R}^{6\times 6}$ Jacobian matrix dependent on the base motion;

$\boldsymbol{J}_m \in \mathbb{R}^{6\times n}$ Jacobian matrix dependent on the motion of the manipulator;

$\boldsymbol{x}_b \in \mathbb{R}^{6\times 1}$ position/orientation of the centroid of the base;

$\boldsymbol{x}_e \in \mathbb{R}^{6\times 1}$ position/orientation of the end-effector;

$\boldsymbol{q} \in \mathbb{R}^{n\times 1}$ vector of joint variables of the space manipulator having n degrees of the freedom.

For a free-floating manipulator in orbit, its base is free to move in inertial space due to the motion of the robotic arm without any external forces or moments. The gravity forces exerted on the system can be neglected so that the nonlinear term of the base becomes $\boldsymbol{c}_b = \dot{\boldsymbol{H}}_b\boldsymbol{v}_b + \dot{\boldsymbol{H}}_{bm}\boldsymbol{\omega}_b$. Furthermore, since we are considering the free-floating behavior of the system only during the approach phase, the external forces/moments applied to the end-effector in this pre-contact interval can be considered zero. Thus, integrating only the equation of motion of the base, in (3.1), with respect to time, we obtain the expression of total momentum of the system as [23]

$$\mathscr{L} = \boldsymbol{H}_b\dot{\boldsymbol{x}}_b + \boldsymbol{H}_{bm}\dot{\boldsymbol{q}} = 0 \tag{3.4}$$

The absolute velocity of the base can be than obtained as

$$\dot{\boldsymbol{x}}_b = -\boldsymbol{H}_b^{-1}\boldsymbol{H}_{bm}\dot{\boldsymbol{q}} \tag{3.5}$$

so that the absolute pose of the base, necessary for computing the relative motion of the target satellite with respect to the space base, ${}^1\boldsymbol{T}_2$, can be determined form (3.5) by the Runge-Kutta method, for example.

However, note that the absolute pose of the base, used inside the developed ground experiment system, is directly measured from the numerical model of the space robot (known as the "truth model"), instead of being calculated using (3.5). This model was developed using the 3D multi-body simulation software SIMPACK.

This design choice was made in order to develop the model that is also suitable both to evaluate the performance of the ground experiment system and to visualize intuitively the dynamics of the space system during the capture phase.

Hereafter, two developed numerical models of the free-floating system are illustrated, differing from each only for the dimensions and the type of the robotic manipulator mounted on the chaser spacecraft.

3.2.2 Model with DEOS' manipulator

The first model of the free-floating robot was developed in SIMPACK according to the specifications of the DEOS' Chaser spacecraft, indicated in Table 2.1 on page 30 and to the parameters of its robotic arm, illustrated briefly in Subsection 2.1.2 on page 34. The model, depicted in Figure 3.4, consist of two basic parts: the carrier satellite and the 7 DOF robotic arm. The servicer spacecraft is considered to have the mass of 724.10 kg and the following dimensions: $1.74 \times 1.74 \times 2\,\mathrm{m}$ (H×W×L). The manipulator, on the other hand, has the mass of 27.1 kg (without the tool) and the overall length of 3.227 m. Detailed parameters used for the development of the model can be found in Section A.2 on page 133. Note that the inertial reference frame, Σ_0, and the one of the base, Σ_1, are initially considered coincident (see Figure 3.4). Since we are interested to simulate the free-floating behavior of the space robot, there are no external forces or torques applied to the centroid of the base so that its motion is exclusively caused by the motion of the robotic arm. The model of the manipulator can be controlled either by commanding desired joint torques or joint angles while the motion of any part of the system can be measured by virtual sensors.

The advantage of a model developed with SIMPACK lies in the export function of the software which gives us the possibility to intuitively develop the model of the desired multi-body systems, within SIMPACK, and subsequently export it as a single closed block that can easily be integrated in any Simulink's model, having the desired input and output signals. Furthermore, it is possible to perform the dynamical analysis of the system within SIMPACK and easily compare the desired output data with the results obtainable in MATLAB or Simulink.

The verification of the model was done using a C++ model of the system,

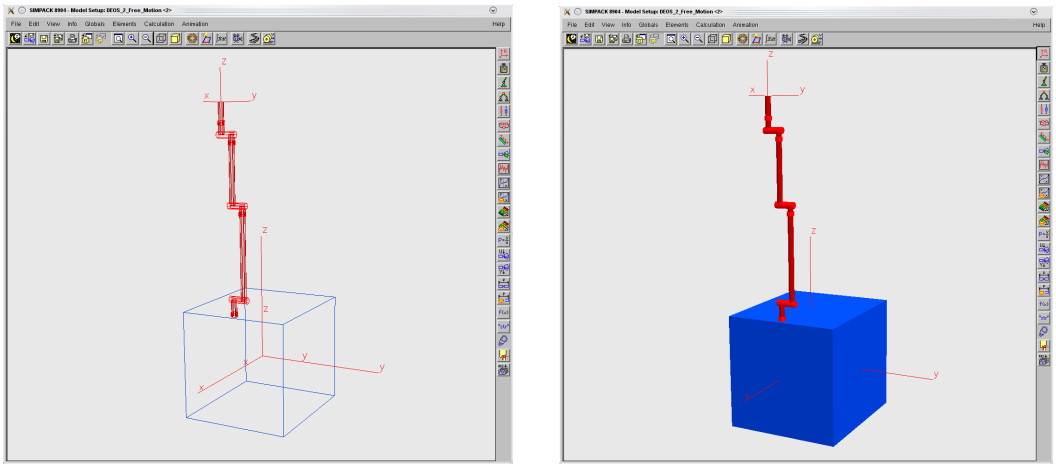

(a) **(b)**

Figure 3.4: I model of the free-floating robot in SIMPACK

developed by Lampariello, R., based on the equations of the kinematics and dynamics (see 3.5) of the space robot. The kinematics of the robotic arm and the dynamics of the base were verified, for a given joint configuration of the manipulator, by comparison between the two aforementioned models of the pose vector $\boldsymbol{x}_e = [\boldsymbol{p}_e, \boldsymbol{\phi}_e]$ and $\boldsymbol{x}_b = [\boldsymbol{p}_b, \boldsymbol{\phi}_b]$ of the end-effector and base respectively. Nevertheless, this model was only the demonstration of the feasibility of the original idea of creating a model of the system with SIMPACK.

The final model of the free-floating manipulator, needed in HIL simulation concept, was developed having in mind that in order to create a truthful motion of the base in microgravity environment the robotic arm inside the model has to present the same characteristics of the real employed hardware, which in our ground experiment facility is the LWR III.

3.2.3 Model with LWR III

The second model of the space robot, depicted in Figure 3.5, was developed considering the dimensions of the carrier spacecraft equal to that of the first model and the parameters of the robotic arm to that of LWR III, presented briefly in Table 3.1. Section A.3 on page 135 describes the details of the LWR III system used to generate the aforementioned model. This choice was mandatory in order to achieve reliable results of the simulations.

Starting from this single model, different versions of the chaser spacecraft were developed, within SIMPACK, with intention to create a great variety of models, each having different inertial parameters, and thus be able to analyze the responses of the ground simulation system to different amplitudes of motion

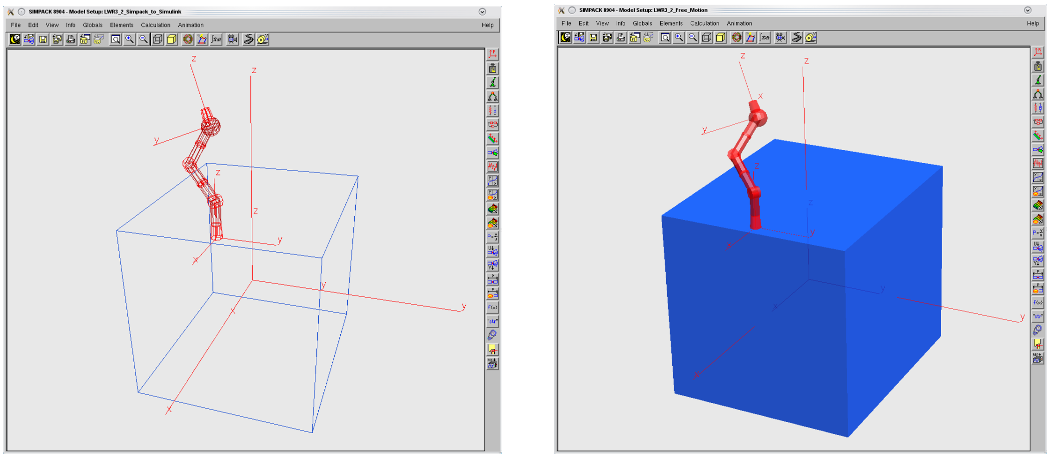

(a) (b)

Figure 3.5: II model of the free-floating robot in SIMPACK

of the base.

The first group of models was created considering the dimensions of the servicer spacecraft constant and equal to $1.74 \times 1.74 \times 2\,\mathrm{m}$ (H×W×L) while changing its mass and thus its inertia matrix. The masses considered are: 724.10 kg, 181.025 kg, 45.256 kg, 11.314 kg, and 2.829 kg. Note that all masses are submultiples of 724.10 which is the original mass of the chaser spacecraft.

The second group of models was developed considering instead the dimensions of the servicer variable with its mass. In particular, in order to obtain the inertia properties of all models proportional to those of the original one according to their dimensions, the density of each model is considered to be equal to the one of the original spacecraft, which is $119.583\,\mathrm{kg}/\mathrm{m}^3$. This way by imposing the desired mass it was possible to obtain the volume and thus the dimensions of the carrier spacecraft. The masses considered are the same as in the first group of models. Detailed informations about the dimensions of the chaser spacecraft used in various models can be found in Section A.4 on page 137.

3.3 Simulink Model of the HIL Simulation System

The main interface of the HIL simulation system is the Simulink model Human Machine Interface 2010 (HMI2010) developed by the IRMC of the German Aerospace Center. By means of HMI2010, visible in Figure 3.6, an operator can simulate or control the motion of the human-scale bimanual haptic interface, depicted in Figure 3.1. The simulation of the desired behavior of the two LWRs can be done by means of a *demo* located inside the block *demos* of the HMI2010 model. The same motion can be than performed on the real hardware by com-

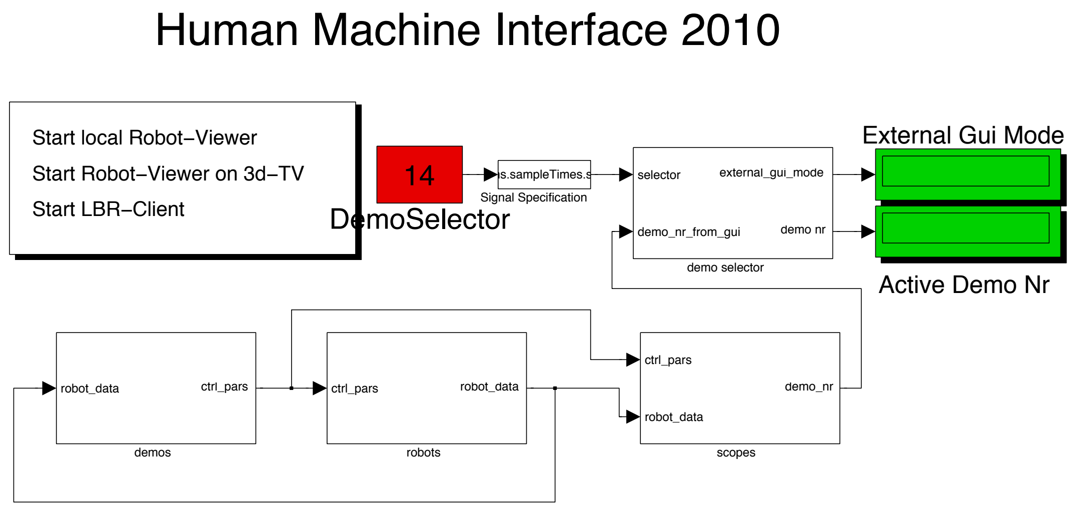

Figure 3.6: HMI2010 Simulink Model

piling the HMI2010 model and executing it on a computer running a real-time VxWorks operating system which supervises the control of the robots.

Within this context, a new demo was developed by De Stefano, M. [10] in order to simulate the capture phase of the DEOS mission using the human-scale bimanual haptic interface. In his study, he considered the free-flying behavior of the system and on this hypothesis developed a proportional-derivative (PD) controller of the Chaser's manipulator. Even though the system performed as expected during the tests, the verification of the control algorithms in a free-floating system was necessary. Therefore, I developed the model of the free-floating robot, as it was evidenced in Subsection 3.2.3, and integrated it in the De Stefano's demo in order to emulate the motion of the space base during the pre-contact phase of the capture maneuver. However, before the actual integration with the existing model of the simulation facility, the exported SIMPACK models, seen in Subsection 3.2.2 and in Subsection 3.2.3, were integrated inside the default HMI2010 model in a stepwise manner, gradually increasing the general complexity of the new demo and each time testing the new configuration. This was particularly useful to integrate correctly exported SIMPACK models and to develop a single Simulink block that could easily be integrated inside not only the De Stefano's model but also inside any other model based on the HMI2010, in order to achieve the free-floating behavior of the system.

3.3.1 Proof of concept

The first model of the simulation system was developed creating a new demo in the default HMI2010 model using an exported S-function from SIMPACK and a few

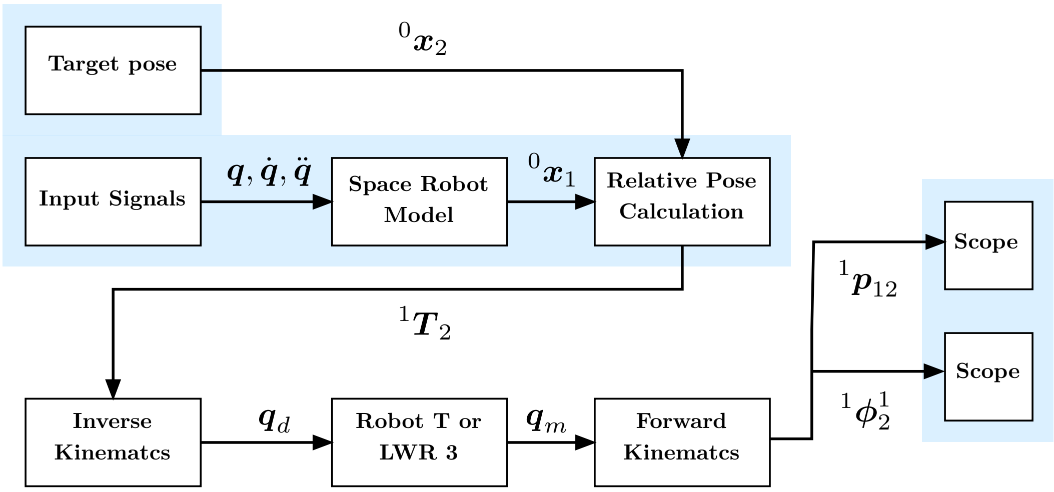

Figure 3.7: Schematic representation of the first Simulink model

custom Simulink blocks needed to calculate the relative pose of the target satellite with respect to the free-floating base. In particular, the mentioned S-function was obtained from the first model of the space robot created in SIMPACK, which detailed characteristics can be found in Subsection 3.2.2. Since the objective of the model is to emulate the dynamical behavior of the free-floating base in response to the motion of the manipulator the exported S-function requires an input signal $\boldsymbol{U}(t) = [\boldsymbol{q}(t)^T, \dot{\boldsymbol{q}}(t)^T, \ddot{\boldsymbol{q}}(t)^T]^T \in \mathbb{R}^{21\times1}$ made of the manipulator's vector of joint variables, its first and its second time derivatives. The output signal $\boldsymbol{Y}(t) = \left[\boldsymbol{p}_b^T, \boldsymbol{\phi}_b^T\right]^T \in \mathbb{R}^{6\times1}$ is the pose of the base with respect to the laboratory reference frame and is obtained directly from the virtual sensors of the model. Note that the orientation of the base with respect to the laboratory reference frame and is described with the Euler angles 321.

The schematic representation of the new HMI2010 demo is depicted in Figure 3.7. The evidenced areas indicate the developed blocks and the unknown symbols used inside the figure are defined as:

$^0\boldsymbol{x}_1 \in \mathbb{R}^{6\times1}$ absolute pose of the base;

$^0\boldsymbol{x}_2 \in \mathbb{R}^{6\times1}$ absolute pose of the target;

$\boldsymbol{q}_d \in \mathbb{R}^{7\times1}$ desired vector of joint angles commanded to the manipulator;

$\boldsymbol{q}_m \in \mathbb{R}^{7\times1}$ measured vector of joint angles of the manipulator, generally slightly different from $\boldsymbol{q}_d$;

$^1\boldsymbol{\phi}_2^1 \in \mathbb{R}^{3\times1}$ orientation vector of Σ_1 relative to Σ_2, expressed in Σ_1;

Furthermore, referring to Figure 3.7 note that:

1. the Simulink model does not include Robot C which at first might appear contradictory given the purpose of the whole simulation. Nevertheless, this was done on purpose since one of the requirements of this model was the ability to control at will the input vector $\boldsymbol{U}(t) = [\boldsymbol{q}(t)^T, \dot{\boldsymbol{q}}(t)^T, \ddot{\boldsymbol{q}}(t)^T]^T \in \mathbb{R}^{21\times 1}$ needed by the model of the space robot;

2. the Target is assumed to be fixed in the laboratory reference frame and to have the absolute position and orientation equal to

$$^0\boldsymbol{p}_2 = [-0.4\,\mathrm{m}, 0.1\,\mathrm{m}, 0.6\,\mathrm{m}]^T$$

$$^0\boldsymbol{\phi}_2^0 = [0.1745\,\mathrm{rad}, 0.1745\,\mathrm{rad}, 0.1745\,\mathrm{rad}]$$

   chosen according to the workspace of the LWR used to simulate its motion;

3. the initial pose of the base centroid with respect to the laboratory reference frame is zero or in other words the Σ_1 and Σ_0 are initially coincident.

4. the scope blocks indicate the measured quantities that were used to validate the implementation of the developed simulation concept .

In order to test the aforementioned demo, a SIMPACK model of the simulated system was developed and used as template for the comparison of the results. Obviously the same inputs of the Simulink model were used for the numeric simulation in SIMPACK. The visualization of the system's model in SIMPACK is illustrated in figure *a* of Figure 3.8. The red cube represents the target spacecraft whose close position to the free-floating base was chosen according to the workspace of the LWR, as pointed out previously. However, during the numeric simulations the intersection of the two bodies did not influence the results since contact forces weren't considered. On the other hand, figure *b* of Figure 3.8 depicts the visualization of the virtual HIL setup and in particular the target robot since the motion of the chaser robot isn't taken in to account in this demo.

Two numeric simulations were performed using the SIMPACK and Simulink platforms in order to achieve the necessary data for the comparison. The first simulation was performed considering the vector of joint variables equal to

$$\boldsymbol{q}\,(t) = [A\sin(\omega t + \phi)\,, A\sin(\omega t + \phi)\,, 0, 0, 0, 0, 0]^T$$

where $A = 1\,\mathrm{rad}, \omega = 0.5\,{}^{\mathrm{rad}}/_{\mathrm{s}}, \phi = 1.5708\,\mathrm{rad}$ in order to obtain $\dot{\boldsymbol{q}}(0) = \ddot{\boldsymbol{q}}(0) = \mathbf{0}$. While the second simulation study was done considering $\boldsymbol{q}(t) = [q_i]$ with $q_i = A\sin(\omega t + \phi)$ and $i = 1, \ldots, 7$. The amplitude, the frequency and the phase of

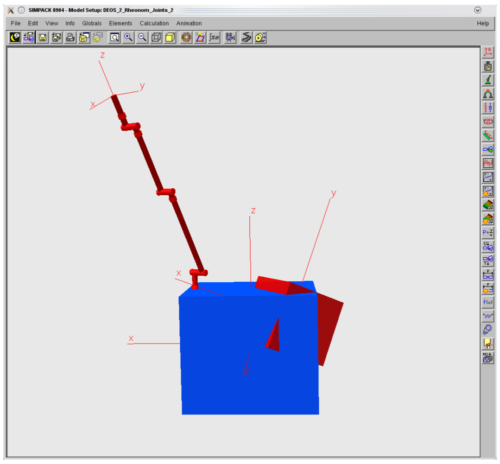

(a) SIMPACK model of the whole system

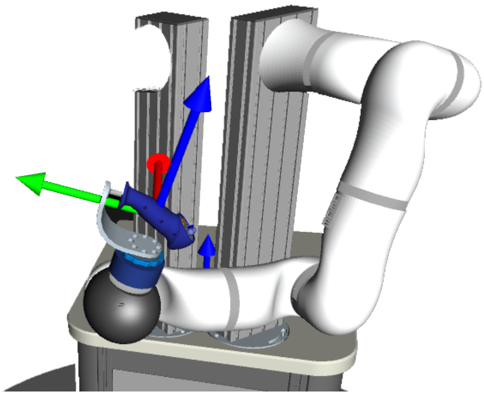

(b) Virtual HIL setup

Figure 3.8: Visualization of simulation environments

the oscillation of the vector of joint variables are identical to the values indicated in the first simulation.

The requested data, represented by the relative pose of the target spacecraft, was than saved and used for comparison between the two platforms. Figure 3.9 depicts the results of this comparison indicating the almost identical data obtainable from the two platform and thus confirming that the implementation of the simulation concept in Simulink was done correctly. The small divergence between results is due to different types of integrators used by the two platforms and to the inertia properties of the robotic arm used to simulate the motion of the target spacecraft completely absent in SIMPACK.

Following the successful design of the first model, the second was developed in the same manner (see Figure 3.7). However, this time the imported S-functions have the characteristics of the manipulator identical to the LWR III (see Subsection 3.2.3) instead to the DEOS manipulator as previously. Moreover, the S-functions were exported from the first group of SIMPACK models, considered to have all the same size of the carrier spacecraft but different masses. As for the first demo, SIMPACK models of the simulated free-floating system were developed and used as templates for the comparison of the simulation results. The only difference from the previous demo is the initial absolute position of the target satellite equal to

$$^{0}\boldsymbol{p}_2 = [-0.4\,\mathrm{m}, 0.1\,\mathrm{m}, 0.4\,\mathrm{m}]^T$$

The reason of this change are to be found in the dimensions of the LWR's workspace since wide movements of its end-effector were expected due to lighter

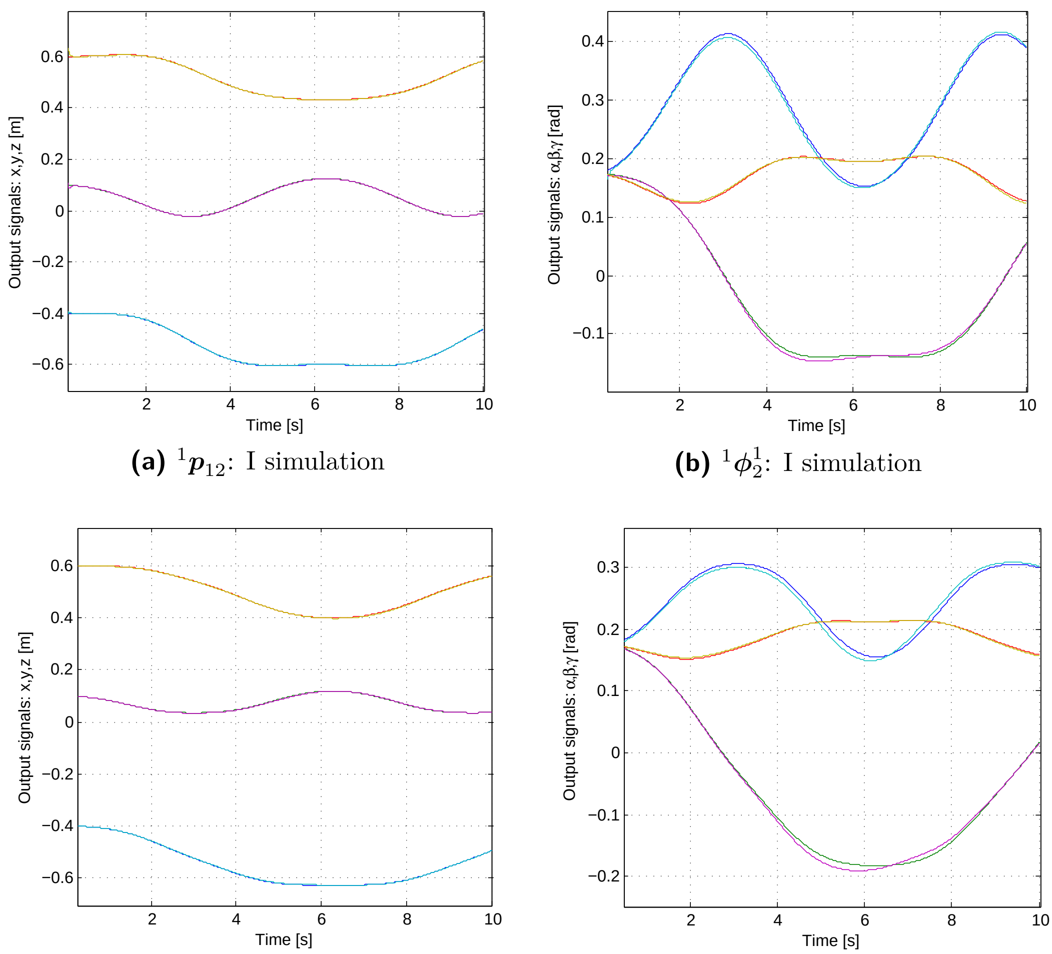

(a) ${}^{1}\boldsymbol{p}_{12}$: I simulation

(b) ${}^{1}\boldsymbol{\phi}_{2}^{1}$: I simulation

(c) ${}^{1}\boldsymbol{p}_{12}$: II simulation

(d) ${}^{1}\boldsymbol{\phi}_{2}^{1}$: II simulation

Figure 3.9: Comparison between SIMPACK and Simulink results: I part

bases. The absolute orientation of the base is instead considered the same.

The numeric simulations were performed in two stages as previously. At first, only the sinusoidal motion of the joints one and two of the manipulator was considered obtaining modest motion of the base. Than the sinusoidal motion of all joints was taken in to account and the simulation time was extended from 10 s to 60 s. The comparison of the results of the latter simulation form both platforms, considering the mass of spacecrafts, m_b, equal to 724.10 kg, 45.256 kg and 2.829 kg, are visible in Figure 3.10. The outcome of the comparison was satisfying, at least during the first 20 s, confirming the validity of the demo and allowing to proceed with the refinement of the existing model of the HIL concept. Nevertheless, it is important to notice that the amplitude of the difference between the results of SIMPACK and Simulink models tends to increase with time proving that the main cause of it are different types of integrators used by the two simulation platforms.

3.3.2 Model of the experimental system

Using the existing model of the multimodal human machine interface, developed by De Stefano, M. for the simulation of the capture phase of the DEOS mission, the realization of the second mode of the kinematic equivalence, illustrated in Figure 2.20 on page 60, was possible considering two control schemes shown in Figure 3.11 and Figure 3.12, respectively. In both schemes the evidenced areas indicate the new Simulink blocks introduced in order to achieve the desired simulation behavior while the unknown symbols are defined as

$\boldsymbol{F}_c \in \mathbb{R}^{6\times1}$ generalized control force applied to the end-effector;

$\boldsymbol{J} \in \mathbb{R}^{6\times7}$ the Jacobian matrix of the manipulator;

$\boldsymbol{\tau}_c \in \mathbb{R}^{7\times1}$ generalized control torque or control joint torques of the manipulator. Note that this variable does not include the gravity compensation torque which is added to the control torque subsequently inside the robot block;

$\boldsymbol{\tau}_c^{'} \in \mathbb{R}^{7\times1}$ control torque generated by the admittance controller. Also this vector does not include the gravity compensation torque, as it was evidenced above;

$\boldsymbol{F}_e \in \mathbb{R}^{3\times1}$ external forces applied on the centroid of the target satellite;

$\boldsymbol{M}_e \in \mathbb{R}^{3\times1}$ external moments applied on the centroid of the target satellite;

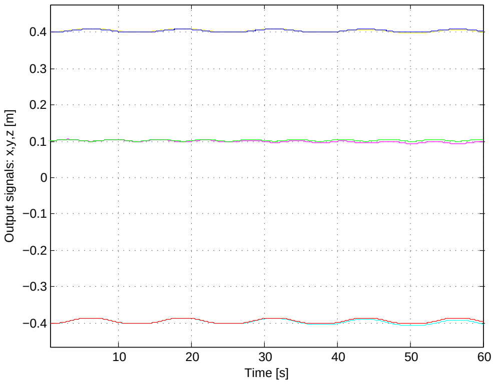

(a) ${}^{1}\boldsymbol{p}_{12}$: $m_b = 724.10\,\mathrm{kg}$

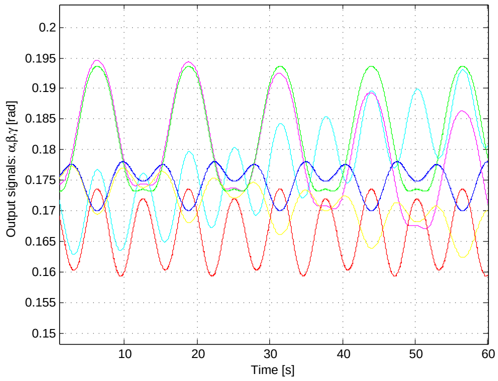

(b) ${}^{1}\boldsymbol{\phi}_{2}^{1}$: $m_b = 724.10\,\mathrm{kg}$

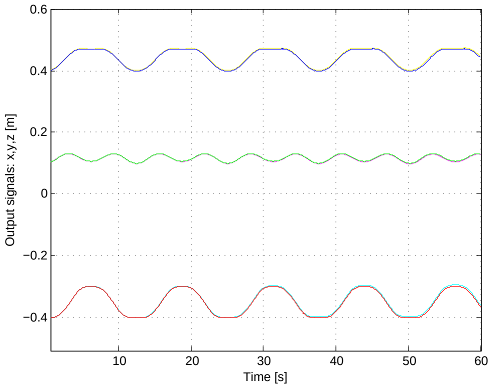

(c) ${}^{1}\boldsymbol{p}_{12}$: $m_b = 45.256\,\mathrm{kg}$

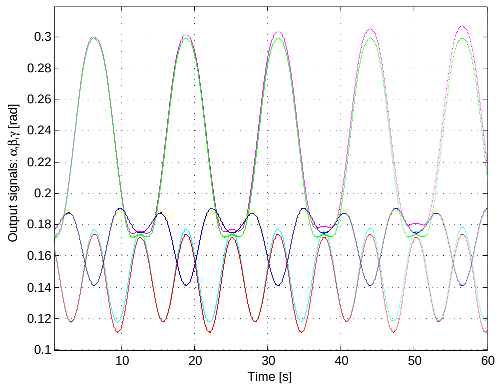

(d) ${}^{1}\boldsymbol{\phi}_{2}^{1}$: $m_b = 45.256\,\mathrm{kg}$

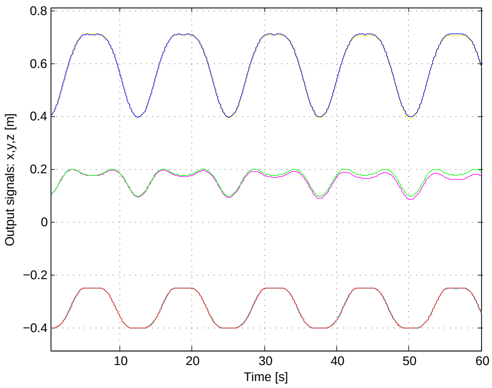

(e) ${}^{1}\boldsymbol{p}_{12}$: $m_b = 2.829\,\mathrm{kg}$

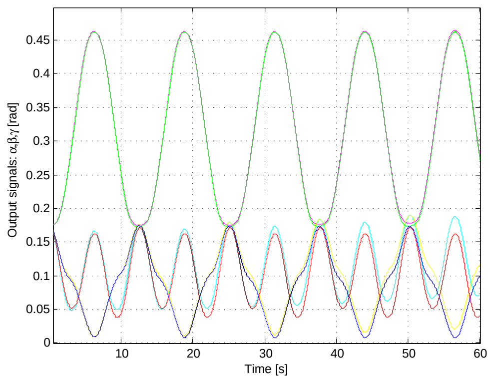

(f) ${}^{1}\boldsymbol{\phi}_{2}^{1}$: $m_b = 2.829\,\mathrm{kg}$

Figure 3.10: Comparison between SIMPACK and Simulink results: II part

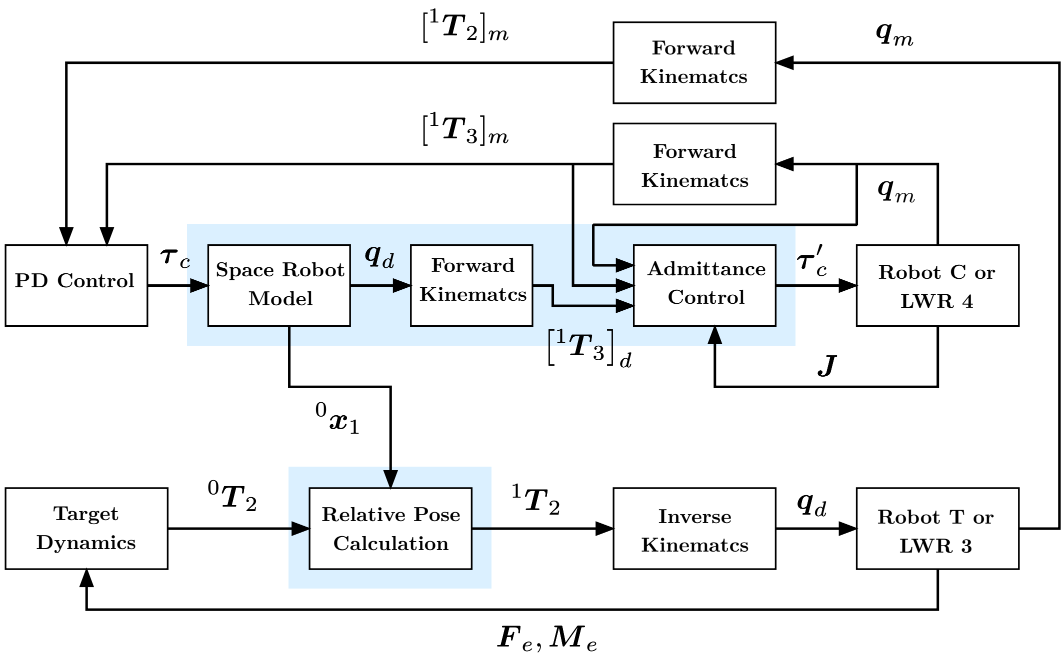

Figure 3.11: "*Torque*" control scheme

Furthermore, all symbols having the subscript m indicate the measured variables while the one with the subscript d denote the desired variables generally used as input signals for robots or controllers.

In the "*torque*" control scheme, depicted schematically in Figure 3.11, the PD controller determines the control force to be applied to the end-effector of Robot C based on the error between the pose of the end-effectors of Robot T and C. The control force, in the approach phase of the capture maneuver, is determined by the following expression [10]

$$\boldsymbol{F}_c = \begin{bmatrix} {}^3\boldsymbol{R}_1 & 0 \\ 0 & {}^3\boldsymbol{R}_1 \end{bmatrix} (\boldsymbol{F}_p + \boldsymbol{F}_d) \tag{3.6}$$

Where

$$\boldsymbol{F}_p = \begin{cases} \boldsymbol{K}_{pp}\boldsymbol{e} & \Leftrightarrow\ |\boldsymbol{F}_p| < \boldsymbol{F}_{max} \\ \text{else} & \\ \dfrac{\boldsymbol{K}_{pp}\boldsymbol{e}}{|\boldsymbol{K}_p\boldsymbol{e}|}\boldsymbol{F}_{max} & \Leftrightarrow\ |\boldsymbol{F}_p| \geq \boldsymbol{F}_{max} \end{cases} \tag{3.7}$$

while

$$\boldsymbol{F}_d = \boldsymbol{K}_d\dot{\boldsymbol{e}} \tag{3.8}$$

and in the end

$$\boldsymbol{K}_{pp} = \frac{\boldsymbol{K}_p}{(1 + \boldsymbol{\alpha}\,|\boldsymbol{e}|)^2} \tag{3.9}$$

The used symbols are defined as:

${}^{i}\boldsymbol{R}_j \in \mathbb{R}^{3\times3}$ the rotation matrix inertia matrix of the reference frame Σ_j with respect to Σ_i. In our case ${}^{3}\boldsymbol{R}_1$ indicates the orientation of the free-floating base (assumed fixed) with respect to the end-effector;

$\boldsymbol{K}_p \in \mathbb{R}^{6\times6}$ diagonal matrix representing the proportional gain of the PD control, a tuning parameter;

$\boldsymbol{K}_d \in \mathbb{R}^{6\times6}$ diagonal matrix representing the derivative gain of the PD control, a tuning parameter;

$\boldsymbol{e} \in \mathbb{R}^{6\times1}$ is the pose error between the end-effectors of the chaser and target robots. Obviously in approach phase the desired value is zero;

$\boldsymbol{F}_{max} \in \mathbb{R}^{6\times1}$ the maximum allowable generalized control force;

$\boldsymbol{\alpha} \in \mathbb{R}^{6\times1}$ constant vector used to tune more precisely the the PD controller, a tuning parameter.

Afterwords, multiplying the transposed Jacobian of the manipulator with the aforementioned control force the generalized control torque is obtained. Note again that this control torque of the joints does not include the gravity compensation component that is added to it in the robot block. The control torque is then used as an input signal to the model of the space robot, on contrary to the signal $\boldsymbol{U}(t) = [\boldsymbol{q}(t)^T, \dot{\boldsymbol{q}}(t)^T, \ddot{\boldsymbol{q}}(t)^T]^T \in \mathbb{R}^{21\times1}$ employed in previous models.

In order to precisely emulate the motion of the free-floating base due to the input torque vector it is necessary to make sure that the initial configuration of the manipulator inside the imported model is identical to that of Robot C. This consideration could seem obvious but from personal experience I can affirm that errors of this kind are quite common. Another important issue, regarding the dynamic emulation, concerns the presence of spikes of the input signal commanded to the S-function. These spikes generally have considerable amplitude and are observable in the first milliseconds of the simulation. Their cause is to be found in the design of the demo itself. If commanded to the space robot model they could lead to wrong results as it was experimented during the initial phases of the refinement of the existing model. Thus various precisely timed switches were employed in order to block the signal in the first millisecond of the simulation. Different solutions to this problem could be found but nevertheless the one described was the most straightforward and thus the one employed.

After the dynamic emulation of the space robot, two output signals generate from the space robot model: the absolute pose of the carrier spacecraft, just as in the first iterations of the simulation concept, seen in Subsection 3.3.1, and the vector of the joint angles of the space manipulator. The latter is directly measured form the SIMPACK model and is assumed to be the desired vector since the emulated joints of the free-floating robot are ideal or in other words without frictional forces or time delays generally associated with the real hardware. The two outputs, ${}^0\boldsymbol{x}_1$ and $\boldsymbol{q}_d$, are than used, respectively, for the calculation of the relative pose of the Target with respect to the moving base and of the desired pose of the end-effector of Robot C. The admittance controller, added in order to satisfy the compliance request of the model, is than able to determine the generalized torque vector that is directly sent to Robot C to perform the desired motion or in our case the capture of the target spacecraft represented by the end-effector of Robot T. Finally, the relative pose of the Target satellite, ${}^1\boldsymbol{T}_2$, is used to obtain the joint angles of the Robot T which is than controlled accordingly to attain the desired motion. Note that the absolute motion of the target satellite, ${}^0\boldsymbol{T}_2$, is determined from the following equation of motion [10]

$$\ddot{\boldsymbol{x}}_{sat} = \begin{bmatrix} \ddot{\boldsymbol{p}}_{sat} \\ \ddot{\boldsymbol{\phi}}_{sat} \end{bmatrix} = \begin{bmatrix} \frac{\boldsymbol{F}_e}{m_{sat}} \\ \boldsymbol{I}_{sat}^{-1}\left(\boldsymbol{M}_e - \dot{\boldsymbol{\phi}} \times \boldsymbol{I}_{sat}\dot{\boldsymbol{\phi}}\right) \end{bmatrix} \tag{3.10}$$

where the symbols are:

$\boldsymbol{x}_{sat} \in \mathbb{R}^{6\times 1}$ the absolute pose of the body reference frame of the satellite;

$\boldsymbol{p}_{sat} \in \mathbb{R}^{3\times 1}$ the absolute position of the body reference frame of the satellite;

$\boldsymbol{\phi}_{sat} \in \mathbb{R}^{3\times 1}$ the absolute orientation of the body reference frame of the satellite;

$m_{sat} \in \mathbb{R}$ the mass of the satellite;

$\boldsymbol{I}_{sat} \in \mathbb{R}^{3\times 3}$ the inertia matrix of the satellite;

The external forces and moments applied to the satellite in the contact phase of the capturing maneuver are measured by the force/torque sensors of Robot T and feedback to the satellite simulator, as it can be noticed in Figure 3.11, influencing the motion of the spacecraft.

The advantage of the "*torque*" control scheme with respect to the other one is represented by the generalized control torque which is directly commanded to the emulated free-floating manipulator as it would be done in reality. Nevertheless, this was also one of the major drawbacks given that emulated space manipulator does not include the frictional forces or other imperfections of the physical joints. Thus the behavior of Robot S and Robot C wasn't identical leading to unexpected motions of the base. To overcome this problem Simulink blocks were developed based on the classical friction models used in robot literature for this purpose. The used friction models incorporated Coulomb, (linear) viscous and static friction and were modeled as a negative joint torque function of the angular joint speed opposing to the controlled torque generated by the PD controller. Despite this attempt the inability to obtain the real values of frictional forces and other major problems related to the admittance controller led inevitably to the abandonment of this scheme and to the development of the second control mode.

The "*angle*" control scheme, illustrated in Figure 3.12, is almost identical to the previous one although unlike the "*torque*" control mode the input signal of the space robot model is represented by the vector of the joint angles measured from Robot C which in turn is commanded directly by the PD controller. This way the serial connection between the controllers and the related instabilities are avoided. Furthermore, since the emulated space manipulator is controlled by the vector of joint angles, the absence of the joint friction is irrelevant. The output signals of the imported S-function are instead equivalent between the two control modes although just the relative pose of the base is visible in Figure 3.12 . This time the joint angles measured from the space robot model are only used as a verification tool between the commanded and the actual motion of the robotic arm.

The consideration regarding the initial position of the emulated manipulator, mentioned during the description of the "*torque*" control mode, is also valid together with the solution found to prevent the entry of the signal spikes in to the SIMPACK model of the free-floating base.

The LWRs used for the simulation purposes have a redundant DOF which means that it is possible to generate internal motions of the manipulator that could reconfigure its structure without changing the end-effector's position and orientation. This characteristics of the LWR can be used for two purposes: for optimizing the robot's configuration and as safety measure by featuring a compliant behavior.

In order to optimize the configuration of Robot C, during the capture phase, so that it does not reach the mechanical joint limits, a new feature was added to the PD controller of the "*angle*" control mode. To achieve this, the control torque of the PD controller was modified by adding a new term so that the final expression of the control torque could be

$$\boldsymbol{\tau}_c = \boldsymbol{J}^T \boldsymbol{F}_c + \left(\boldsymbol{I}_n - \boldsymbol{J}^\dagger \boldsymbol{J} \right) \boldsymbol{\tau}_0 \tag{3.11}$$

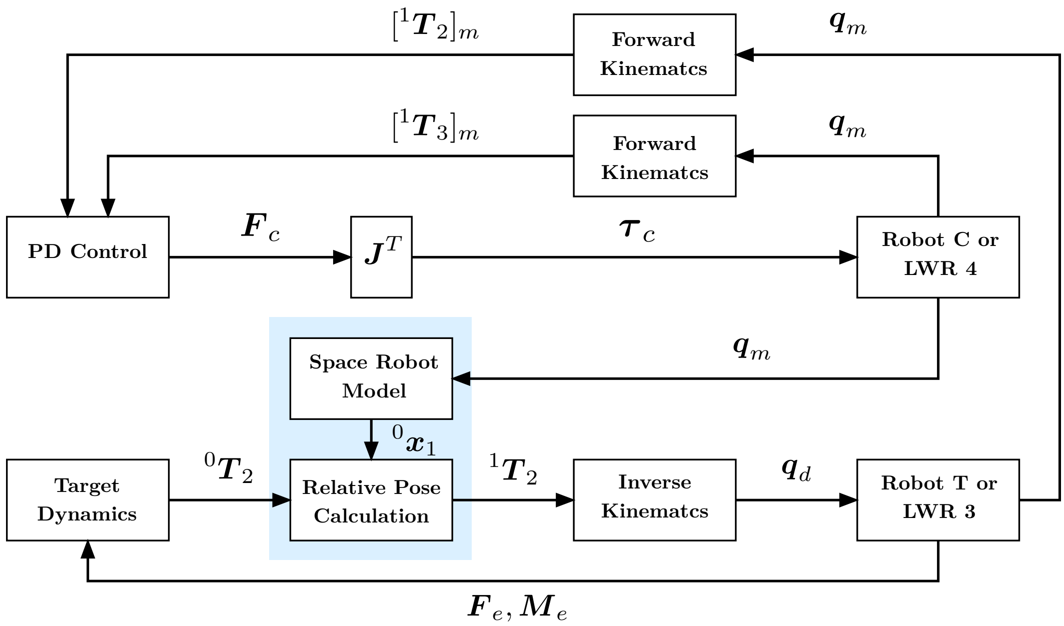

Figure 3.12: "*Angle*" control scheme

where the matrix [53]

$$\boldsymbol{J}^{\dagger} = \boldsymbol{J}^T \left(\boldsymbol{J} \boldsymbol{J}^T \right)^{-1} \tag{3.12}$$

is the *right pseudo-inverse* Jacobian of $\boldsymbol{J}$ while $\boldsymbol{I}_n \in \mathbb{R}^{n \times n}$ is the identity matrix. Note that (3.11) is composed of two terms of which the first one is the control torque that comes directly from the PD controller while the second term attempts to satisfy the additional constraint that is specified by the torque $\boldsymbol{\tau}_0$. For a convenient utilization of the redundant DOF a typical expression of the additional torque is

$$\boldsymbol{\tau}_0 = k_0 \left(\frac{\partial w(\boldsymbol{q})}{\partial \boldsymbol{q}} \right) \tag{3.13}$$

is where $k_0 > 0$ and $w(\boldsymbol{q})$ represents the secondary objective function of the joint variables. Since we want to achieve the *distance from mechanical joint limits* the objective function can be defined as [53]

$$w(\boldsymbol{q}) = -\frac{1}{2n} \sum_{i=1}^{n} \left(\frac{q_i - \bar{q}_i}{q_{iM} - q_{im}} \right)^2 \tag{3.14}$$

where q_{iM} (q_{im}). denotes the maximum (minimum) joint limit while $\bar{q}_i = \frac{q_{iM} - q_{im}}{2}$. Considering that in case of the LWR $n = 7$, the i-th component of the (3.13) becomes

$$\tau_{0_i} = k_0 \left(-\frac{1}{7} \frac{q_i - \bar{q}_i}{(q_{iM} - q_{im})^2} \right) \tag{3.15}$$

where $k_0 = \operatorname{diag}(100, 100, 100, 100, 100, 100)$. The (3.15) was than used with (3.11) to develop Simulink blocks that would implement the desired feature.

3.4 New Target Satellite Mockup

One of the fundamental elements of the HIL simulation facility is the mockup of the target satellite, necessary to achieve the physical contact and thus overcome the problem of accurately model and simulate the difficult 3D contact dynamics.

Given the relatively small dimensions of the LWR and the limited workspace of the ground simulation facility, the mockup is a scale model of the target satellite, described in Table 2.1 on page 30. Moreover, since the capture phase of the DEOS mission will be achieved by using a grappling ring or a set of grapple fixtures, visible in Figure 2.1 on page 29, placed in the front part of the satellite, the mockup recreates only this part of the spacecraft. This way a simple yet effective design is obtained while at the same time the costs of its realization are kept low. Finally, since the Target dynamics is predicted by a mathematical model, expressed in (3.10), the mass of the mockup can be kept as low as possible without influencing the spacecraft's dynamics and on the other hand easing the work of the gravity compensation function of the robot's controller.

3.4.1 The old mockup

The old mockup of the target spacecraft, used by De Stefano, M. in his study [10], is visible in Figure 3.13. It was originally developed at IRMC in 2006 for a telepresence testbed of an OOS mission. Similarly to the DEOS mission, in this past study two major tasks were: the capture of a tumbling spacecraft and its subsequent repair/maintenance by means of a teleoperated LWR II [54, 55].

The main body of the mockup is a wooden panel to which a grappling fixture, made of an aluminum alloy, and a series of connectors and other task related elements are attached. The dimensions of the wooden panel are $0.40\,\mathrm{m} \times 0.46\,\mathrm{m} \times 0.03\,\mathrm{m}$ (H×W×L) while those of the grappling fixture are $0.085\,\mathrm{m} \times 0.200\,\mathrm{m} \times 0.03\,\mathrm{m}$ (H×W×L). The latter were chosen in order to allow the grasping task also by means of teleoperated Space Justin, depicted in Figure 3.14. Space Justin is a dexterous humanoid robot capable of performing complex repair tasks in orbit featuring DLR hands as tools instead of industrial grippers. That is why the grappling fixture, visible in Figure 3.13, is sensibly wider than it would be required if the task was performed only by an industrial gripper.

The total mass of the mockup is $3.854\,\mathrm{kg}$ while the position of its cen-

(a) Frontal view **(b)** Oblique view

Figure 3.13: Old mockup of the target satellite

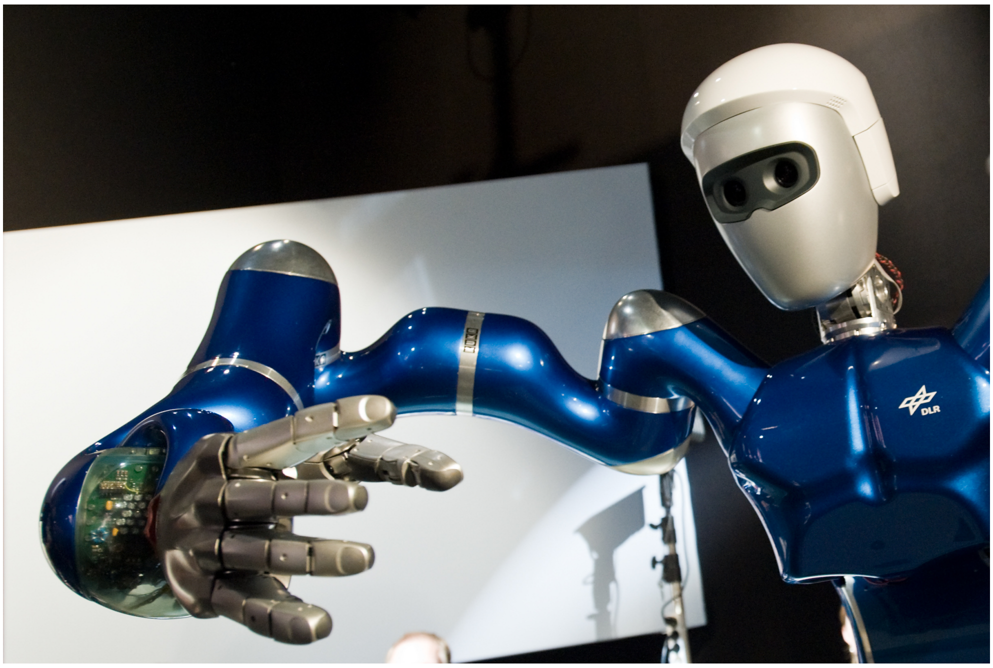

Figure 3.14: DLR's Space Justin (credit: DLR)

ter of gravity (c. g.), measured from the attach point with Robot T, is $\boldsymbol{p}_{cg} = [-0.01064\,\mathrm{m}, -0.09606\,\mathrm{m}, 0.0636\,\mathrm{m}]^T$, evidencing considerable misalignment between the c. m. of the model and the z axis of the last joint of the robot. This, together with the not irrelevant mass of the mockup, due to its not optimized design, led to the request of a new prototype, illustrated below.

3.4.2 Preliminary designs

Starting from the design of the old mockup, the new one needed to demonstrate features that are lacking in the former and that revealed important during the ground tests performed in the past. Within this context, the development of the new prototype of the target spacecraft followed the requirements enumerated hereafter:

1. the mass should be below 2 kg;
2. the dimensions should be similar to those of the old mockup. In particular, the dimensions of the grappling fixture should be identical;
3. the cost of the mockup should be low;
4. the c. g. of the model should be aligned with the z axis of the last joint of Robot T which means that the new mockup should have symmetrical design;
5. the design should reflect the front part of the target spacecraft thus the design with more than one grappling fixture should be considered;
6. the structure should be modular so that grappling fixtures with different shapes could be tested;
7. the maximum displacement of the fixtures subjected to loads of 100 N should be millimetric.

In order to fulfill the mentioned requirements and find the optimum design, in short amount of time, the 3D mechanical computer-aided design (CAD) program, SolidWorks, was used to generate different virtual prototypes visible in Figure 3.15. All of them have different characteristics and present increasingly optimized design starting from the first one depicted in figure *a*. This way, it was possible to virtually design and optimize single parts and assemblies without having to built and test them physically (see Figure 3.16), saving time and lowering the cost of the project. The technical drawings of the aforementioned models can be found in Appendix B on page 140.

At first, the design similar to the one of the existing prototype was considered with the difference that, this time, the wooden panel had no structural purpose, in fact it is only 5 mm thick. Another difference is represented by the total mass of the model that is 0.748 kg instead of 3.854 kg. Moreover, the grappling fixture is removable so that different shapes of handles can be tested during the simulation of the capture maneuver. The material used for it is an aluminum alloy 7075, often used in aerospace industry due to its high strength-to-density ratio. Nevertheless, this design was not satisfying all the stated requirements which led to its early abandonment. On the other hand, this caused the development of models illustrated in figures *b* and *c* of Figure 3.15, differing from each other for the materials used for the supporting panel, balsa wood and aluminum honeycomb composite panel, respectively. The handles are made of an an aluminum alloy 7075, as before. Particularly attractive was the model that used an aluminum sandwich-type panel which conferred high rigidity and at the same time extremely low weight to the structure. However, further refinement of this design was also interrupted since it did not comply with all the initial requirements. As before, this led to the development of a "cross" like structure with four handle, made of an aluminum alloy 7075, and a thin wooden panel. Of four handles, two are smaller and designed for the grasping with a gripper while the other two are designed for the capture with the DLR hand. Moreover, all four handles are removable and interchangeable. The wooden panel has only a decorative function. The total mass of this mockup is 1.752 kg, in compliance with the mass requirement. However, to achieve this objective, the optimization of every single part of the virtual prototype was necessary. This was possible by using the SolidWorks Simulation tool conceived to perform finite element analysis (FEA) of a model when this is subjected to desired forces and/or torques.

The results of some performed analysis are visible in Figure 3.16. They refer to the studies of the static displacement and static nodal stress of an entire virtual model and of a handle, respectively. The force applied to the elements is equal to 100 N and its direction is indicated in Figure 3.16 with red arrows. Note that the deformations visible in figures are exaggerated on purpose. The deformation scale is placed in the upper left angle of every figure.

Using those results it was possible to achieve the optimum shape of all parts of the virtual model by removing (adding) material of the element where it wasn't (was) needed or eventually changing the shape of the piece where the displacements revealed to be to high.

However, the high optimization of the assembly was also the major drawback of this model since its realization would require custom built elements, leading to

(a) Wooden model with a single handle

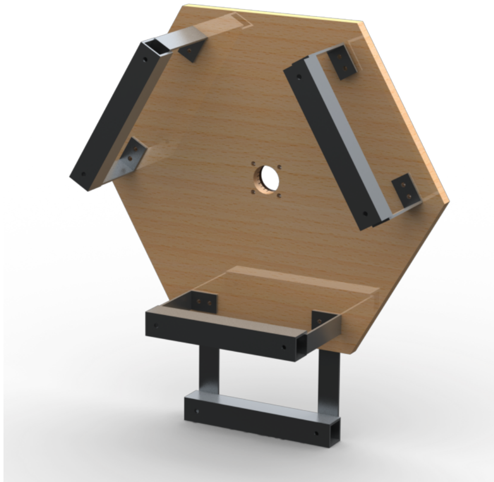

(b) Wooden model with 4 handles

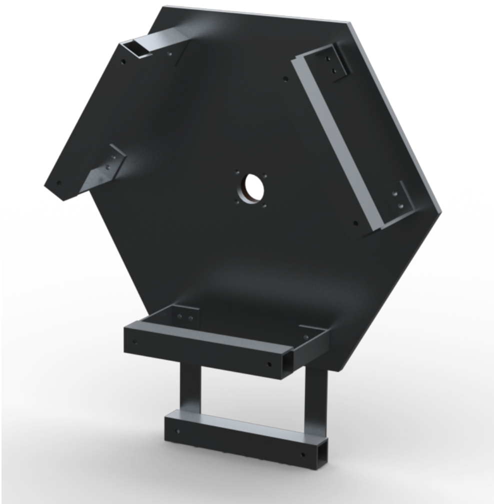

(c) Honeycomb model with 4 handles

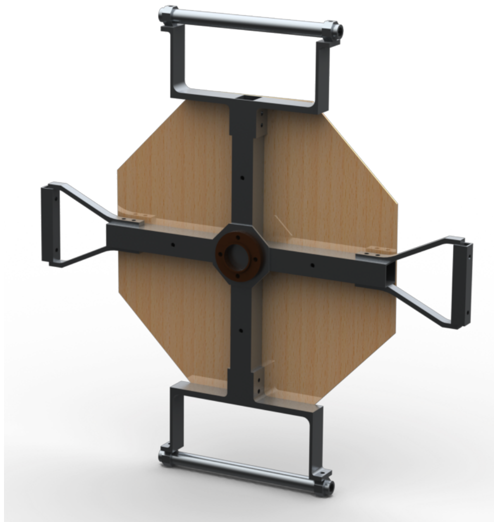

(d) Aluminum alloy 7075 model with 4 handles

Figure 3.15: Preliminary CAD models of the new mockup

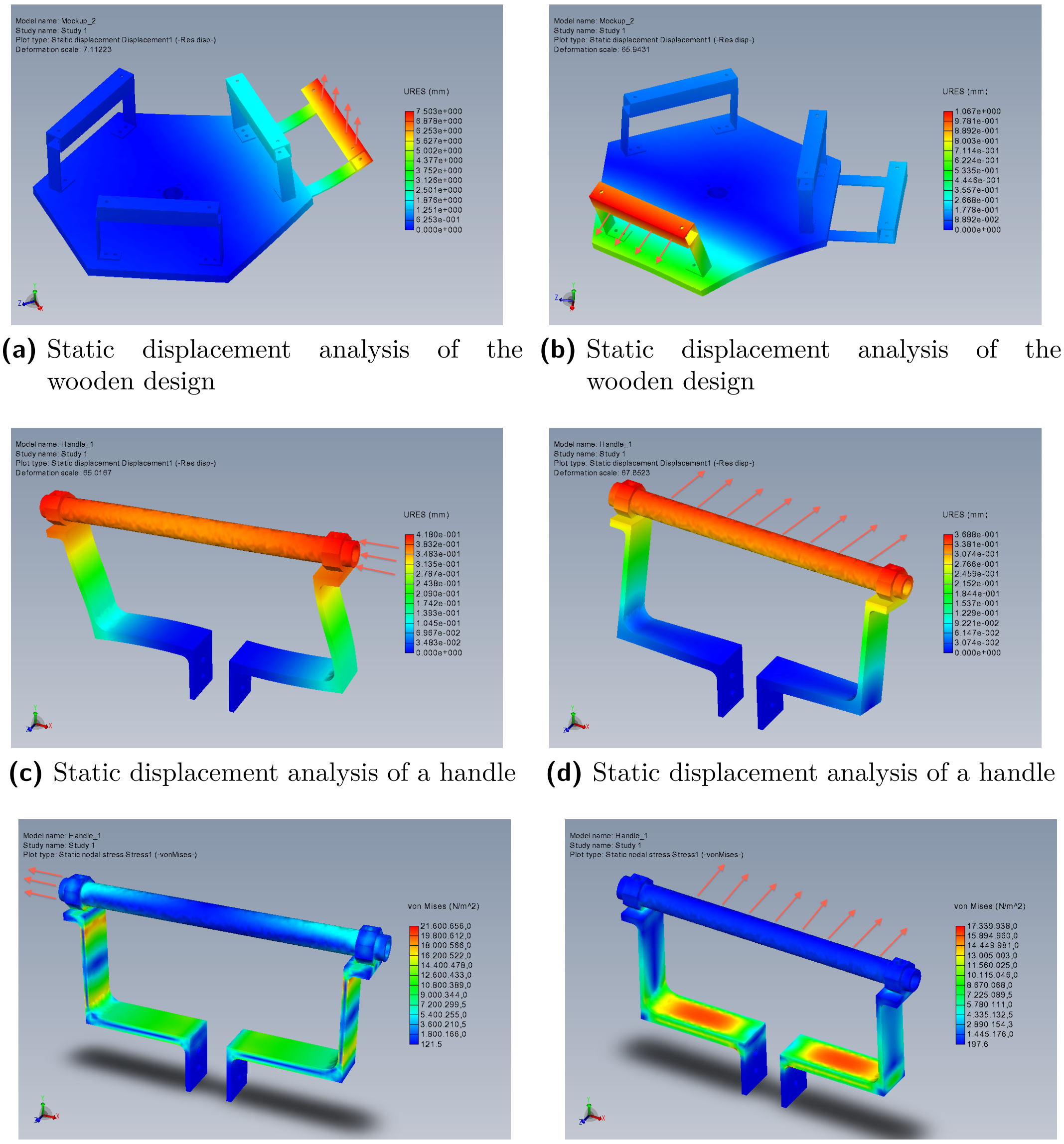

(a) Static displacement analysis of the wooden design

(b) Static displacement analysis of the wooden design

(c) Static displacement analysis of a handle

(d) Static displacement analysis of a handle

(e) Static nodal stress analysis of a handle

(f) Static nodal stress analysis of a handle

Figure 3.16: FEA of the wooden design and grappling fixtures

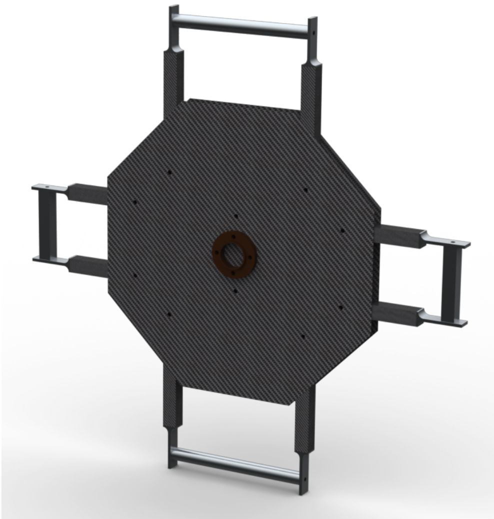

(a) Oblique view

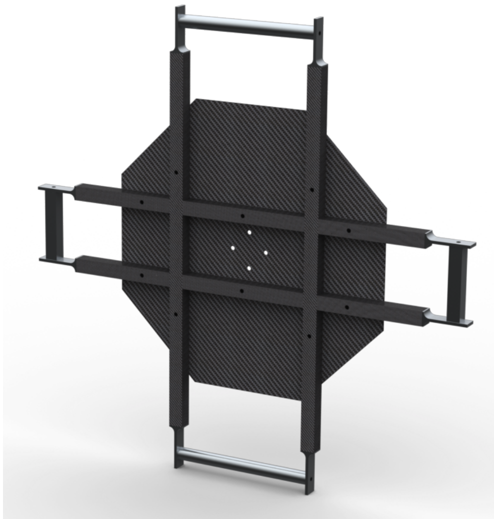

(b) Oblique view of the interior

Figure 3.17: Final CAD model of the new mockup

lengthly and, most importantly, costly fabrication.

With this in mind the use of aluminum alloy 7075, as main structural material of the future mockup, was abandoned in favor of lighter and more resistant carbon fiber reinforced polymer (CFRP). The new design, illustrated in Figure 3.17, uses almost exclusively prefabricated elements solving the problem stressed earlier.

3.4.3 Final design

The final design of the satellite mockup is almost entirely made of CFRP (see Figure 3.17), which is a very strong and light fiber-reinforced polymer containing carbon fibers. Only the handles are made of an aluminum alloy 7075 and they are custom designed to satisfy the original requirements.

Internally, the mockup has a "cross" like structure (see Figure 3.17), inherited from the previous design, made of prefabricated square carbon fiber tubes (thick only 1.30 mm) glued between them. The whole structure is than glued to the two carbon fiber plates (thick only 1 mm), conferring greater resistance to the model to non planar forces that could arise during simulations. The technical drawing of the final model can be found in Appendix B on page 140. Note that in the original design the "cross" like structure had to be screwed to the two plates instead of being glued. The latter choice was made during the fabrication process in order to minimize as much as possible the mass of the prototype by avoiding unnecessary metallic bolts.

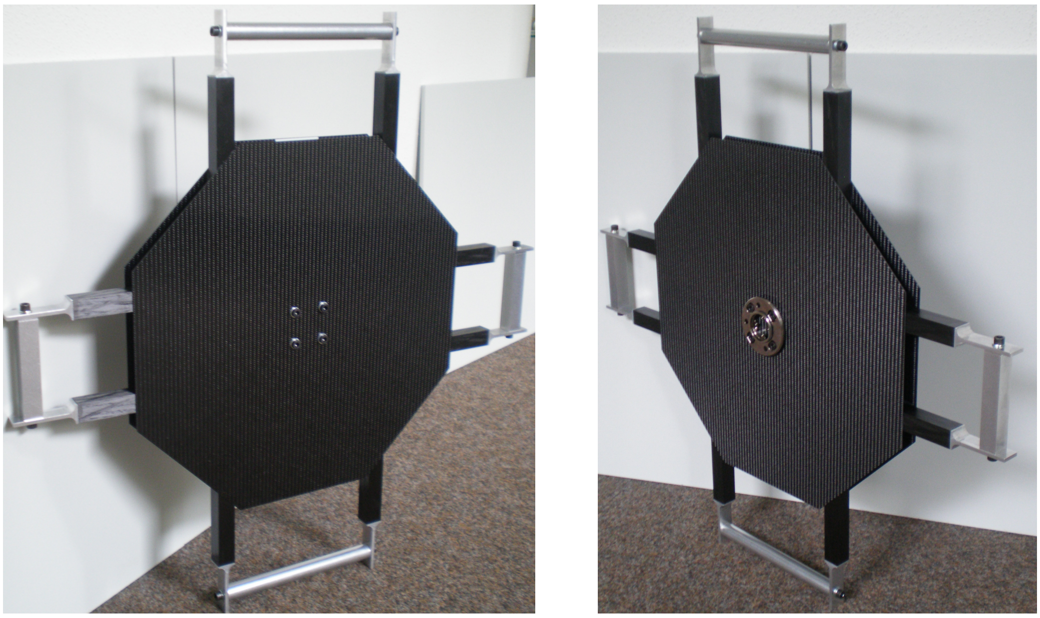

(a) Oblique view of the front

(b) Oblique view of the back

Figure 3.18: Prototype of the new mockup

The handles are four and, just like in the last model, two of them are smaller and designed for the grasping with a gripper while the other two are designed for the capture with the DLR hand. Given that CFRP was used, the handles had to be glued to the supporting structure and even though they aren't interchangeable it is possible to test different types of handles by simply substituting the horizontal part of the grappling fixture.

With this design it was possible to considerably lower the mass of the satellite mockup, visible in Figure 3.18 while satisfying all the requirements enumerated at the beginning of Subsection 3.4.2, costs included. Indeed, the mass of the prototype is only 1.3974 kg while the position of its c. g. , measured from the attach point with Robot T, is $\boldsymbol{p}_{cg} = [0\,\mathrm{m}, 0\,\mathrm{m}, 0.01174\,\mathrm{m}]^T$ as requested.

4 Numeric Simulations

Numeric simulations are a valuable tool for testing the potential of any system before their actual physical use. This is particularly true in case of new and untested systems or approaches such as the developed ground experiment system.

This chapter addresses the problem of numeric simulations performed to test the ability of the "*angle*" control scheme to emulate the free-floating behavior of the space manipulator and evidence its limits.

In the following, Section 4.1 outlines the performed simulations and indicates the starting point of the tuning process of the control parameters. Section 4.2 illustrates the first set of simulations characterized by the motion of the manipulator towards the center of gravity of the chaser spacecraft. Section 4.3, on the other hand, considers the simulations where the trajectory of the manipulator is directed away from the Chaser's center of gravity. In the end, in Section 4.4, the dynamic coupling between the manipulator and its base is accentuated by combining the second set of SIMPACK models and the motion of the Chaser's manipulator away from from its center of gravity.

4.1 General Considerations

The purpose of the numeric simulations, presented hereafter, was to throughly test the developed "*angle*" control scheme, illustrated in Figure 3.12 on page 83, and therefore attempt to find the optimum tuning of the embedded PD controller, prior to any use of the physical setup. Since the developed control scheme is based on the one created and tuned by De Stefano M. [10], the tweaking process of the PD controller started from his default values.
A generic numeric simulation illustrated in the following sections can be divided in to the following phases:

1. the initialization phase;

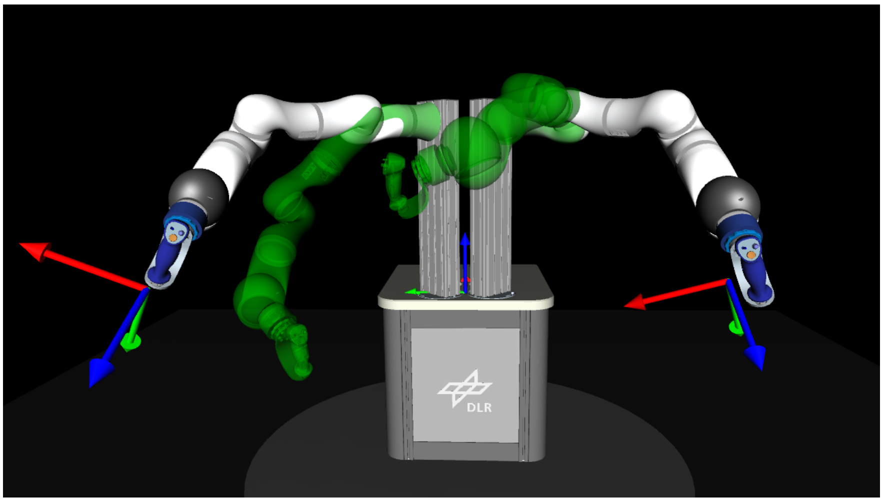

Figure 4.1: Initialization phase

2. the approach phase.

The initialization phase consists in commanding the desired initial configuration to Robot C and Robot T in order to position them appropriately for the next phase. Figure 4.1 is an illustration of this stage. The green transparent manipulators depict the desired configuration commanded to the robots during this phase.

The approach phase consists in the actual simulation of the pre-contact phase of the capture maneuver and is activated only after the two robots have reached their initial configuration defined in the previous stage. During this phase the motion of the Chaser's manipulator and thus of Robot C is determined by the PD controller, in accordance with (3.6) on page 79. The motion of Robot T, on the other hand, is determined by (3.10) on page 81 and by the output signal of a model of the free-floating manipulator.

The chaser spacecraft is assumed to have the LWR mounted on its base satellite whose inertial parameters are those of the SIMPACK models described in Subsection 3.2.3 on page 70. Given that the aforementioned models are classified in two distinct groups, two different types of simulations were considered, and are described in detail hereafter.

The mass and the inertia matrix of the target spacecraft are presumed to be the same in all simulations and equal to

$$m_{sat} = 300\,[\mathrm{kg}] \quad \text{and} \quad \boldsymbol{I}_{sat} = \mathrm{diag}\,(18, 20, 22)\ [\mathrm{kg}\cdot\mathrm{m}^2] \tag{4.1}$$

while its motion, prior to contact, is assumed to be a simple constant rotation around the z axis of its body reference frame (coincident with the z axis of the last joint of Robot T), at an angular velocity of 0.0698 $^{\mathrm{rad}}/_{\mathrm{s}}$.

In the simulation environment no tools are considered to be attached to the end-effectors of the LWRs. With this in mind, the joystick handles depicted in Figure 4.1 and in all other figures are considered to be massless.

The default configuration of the developed control scheme and thus of the PD controller is the one developed by De Stefano M. for his study of the capturing maneuver of the DEOS mission [10]. However, it must be acknowledged that the initial configuration of the LWRs and the tuning of the controller, embedded within the demo developed by De Stefano, were optimized for the real setup and not for the simulation environment that is considered here. Thus, it should not be a surprise that the results of the numeric simulations obtained with the default parameters were not satisfactory even if the free-floating base motion was not considered. Indeed, all the simulations performed using the default values led to considerable pose errors, $\boldsymbol{e}$, evidencing the necessity to retune the controller and to find a different initial configuration of the robots in order to optimize the workspace of the ground setup for the study of the free-floating base.

The mentioned default configuration is considered to have the following parameters:

$$\boldsymbol{q}_c = [1.080, -1.089, -1.076, -1.227, 0.450, 0.393, 1.280]^T \,[\mathrm{rad}] \tag{4.2}$$

$$\boldsymbol{q}_t = [-0.281, -1.360, 1.384, 0.492, -0.909, -1.615, 0.273]^T \,[\mathrm{rad}] \tag{4.3}$$

$$\boldsymbol{F}_{max} = [12, 12, 12, 5, 5, 5]^T \,[\mathrm{N}] \tag{4.4}$$

$$\boldsymbol{\alpha} = [5, 5, 5, 1, 1, 1]^T \tag{4.5}$$

$$\boldsymbol{K}_p = \mathrm{diag}\,(350, 350, 350, 100, 100, 100) \tag{4.6}$$

$$\boldsymbol{K}_d = \mathrm{diag}\,(50, 50, 50, 10, 10, 10) \tag{4.7}$$

where $\boldsymbol{q}_c \in \mathbb{R}^{7\times1}$ and $\boldsymbol{q}_t \in \mathbb{R}^{7\times1}$ are the initial vectors of joint angles of Robot C and T commanded during the initialization phase. Figure 4.2 depicts the initial configuration assumed by the two robots indicated in (4.2) and in (4.3).

The numeric simulations illustrated hereafter can be divided in to three major classes based on:

- the motion of the space manipulator during the approach phase;
- the models used for the dynamical emulation of the free-floating base.

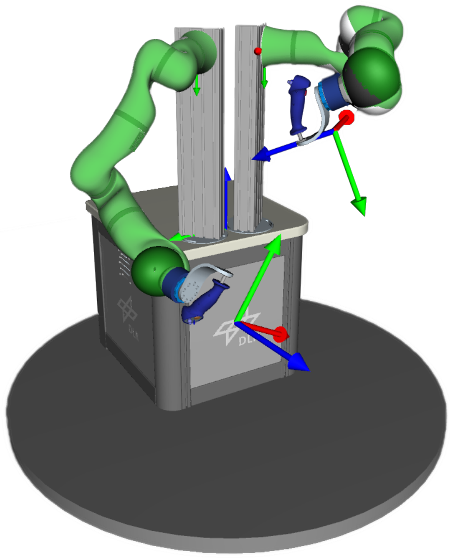

Figure 4.2: Default initial configuration

4.2 Motion Towards the Center of Mass

The numeric simulations described in this section are all characterized by the motion of the manipulator towards the c.m. of the base during the approach phase. Furthermore, the dynamic emulation of the space robot is performed considering the first set of the models, illustrated in Subsection 3.2.3 on page 70. In particular, the models with the mass of 724.10 kg, and 2.829 kg are used.

4.2.1 Initial conditions

The initial conditions of the simulation are described through the following parameters:

$$\boldsymbol{q}_c = [-1.571, 0.785, 1.571, -0.611, -0.785, 0.785, 0]^T \text{ [rad]} \tag{4.8}$$

$$\boldsymbol{q}_t = [-0.106, -1.186, 1.384, 0.492, -1.083, -1.091, -0.436]^T \text{ [rad]} \tag{4.9}$$

$$\boldsymbol{F}_{max} = [40, 40, 40, 40, 40, 40]^T \text{ [N]} \tag{4.10}$$

$$\boldsymbol{\alpha} = [15, 15, 15, 9, 9, 9]^T \tag{4.11}$$

$$\boldsymbol{K}_p = \text{diag}\,(300, 300, 850, 150, 320, 100) \tag{4.12}$$

$$\boldsymbol{K}_d = \text{diag}\,(52.5, 70, 35, 25, 25, 50) \tag{4.13}$$

Having in mind the default initial conditions, described on page 94, it can be noticed the almost overall increase of the control parameters due to the necessity

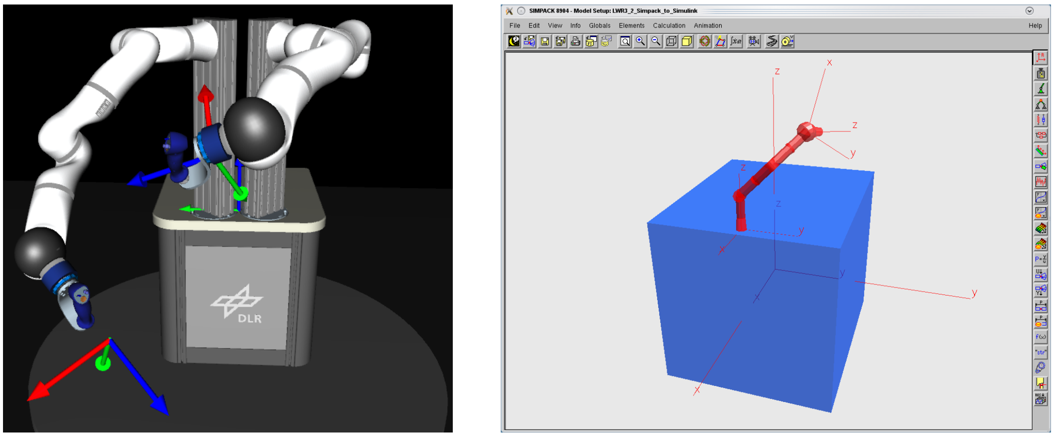

(a) In Simulink **(b)** In SIMPACK

Figure 4.3: Initial configuration of the space robot: motion towards the c. m.

to obtain faster response of the controller to contrast the dynamical coupling between the manipulator and its moving base. Moreover, the initial configuration of Robot T is essentially the default one while the initial configuration of Robot C is completely different since the default one was unsuitable for the case study. Figure 4.3 illustrates the initial configuration of the virtual ground simulation facility and the one of the model used for the dynamic emulation of the free-floating robot. Note that the manipulator in figure *b* is directed towards the base.

4.2.2 Results and conclusions

The results of the simulations of 40 s are visible in Figure 4.4, Figure 4.5 and Figure 4.6, according to the mass of the free-floating base. The exposed results concern the absolute position and orientation error between the two tool frames of Robot C and T, depicted in Figure 4.3. Moreover, the position and orientation of the body reference frame of the base with respect to the inertial coordinate system are included in the aforementioned results.

As expected, the results confirm that the motion of the base is inversely related to its mass, due to the conservation laws of linear and angular momentum. Thus, the control, without further tuning, appears to be less effective in cases where the masses of the base are similar to that of the manipulator, leading to longer settling times and thus to bigger errors between the end-effectors of Robot C and T. However, the results affirm that in this case of study the developed control parameters are appropriate, even though further tweaking appears to be necessary in cases where the mass of the base is comparable to that of the manipulator itself.

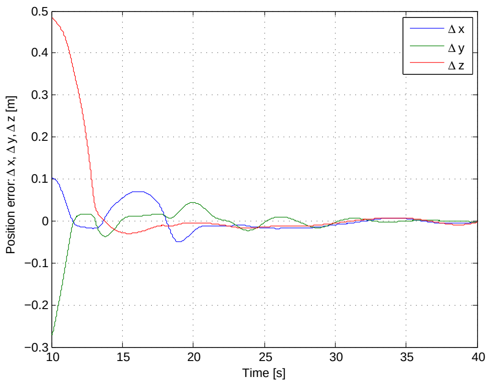

(a) Position error

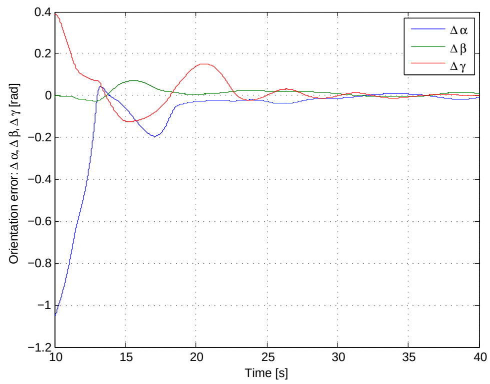

(b) Orientation error

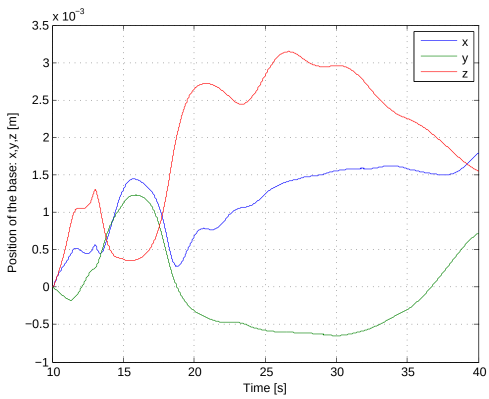

(c) Absolute position of the base

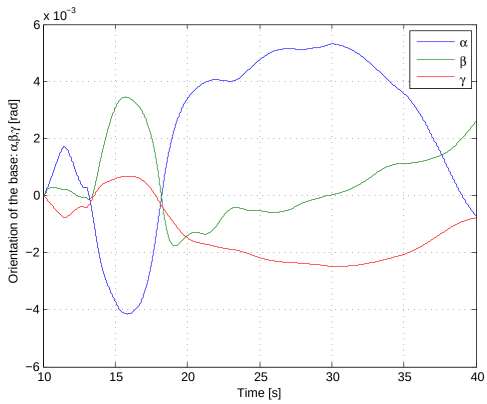

(d) Absolute orientation of the base represented by the Euler angles 321 (γ, β, α)

Figure 4.4: Simulation results: $m_b = 724.10\,\text{kg}$

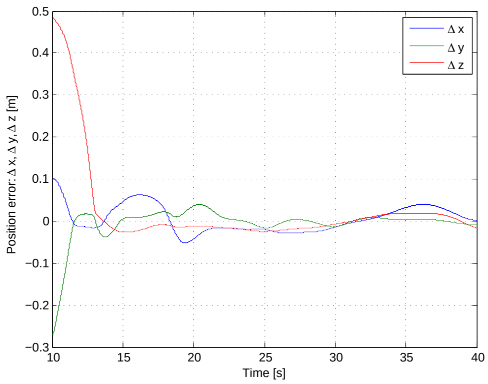

(a) Position error

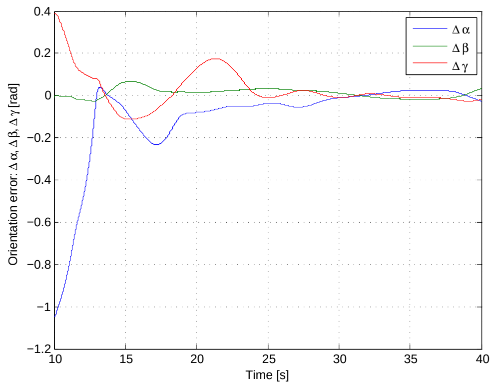

(b) Orientation error

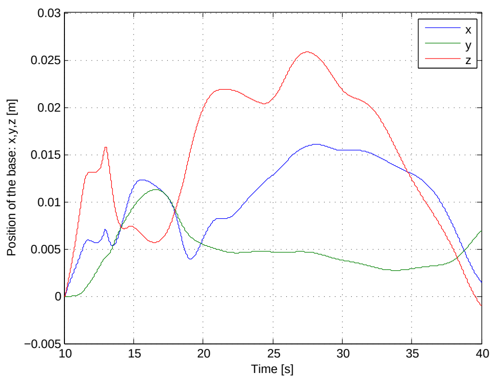

(c) Absolute position of the base

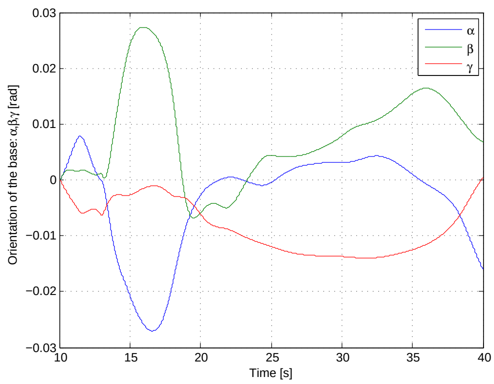

(d) Absolute orientation of the base represented by the Euler angles 321 (γ, β, α)

Figure 4.5: Simulation results: $m_b = 45.256\,\mathrm{kg}$

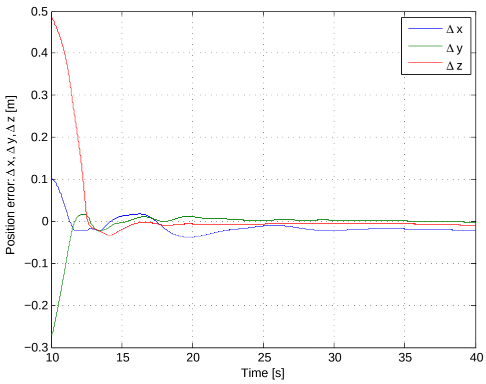

(a) Position error

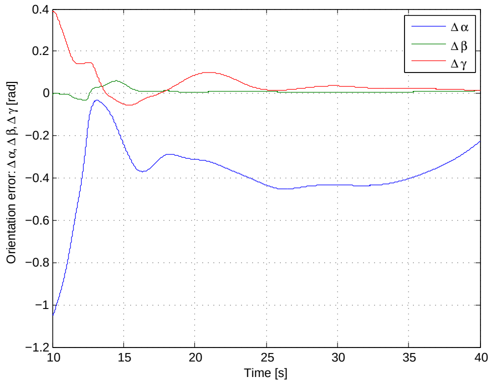

(b) Orientation error

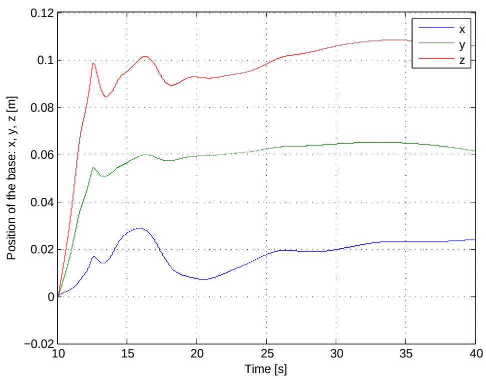

(c) Absolute position of the base

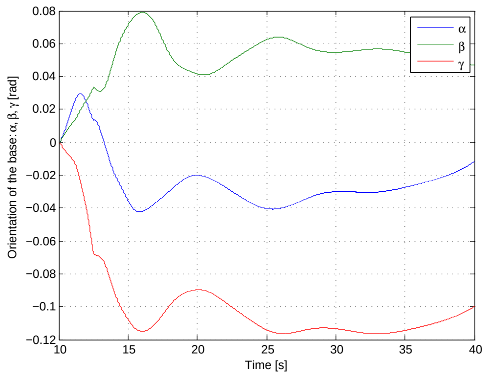

(d) Absolute orientation of the base represented by the Euler angles 321 (γ, β, α)

Figure 4.6: Simulation results: $m_b = 2.829\,\mathrm{kg}$

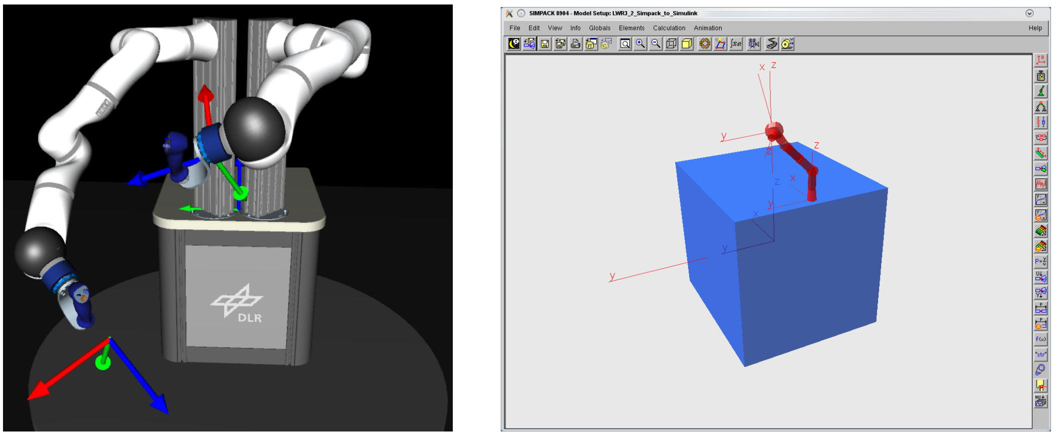

(a) In Simulink **(b)** In SIMPACK

Figure 4.7: Initial configuration of the space robot: motion away from the c. m.

4.3 Motion Away from the Center of Mass I Part

The numeric simulations illustrated in this section are characterized by the motion of the manipulator away from the Chaser's c. m. , during the approach phase, on the contrary from those seen in Section 4.2. Since this motion concerns only the emulation of the space robot's dynamics, this is achieved by displacing the manipulator's position on the carrier spacecraft inside the virtual models used in Section 4.2. Figure 4.7 illustrates the new position of the manipulator with respect to its body reference frame.

4.3.1 Initial conditions

The initial conditions of the simulations in this section are identical to those in Section 4.2 and are show below for convenience:

$$\boldsymbol{q}_c = [-1.571, 0.785, 1.571, -0.611, -0.785, 0.785, 0]^T \text{ [rad]} \tag{4.14}$$

$$\boldsymbol{q}_t = [-0.106, -1.186, 1.384, 0.492, -1.083, -1.091, -0.436]^T \text{ [rad]} \tag{4.15}$$

$$\boldsymbol{F}_{max} = [40, 40, 40, 40, 40, 40]^T \text{ [N]} \tag{4.16}$$

$$\boldsymbol{\alpha} = [15, 15, 15, 9, 9, 9]^T \tag{4.17}$$

$$\boldsymbol{K}_p = \text{diag}\,(300, 300, 850, 150, 320, 100) \tag{4.18}$$

$$\boldsymbol{K}_d = \text{diag}\,(52.5, 70, 35, 25, 25, 50) \tag{4.19}$$

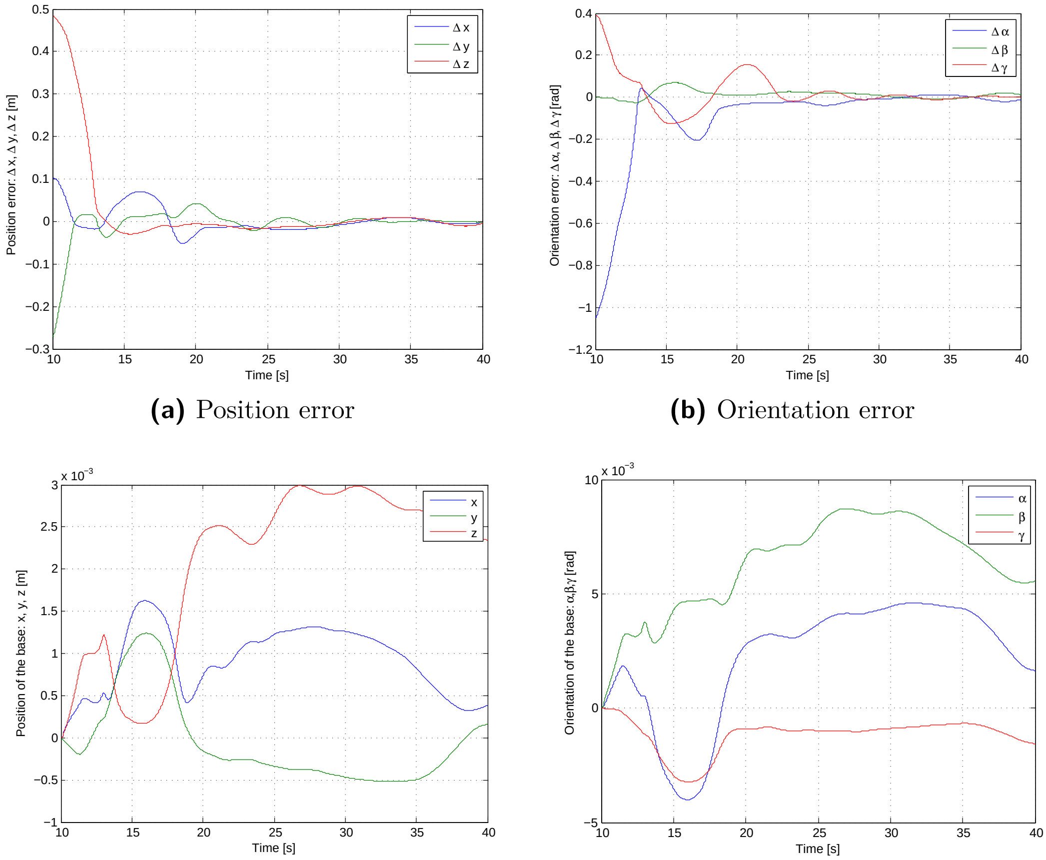

(a) Position error

(b) Orientation error

(c) Absolute position of the base

(d) Absolute orientation of the base represented by the Euler angles 321 (γ, β, α)

Figure 4.8: Simulation results: $m_b = 724.10\,\mathrm{kg}$

4.3.2 Results and conclusions

The results of the simulation studies, visible in Figure 4.8, Figure 4.9 and also in Figure 4.10, illustrate that the pose error has essentially the same pattern for $m_b = 724.10\,\mathrm{kg}$, as in Figure 4.4, while it has changed for the smaller masses, even though moderately. However, it can be noticed that the different motion of the manipulator (away from the c. m. instead of towards) has limited effect to the base motion in cases where the Chaser's mass is comparable to that of the robot since than the distance between the end-effector and the c. m. of the system is almost identical to the case analyzed in Section 4.2.

As before, it can be concluded that despite the free-floating base the controller responds rather properly and its tuning appears to be satisfactory for high masses of the carrier spacecraft while further tuning seems to be necessary in cases where the mass of the base is comparable to that of the manipulator itself.

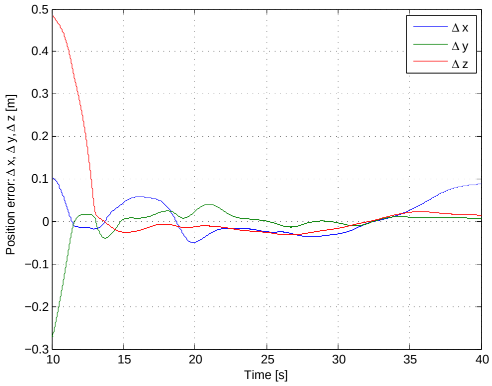

(a) Position error

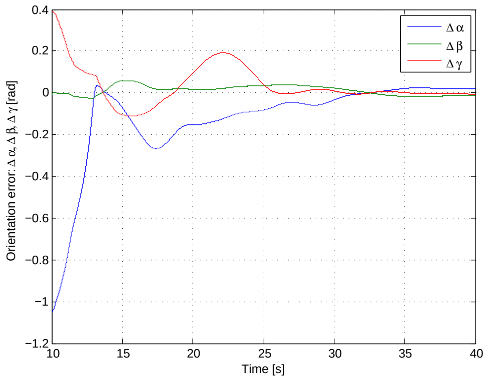

(b) Orientation error

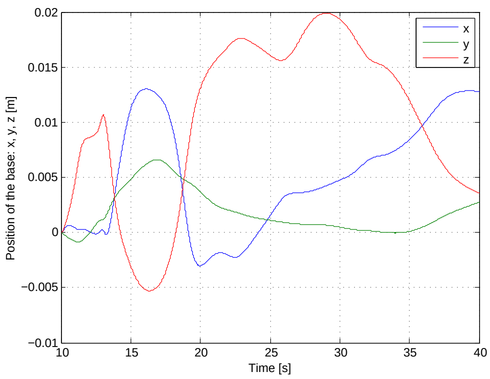

(c) Absolute position of the base

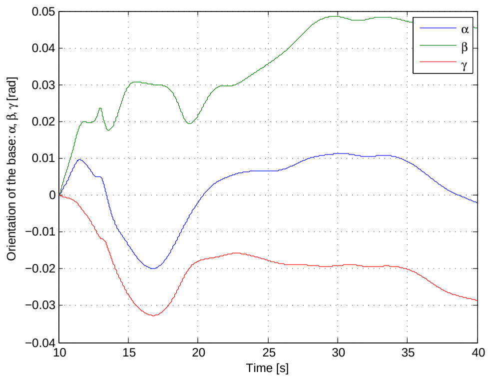

(d) Absolute orientation of the base represented by the Euler angles 321 (γ, β, α)

Figure 4.9: Simulation results: $m_b = 45.256\,\mathrm{kg}$

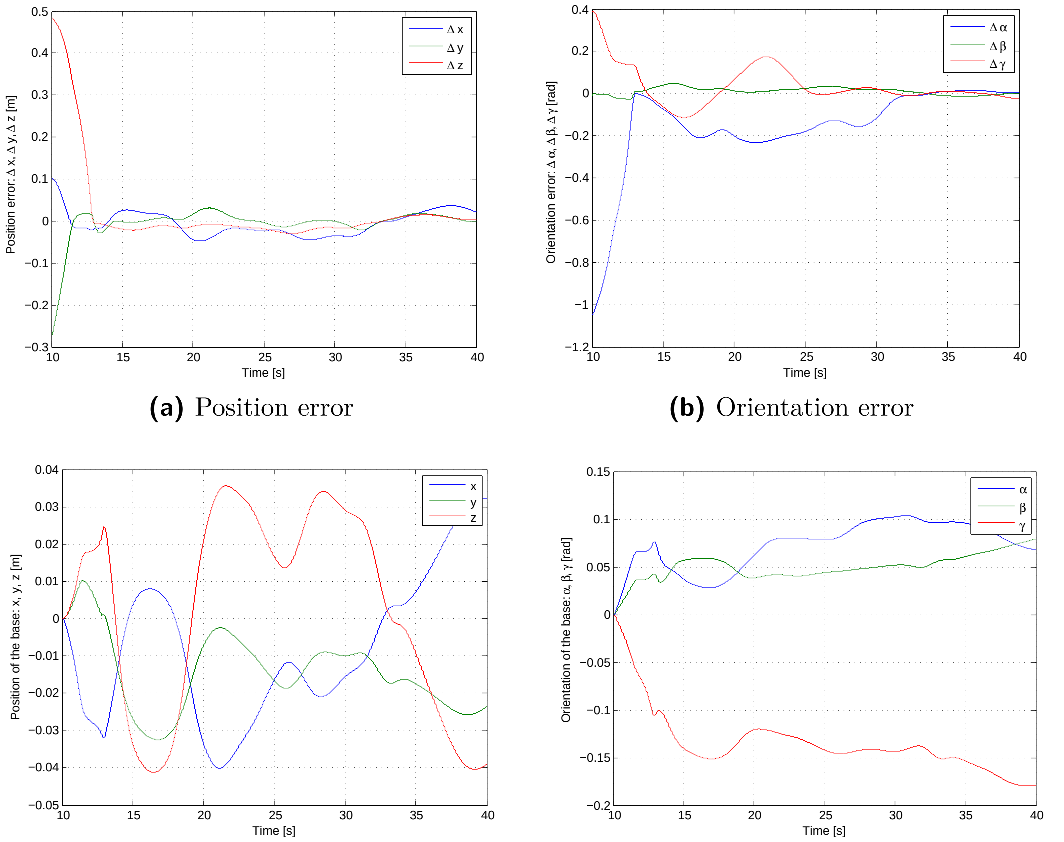

(a) Position error

(b) Orientation error

(c) Absolute position of the base

(d) Absolute orientation of the base represented by the Euler angles 321 (γ, β, α)

Figure 4.10: Simulation results: $m_b = 2.829\,\mathrm{kg}$

4.4 Motion Away from the Center of Mass: II Part

The numeric simulations of the approach phase, illustrated hereafter, exhibit the motion of the manipulator away from the c. m. of the base spacecraft, as in Section 4.3. However, unlike the previous simulation studies, the inertia properties of the emulated space robots in this section are proportional to those of the default spacecraft according to their dimensions. This is achieved by using the second group of models, presented in Subsection 3.2.3 on page 70, suitable modified to obtain the aforementioned motion of the manipulator.

Two different simulation studies were performed under this requirements. The first study uses the initial conditions seen so far in order to achieve the results that could be compared with those illustrated previously. The second study, on the other hand, uses different initial conditions in order to obtain the desired control performance even in the worst case scenarios such as those were the mass of the base is comparable to that of the manipulator.

4.4.1 Initial conditions

I simulation study

The initial conditions of the first simulation study are identical to those described in Section 4.2 and in Section 4.3 and are reported hereafter for convenience:

$$\boldsymbol{q}_c = [-1.571, 0.785, 1.571, -0.611, -0.785, 0.785, 0]^T \, [\text{rad}] \tag{4.20}$$

$$\boldsymbol{q}_t = [-0.106, -1.186, 1.384, 0.492, -1.083, -1.091, -0.436]^T \, [\text{rad}] \tag{4.21}$$

$$\boldsymbol{F}_{max} = [40, 40, 40, 40, 40, 40]^T \, [\text{N}] \tag{4.22}$$

$$\boldsymbol{\alpha} = [15, 15, 15, 9, 9, 9]^T \tag{4.23}$$

$$\boldsymbol{K}_p = \text{diag}\,(300, 300, 850, 150, 320, 100) \tag{4.24}$$

$$\boldsymbol{K}_d = \text{diag}\,(52.5, 70, 35, 25, 25, 50) \tag{4.25}$$

II simulation study

The initial conditions of the second simulations study, optimized for this particular case, present slightly different initial configuration of the robots, with respect to the previous one, while the control parameters, $\boldsymbol{K}_p$ and $\boldsymbol{K}_d$, are nearly increased by an order of magnitude to achieve the desired control behavior.

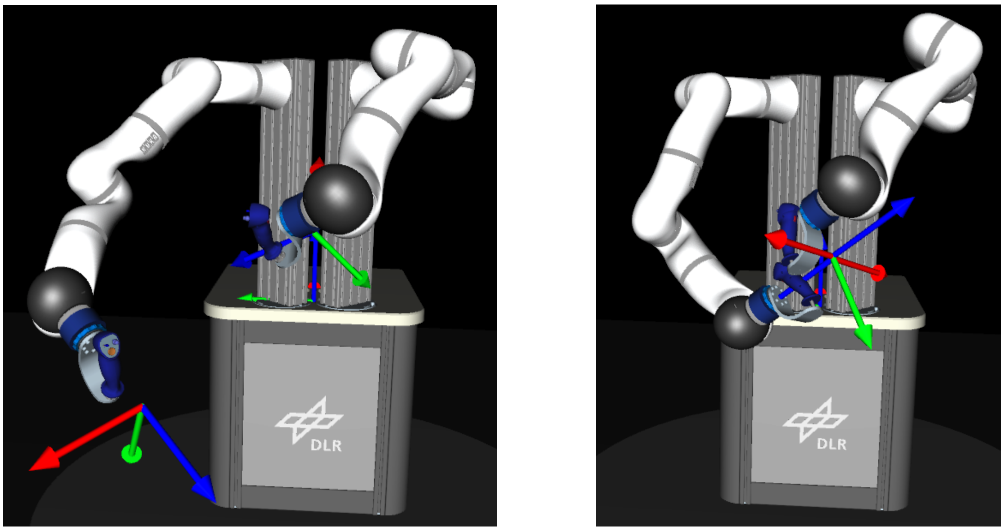

(a) Initial configuration **(b)** Final configuration

Figure 4.11: Configurations of the virtual setup

The following are the initial values of the simulation parameters:

$$\boldsymbol{q}_c = [-1.571, 0.785, 1.571, -0.611, -0.785, 0.785, 0]^T \text{ [rad]} \tag{4.26}$$

$$\boldsymbol{q}_t = [-0.106, -1.186, 1.384, 1.016, -1.083, -1.091, 0]^T \text{ [rad]} \tag{4.27}$$

$$\boldsymbol{F}_{max} = [40, 40, 40, 40, 40, 40]^T \text{ [N]} \tag{4.28}$$

$$\boldsymbol{\alpha} = [15, 15, 15, 9, 9, 9]^T \tag{4.29}$$

$$\boldsymbol{K}_p = \text{diag}\,(3600, 3600, 3600, 1200, 960, 900) \tag{4.30}$$

$$\boldsymbol{K}_d = \text{diag}\,(140, 140, 140, 25, 25, 50) \tag{4.31}$$

The initial configuration of the virtual setup, indicated by (4.26) and (4.27), is shown in figure a of Figure 4.11. This configuration was particularly chosen to avoid as much as possible the boundary singularities of Robot C that could occur when the manipulator is outstretched. In particular, this was expected to occur with the smaller masses of the base spacecraft.

Figure b of Figure 4.11 depicts the final configuration of the two robots and a successful capture of the target after a simulation of 40 s.

4.4.2 Results and conclusions

I simulation study

Figure 4.12, Figure 4.13 and Figure 4.14 illustrate results of the simulations with $m_b = 724.10$ kg, $m_b = 45.256$ kg and $m_b = 2.829$ kg, respectively. Figure 4.12 shows the identical behavior of Robot C as in Figure 4.8, since the inertial pa-

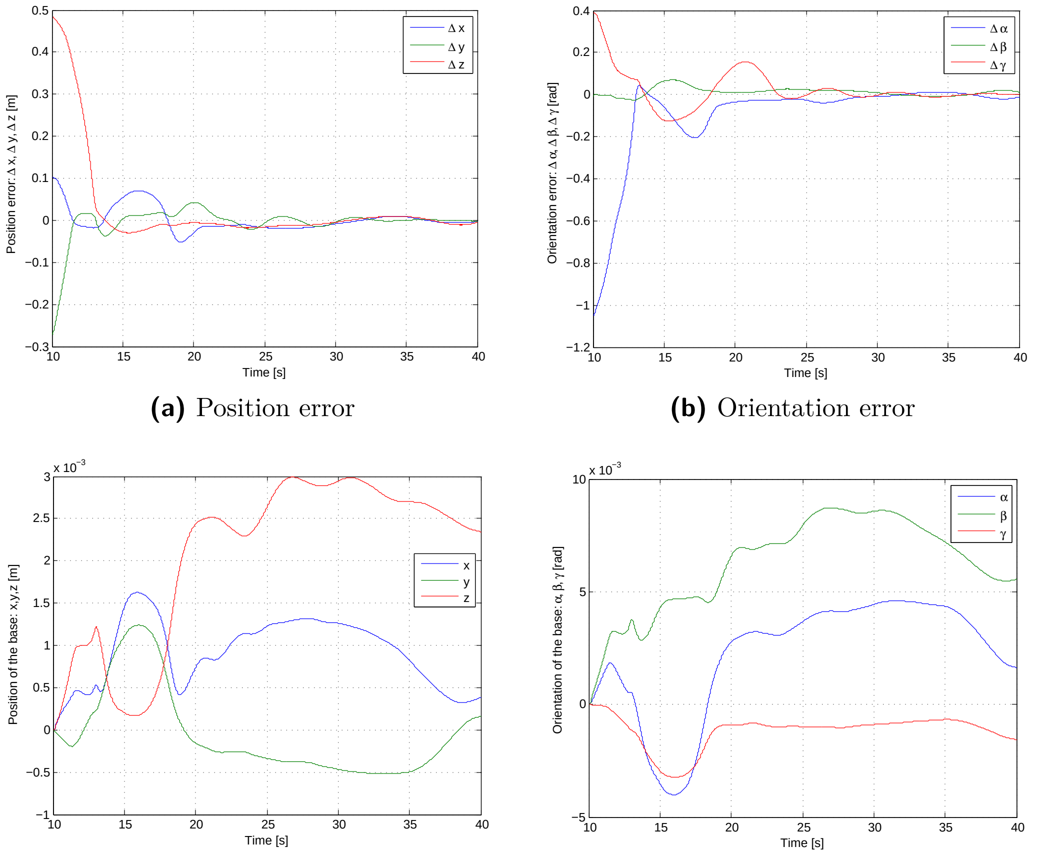

(a) Position error

(b) Orientation error

(c) Absolute position of the base

(d) Absolute orientation of the base represented by the Euler angles 321 (γ, β, α)

Figure 4.12: Results of the first simulation study: $m_b = 724.10\,\text{kg}$

rameters of the carrier spacecraft are identical. Moreover, the initial conditions of the simulation and the motion of the manipulator are the same as those described in Section 4.3.

Figure 4.13 and Figure 4.14 illustrate the results of the simulations relative to $m_b = 45.256\,\text{kg}$ and $m = 2.829\,\text{kg}$. Form both figures it can be noticed that the controller, unlike in Section 4.3, is not capable to properly compensate the pose error, given the considerable motions of the base. The thicker parts of the curves indicate that Robot C has reached a boundary singularity and that thus the Target is outside its reachable workspace. This condition is visible in Figure 4.15 and illustrates the moment after the chaser manipulator has reached a boundary singularity.

II simulation study

The results of the second simulation study are visible in Figure 4.16, Figure 4.17 and Figure 4.18. With respect to the previous results all the figures present

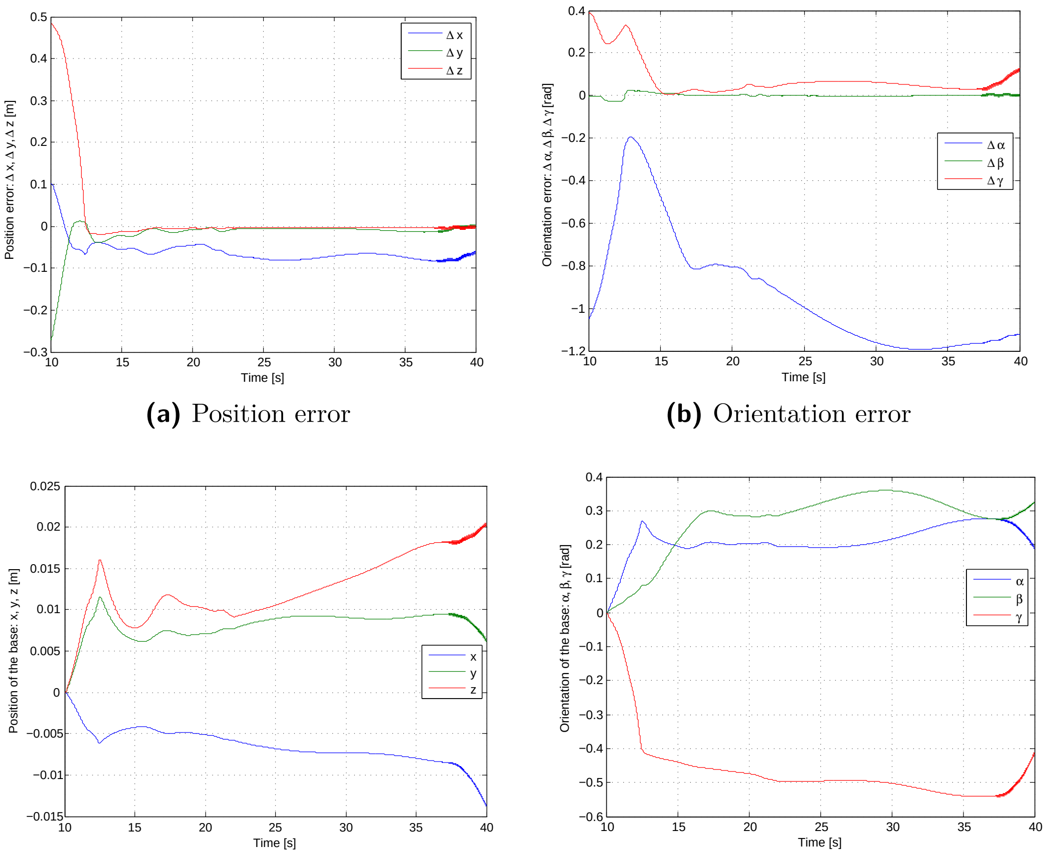

(a) Position error

(b) Orientation error

(c) Absolute position of the base

(d) Absolute orientation of the base represented by the Euler angles 321 (γ, β, α)

Figure 4.13: Results of the first simulation study: $m_b = 45.256\,\mathrm{kg}$

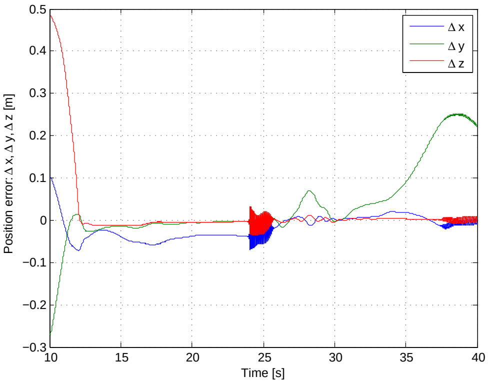

(a) Position error

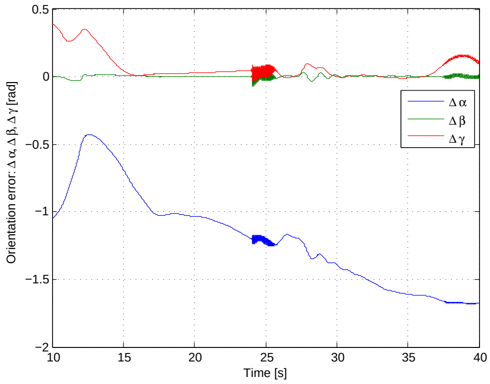

(b) Orientation error

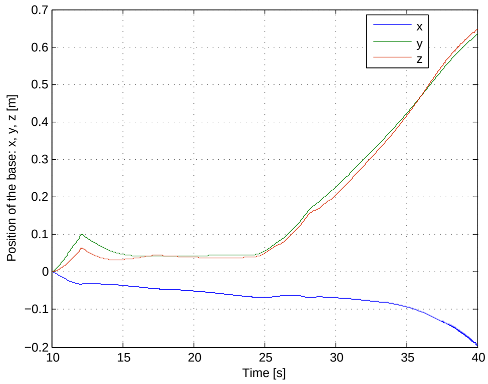

(c) Absolute position of the base

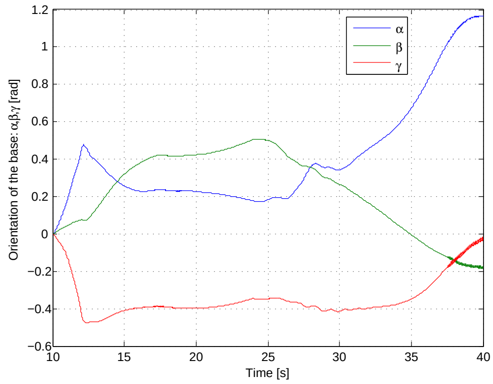

(d) Absolute orientation of the base represented by the Euler angles 321 (γ, β, α)

Figure 4.14: Results of the first simulation study: $m_b = 2.829\,\text{kg}$

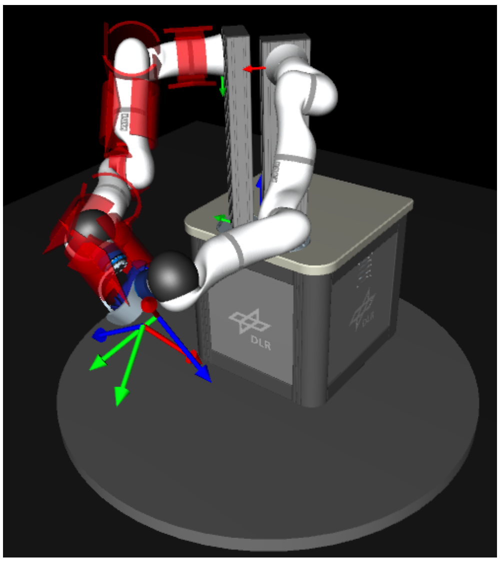

(a)

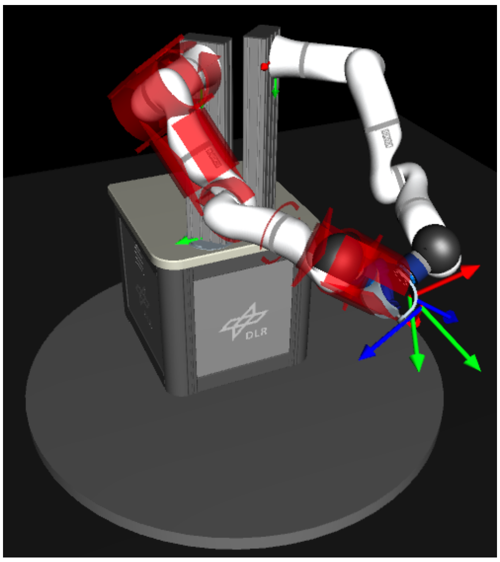

(b)

Figure 4.15: Boundary singularity

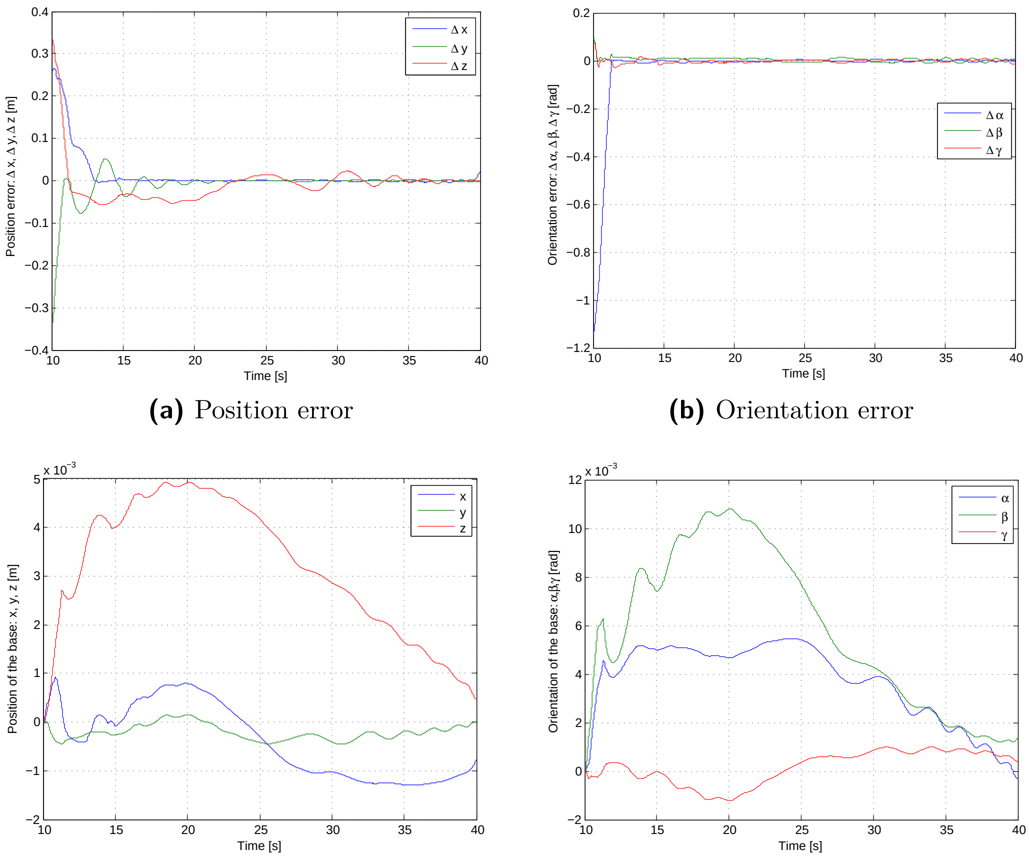

(a) Position error

(b) Orientation error

(c) Absolute position of the base

(d) Absolute orientation of the base represented by the Euler angles 321 (γ, β, α)

Figure 4.16: Results of the second simulation study: $m_b = 724.10\,\mathrm{kg}$

considerable improvement given the higher gains of the PD controller and the optimized initial configuration of the robots. In particular, Figure 4.17 proves that with the proper tuning of the parameters the developed control scheme can be used to successfully simulate the pre-contact phase of the capture maneuver even if the base satellite has the mass comparable to that of the manipulator. However, it must be acknowledged that, with this control scheme and with the base having smaller mass than the manipulator, considerable position errors will arise due to high motion rate of the base itself if the capture time is below 40 s.

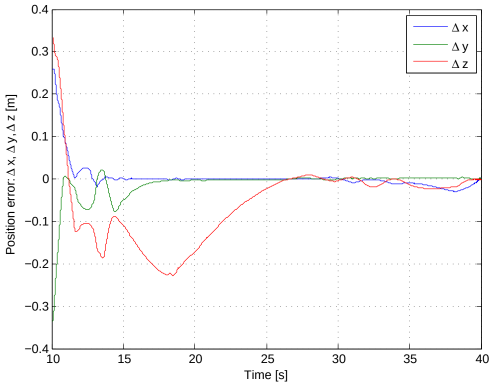

(a) Position error

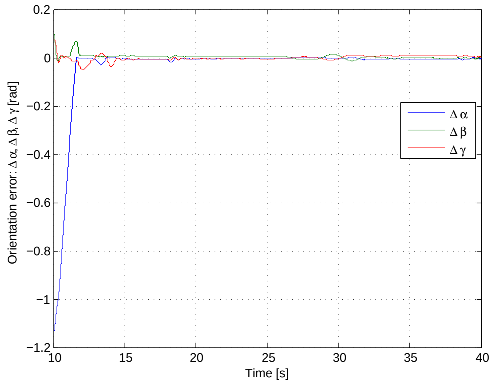

(b) Orientation error

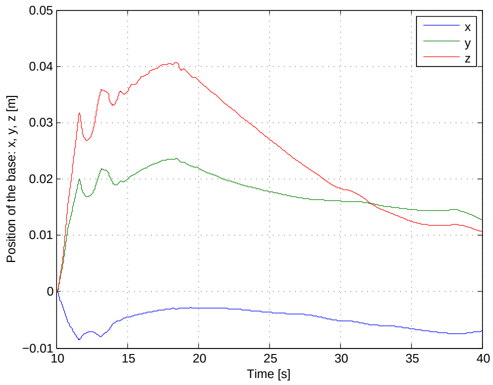

(c) Absolute position of the base

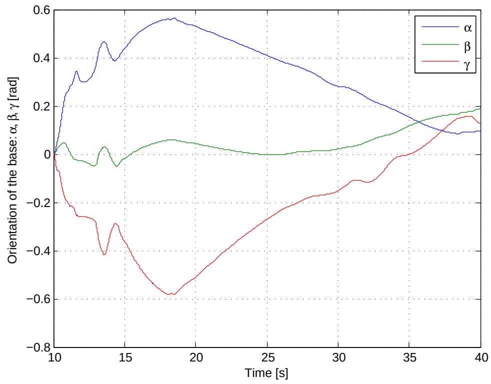

(d) Absolute orientation of the base represented by the Euler angles 321 (γ, β, α)

Figure 4.17: Results of the second simulation study: $m_b = 45.256\,\mathrm{kg}$

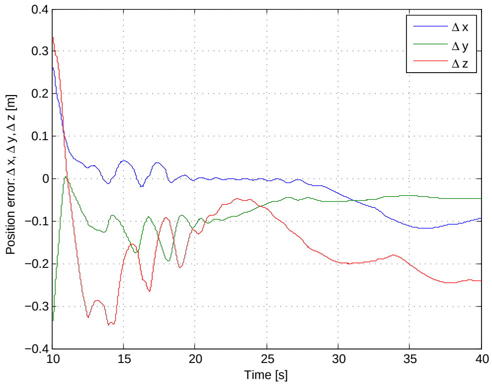

(a) Position error

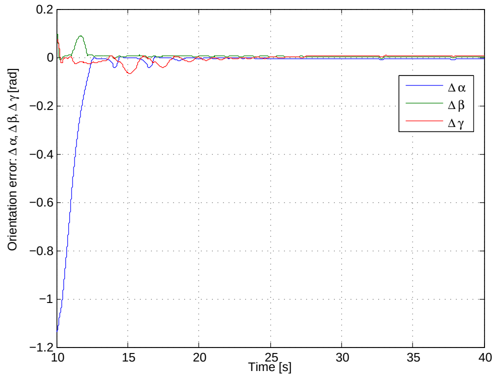

(b) Orientation error

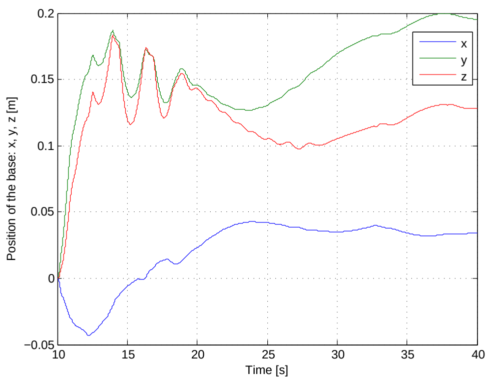

(c) Absolute position of the base

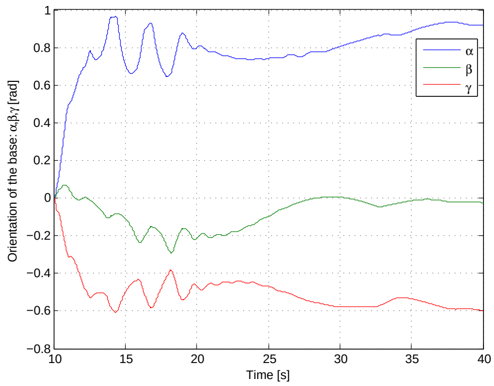

(d) Absolute orientation of the base represented by the Euler angles 321 (γ, β, α)

Figure 4.18: Results of the second simulation study: $m_b = 2.829\,\mathrm{kg}$

5 Experimental Validation

This chapter presents the experimental validation of the developed ground simulation facility to simulate the approach phase of the DEOS mission.

To this end, Section 5.1 introduces the cause and the objective of the experimental validation as opposed to the numeric validation of the system encountered in the previous chapter. Next, Section 5.2 illustrates the basic components of the ground simulation facility, such as the mechanical components and the computer control architecture, necessary to perform the experiments. Detailed operation procedures and precautions for running the hardware-in-the-loop simulation facility can be found in Appendix C. Section 5.3 describes in detail the four categories of the performed experiments, defined to test in a step-wise-manner the main concerns and issues of the simulation facility. Furthermore, Section 5.4 defines the validation criteria used for the evaluation of the test results. Finally, the results of the experiments are presented in Section 5.5.

5.1 Cause and Objective

Computer simulations are a valuable tool for the development of any complex robotic system. Their extensive usage, in the early phases of a project, generally lead to an enhanced design and preliminary performance verification of the system prior to its experimental use. However, it must be noted that the accuracy of a generic numeric simulation depends greatly on the fidelity of the employed mathematical models, usually including nonlinearities and uncertainties due to imposed simplifications and assumptions. This is certainly the case of the numeric simulations of the robotic system developed at the DLR IRMC, for the simulation of the capture maneuver of the DEOS mission, seen in Chapter 4. To overcome this limitation in a cost-effective manner and, at the same time, be able to evaluate the real potential of the system, instead of trying to precisely model all the details of the HIL simulation facility, the experimental validation of the latter was performed. In other words, the primary goal of the validation process was to experimentally demonstrate the ability of the developed laboratory simulator to reproduce dynamic behavior of the free-floating robot of the DEOS mission, during the approach phase, in accordance with the results of the numeric simulations illustrated in Section 4.4 on page 104.

In order to achieve this a series of test cases were developed varying their general complexity from the simplest test, i. e. the free-space test, where the Servicer's manipulator was moved manually, to the most complex approach phase test.

5.2 Setup of the Experimental System

5.2.1 Mechanical configuration

The mechanical configuration of the experimental HIL system, visible in Figure 5.1, consists essentially of the multimodal haptic Human Machine Interface (HMI) to which the following two end-effectors are attached: the satellite mockup of the target spacecraft and the SCHUNK servo-electric 2-finger parallel gripper PG 70.

The specifications of the HMI, composed of two LWRs of the third generation fixed to the rigid platform by means of a supporting aluminum structure, can be found in Section 3.1 on page 63.

The characteristics of the Target mockup, on the other hand, are described in detail in Subsection 3.4.3 on page 90.

The most significant parameters of this end-effector, to have in mind during

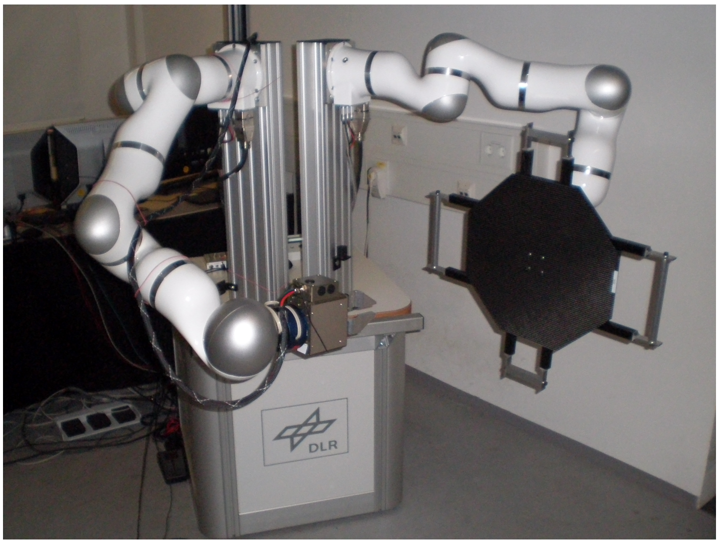

Figure 5.1: Mechanical configuration of the experimental laboratory setup developed at DLR IRMC

the experiments, are:

- its mass, m;
- its c. g. position, ${}^7\boldsymbol{p}_{cg}$ (calculated with respect to the reference frame of the 7^{th} joint of Robot T);
- the position of its tool frame or namely the position of Σ_2 (visible in Figure 2.20 on page 60). This parameter is specified by the homogeneous transformations matrix, ${}^7T_{tool}$, once again calculated with respect to the reference frame of its 7^{th} joint.

The first two characteristics are required by the control algorithm for the correct compensation of the gravity effects acting upon the mentioned end-effector while the third identifies Robot C's grasping point.

The m and ${}^7\boldsymbol{p}_{cg}$ of the satellite mockup are defined by the vector $\left[m, {}^7\boldsymbol{p}_{cg}\right]^T \in \mathbb{R}^{4\times1}$, having the following expression

$$\left[m, {}^7\boldsymbol{p}_{cg}\right]^T = [1.3974\,\text{kg}, 0\,\text{m}, 0\,\text{m}, 0.1477\,\text{m}]^T \tag{5.1}$$

while the relative homogeneous transformations matrix, ${}^7T_{tool}$, is

$${}^7T_{tool} = \begin{bmatrix} 1 & 0 & 0 & 0 \\ 0 & 1 & 0 & 0.305 \\ 0 & 0 & 1 & 0.158 \end{bmatrix} [\text{m}] \tag{5.2}$$

The SCHUNK servo-electric 2-finger parallel gripper PG 70, illustrated in Figure 5.2, is a universal gripper with accurate gripping force, integrated control and power electronics. This way, the module does not require any additional external control units a part from an external power supply unit and a communicator for EtherCAT.

In order to function correctly the voltage and the current on the external power supply unit have to be tuned precisely to 24 V(DC) and 0.2 mA, respectively, for the integrated electronics and to 24 V(DC) and 0.4 mA, respectively, for the motor of the gripper [10]. Further informations and specifications of the PG 70 gripper can be found in [56].

The most significant parameters of this end-effector to have in mind during the experiments, similarly to those enlisted for the satellite mockup earlier, are :

- its mass, m;
- its c. g. position, ${}^7\boldsymbol{p}_{cg}$;

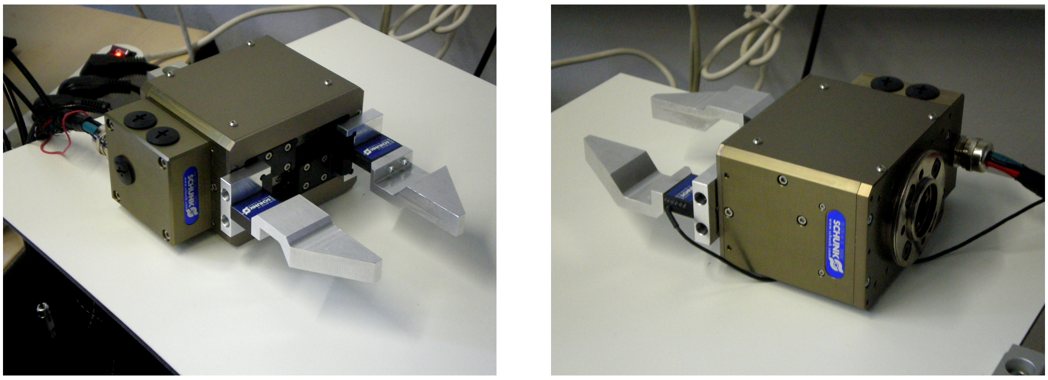

(a) Oblique view of the front **(b)** Oblique view of the back

Figure 5.2: SCHUNK servo-electric 2-finger parallel gripper PG 70

- the position of its tool frame or namely the position of Σ_3 (visible in Figure 2.20 on page 60).

The PG 70 gripper presents the vector of mass and c. g. position as follows

$$\left[m, {}^7\boldsymbol{p}_{cg}\right]^T = [1.790\,\text{kg}, -0.0007296\,\text{m}, -0.007897\,\text{m}, 0.2051\,\text{m}]^T \tag{5.3}$$

while the homogeneous transformations matrix ${}^7T_{tool}$, indicating this time the position of the reference frame Σ_3 (illustrated in Figure 2.20 on page 60) is

$${}^7T_{tool} = \begin{bmatrix} 1 & 0 & 0 & 0 \\ 0 & 1 & 0 & 0 \\ 0 & 0 & 1 & 0.320 \end{bmatrix} [\text{m}] \tag{5.4}$$

5.2.2 Control architecture

The control architecture of the setup consist of two Dell workstations:

- the *host* computer, running a Unix-like operating system;
- the *real-time* computer, running the VxWorks real-time operating system.

The *host* computer runs the user interface of the whole system, i. e. the Simulink models: HMI2010, visible in Figure 3.6 on page 72, together with that of the PG 70 gripper, and provides the software development tools.

The control software is downloaded via Ethernet form the *host* computer to the *real-time* computer which uses the pose error between the tool frames Σ_2 and Σ_3 to determine the generalized control torque vector that is than commanded to Robot C in order to track and capture the Target mockup. The motion of the latter, according to the second mode of the kinematic equivalence illustrated in

Figure 3.12, is based on the absolute motion of the target satellite (see (3.10)) and the absolute pose of the carrier spacecraft which is obtained directly from the dynamic emulation block of the space robot.

The control software of the PG 70 gripper is a stand-alone, in-house developed, algorithm with its own user interface. Therefore a generic experiment of the approach phase of the DEOS mission requires the coordinate use of the PG 70 control software and of the HMI2010 model.

The dynamic emulation of the space robot is performed using the SpaceDyn model of the free-floating manipulator instead of using its SIMPACK model, described in Subsection 3.2.3 on page 70. This discrepancy between the real-time and simulation models of the HIL system is justified by the last moment discovery that SIMPACK models can not be compiled for the computer running the VxWorks operating system. As a result of this discovery, the Simulink block of the space robot model used in Section 4.4 on page 104, developed with SIMPACK, was substituted with the block providing the identical functionality and having the same characteristics of the chaser spacecraft as those illustrated in Subsection A.4.2 on page 138 developed instead with the *SpaceDyn* subroutines.

The *SpaceDyn* is a MATLAB Toolbox developed by the Space Robotics Lab of Tohoku University of Japan for the kinematic and dynamic analysis as well as for the simulation of multi-body systems having a free-floating base. It is is a collection of subroutines that are able to compute the acceleration, velocity and position of:

- the centroid of the base body;
- the centroid of each body;
- the endpoints;
- the joints;

by using dynamic equation of a space robot (3.1) (including gravity terms not present in the mentioned equation), together with (3.2) and (3.3).

The toolbox can be freely downloaded from Spacedyn Webpage and its development was inspired by the work of Peter Corke, Robotics Toolbox [57].

5.3 Test Cases

The test cases were defined to address the main concerns and issues regarding the design and operation of the simulation facility, or in other words to validate

Table 5.1: HIL validation test cases

Test ID	Test category	Purpose of the test	No. of runs
FS	Free-space test	Validate HIL capability to simulate the free-space motion	2
AF	Applied force test	Validate HIL capability to simulate the free-space motion even with external forces applied to the Client	4
FF	Free-flying test	Validate HIL capability of simulating DEOS *free-flying* approach phase	4
FT	Flight test	Validate HIL capability of simulating DEOS *free-floating* approach phase, namely flight test	4
Total number of test runs			14

its capability to faithfully reproduce the dynamic behavior of the space robot of the DEOS mission during the approach phase.

To check a particular level of validity of the HIL setup, the test cases were divide in to four different test categories each having certain number of test runs (cases), as illustrated in Table 5.1. The cases of a particular test category differ from each other in test conditions, developed within the scope of that particular category. The test cases are identified using the test ID (representing its test category) accompanied with a number (representing its run number), as it can be noticed from Table 5.1. For example, AF-2 indicates the second test case of the applied force test category.

The general complexity of the test categories increases in a stepwise manner from top to bottom of Table 5.1, starting with the simplest free-space test (Figure 5.3) and finishing with the most realistic test among them all (Figure 5.6). This particular test design, from-simple-to-complex with the gradual increase of the complexity of single tests, appeared to be necessary for a cost-effective evaluation of the HIL system given the unavailability of validated free-floating dynamic behavior of the space robot. In other words, given the absence of validated data, the evaluation of the final tests would appear almost impossible without going through simpler and much more understandable test cases first. This would be particularly true for unsuccessful test cases or unpredicted behavior of the system during a generic test run. The intermediate test categories considered in this study include the free-space test, the applied forces test and the free-flying test.

The inertial parameters of the servicer spacecraft, used during the test cases, are illustrated by the first two cases of Subsection A.4.2 on page 138. That is by the $m_b = 181.025\,\mathrm{kg}$ and $m_b = 45.256\,\mathrm{kg}$ cases. The $m_b = 181.025\,\mathrm{kg}$ case was particularly interesting for the validation of the setup's capability to simulate the DEOS mission. In fact, with these inertial parameters the simulated version of the servicer spacecraft represents the scaled version of the spacecraft that will be employed during the DEOS mission (see Section 2.1 on page 28). This is why this particular case was used for the last three test runs of the FT test category whose main purpose was to validate the capability of the laboratory setup to simulate the approach phase of the DEOS mission.

The sign of the first component of the $\boldsymbol{p}_{cm_0 \to 1}$ vector, indicating the position of the first joint of the manipulator with respect to the body reference frame of the base spacecraft, was negative in all test cases, based upon the results of the numeric simulations. This was necessary in order to obtain conspicuous motion of the free-floating base, during the motion of the mounted manipulator, and thus to simulate the worst case scenario.

The inertial parameters of the client spacecraft are described in (4.1) on page 93. Its initial motion was assumed to be either non existent (as for the first two test categories of Table 5.1) or to be a simple constant rotation around the z axis of its body reference frame, at an angular velocity of $0.0698\,{}^{\mathrm{rad}}/_{\mathrm{s}}$, as in Chapter 4.

The initial configuration of the LWRs and the parameters of the PD controller were determined prior to any test and always on a test case basis. This way different different test conditions (within the scope of the particular test category) were obtained for every single test run.

Finally it is necessary to specify that a generic test run was divided in to two different stages for practical and precautionary measures: the initialization phase and the actual test phase. The first phase was used, just as in Chapter 4, for reaching the desired initial configuration of the HIL facility while the second phase is self explanatory.

5.3.1 Free-space tests

The test cases within this test category have been conducted by manually moving the Servicer's manipulator, i. e. Robot C or LWR4, and observing the consequent motion of the Client due to the projection of the Servicer's motion on to the client spacecraft.

The objective of this test category was to visually verify the implementation of the (2.36) on page 62 and thereby verify the capability of the laboratory setup

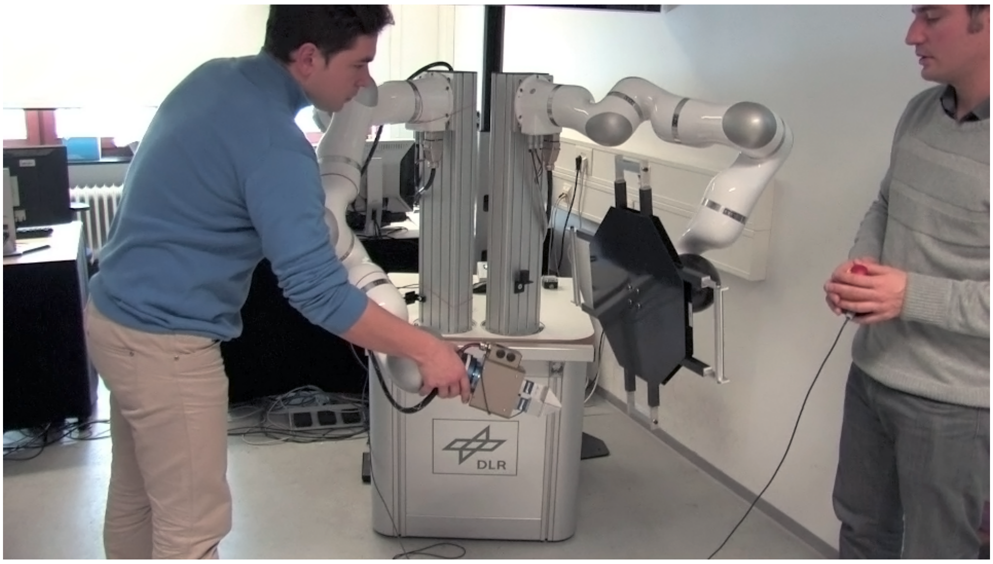

Figure 5.3: Free-space test

to simulate the free-floating dynamics of the space robot.

To this end, once that the platform has been placed into the the desired initial position, the configuration of Robot C was changed by an operator, visible in Figure 5.3 on the left. For safety reasons, during the experiment, there was always present another operator, visible in Figure 5.3 on the right, who simply observed the experiment, ready, in case of emergency, to press the panic button to freeze the platform and thus stop the experiment.

The considered inertial parameters of the servicer spacecraft are those described by the $m_b = 45.256\,\mathrm{kg}$ case in Subsection A.4.2 on page 138. The choice of that mass case instead of the $m_b = 181.025\,\mathrm{kg}$ was deliberate since only the former case was able to guaranty both visibly appreciable motions of the client spacecraft and within the workspace of Robot T.

The test runs within this test category differ from each other in the initial configuration of the platform and in the motion of Robot C during the experiment. The initial configurations of the two robots were chosen based on the the following criteria:

- make more visible the projection of the Servicer's base motion on to the Client;
- prevent the collision between the target mockup and Robot T during the experiment.

The motions of LWR4, on the other hand, were random and not established in advance although they were within the expected range of motions that the space manipulator would have during a generic approach phase.

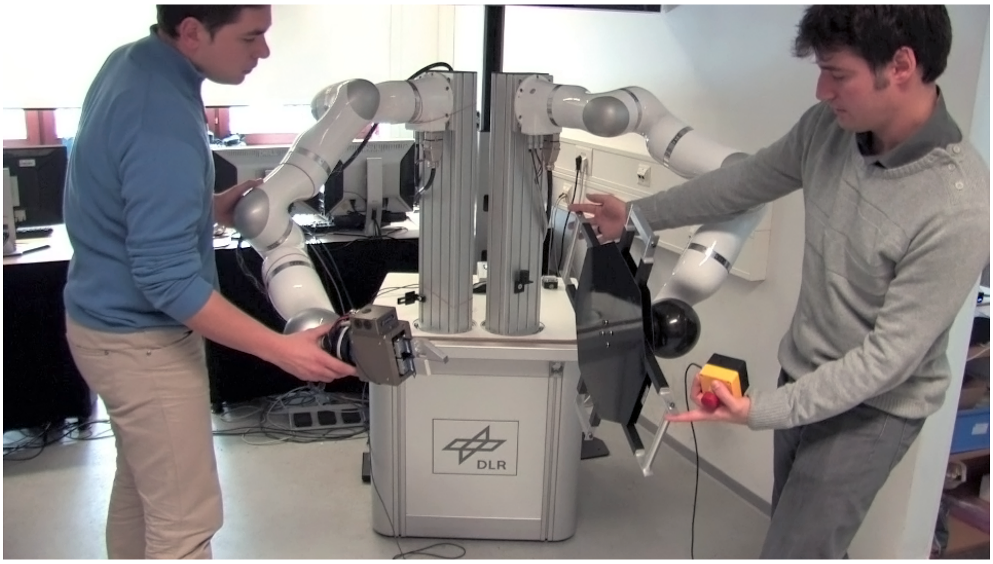

Figure 5.4: Applied forces test

5.3.2 Applied force tests

The test cases considered in this subsection have been conducted essentially in the same way as the experiments in the first category although this time external forces were applied to the client spacecraft before and during the motion of the space robot, i. e. LWR4.

The purpose of this category of experiments was to observe and validate the ability of the laboratory setup to simulate the free-floating dynamics of the space robot by projecting its motion on to the client spacecraft having its own independent motion.

To achieve this, after positioning the laboratory setup in the desired initial configuration, the client satellite was given a rotational motion around the z axis of its body reference frame. This motion was the result of a torque manually applied to the center of mass of the Client mockup, as illustrated in Figure 5.4. The operator who carried out this task was also responsible for the panic button.

Only at this point the manual motion of the LWR4 was permitted. Note that during the experiment, the initial rotational motion of the mockup was changed couple of times applying additional torques and forces to the c. m. of the mockup, causing not only the rotation of the Client around its c. m. but at also the translation of it in the inertial space.

The test runs within this test category differ from each other in: the initial configuration of the platform, the motion of Robot C and the applied forces and torques. The criteria used for the selection of the initial configurations of the two robots of the first set of tests are valid also in this test category. The same applies to the considerations made for the manual motions of LWR4. The magnitude and direction of the forces and torques applied to the mockup during the test runs were chosen randomly on a case basis although with the aim to keep the satellite mockup within the workspace of LWR3 for as long as possible. Regarding the inertial parameters of the servicer spacecraft, the same applies as in the previous subsection.

5.3.3 Free-flying tests

The test cases within this test category represent the simulations of the capture phase of the DEOS mission, considering the free-flying servicer spacecraft. The free-flying nature of the space robot can be achieved either by means of producing external forces and moments, to counteract the dynamic coupling between the manipulator and the spacecraft with the AOCS, or considering the carrier spacecraft with a mass of at least two orders of magnitude bigger than that of the mounted manipulator.

The objective of this set of experiments was to verify the ability of the developed setup to simulate the capture phase of the non-cooperative satellite considering a free-flying space robot and thus validate the implementation of the PD controller, developed by De Stefano M.

Each experiment was performed in two different phases, as described in detail in Section 4.1 on page 92:

1. the initialization phase;
2. the approach phase.

However, compared to the numerical simulations, this set of tests does not take into account the output signal of the *Space Robot Model* block (see Figure 3.12), given the free-flying nature of the space robot.

The initial conditions of the HIL system in all test cases were similar to those of the default configuration, defined in Section 4.1 on page 92. The reason is to be found in the similarity of the experiments with those considered in [10].

The inertial parameters of the servicer spacecraft are irrelevant in this category, given its free-flying nature, while those of the client spacecraft are described in (4.1). Its initial motion was considered to be a simple constant rotation around the z axis of its body reference frame, at an angular velocity of $0.0698\,\mathrm{rad/s}$, as it was evidenced in the previous section.

The test runs within this test category are four and they were designed with increasing general complexity. They differ respectively in: values assigned to the control parameters (in FF-2 and FF-3), position of the tool frame Σ_2 (in FF-3 and FF-4) and initial configuration of LWR4 (in FF-3 and FF-4).

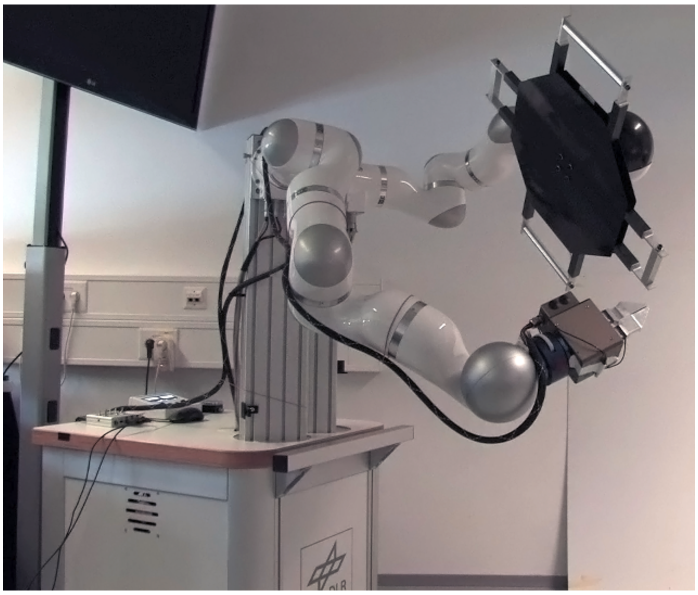

Figure 5.5: Free-flying test

Note that the first two experiments were performed with the closed gripper. Thus, to prevent collisions between the gripper and the mockup, the tool frame of Robot T, Σ_2 , was intentionally displaced with respect to its original position, defined in (5.2). This way, the gripper approached and tracked a point positioned at certain distance from the grappling fixture of the mockup, as depicted in Figure 5.5. On the other hand, the last two experiments were performed with the opened gripper and thus it was possible to consider the original tool frame of Robot T, indicated in (5.2).

5.3.4 Flight tests

In a real flight scenario, the capture phase of the DEOS mission will involve the acquisition, the tracking and the grasping of the dedicated fixture, of the non-cooperative target satellite, with the end-effector of the free-floating space robot. Therefore, it is essential to examine in depth the capabilities and limitations of the control algorithm by thoroughly testing the capture maneuver on the ground under realistic conditions of the space environment.

To this end this particular test category aims to validate the capability of the developed robotic gravity compensation system to simulate the acquisition and the tracking of a point fixed to the tumbling target spacecraft, using the developed "*angle*" control scheme, depicted in Figure 3.12 on page 83.

Based on the numeric simulations (see Section 4.1), the test cases within this test category were performed by initially placing the system in its initial configuration and than starting the simulation of the pre-contact phase of the capture maneuver.

The initial conditions of the hardware-in-the-loop, simulation facility in all test runs were a combination of those of the default configuration and those used in the II simulation study of Section 4.4. The reason of this choice was the desire to obtain the initial configuration of the robots as similar as possible to that illustrated in the II simulation study of Section 4.4, while using the parameters of the PD controller optimized for the experiments.

The initial conditions used in the test cases are the following:

$$\boldsymbol{q}_c = [-1.571, 0.785, 1.571, -0.611, -0.785, 0.785, 0]^T \text{ [rad]} \tag{5.5}$$

$$\boldsymbol{q}_t = [-0.281, -1.360, 1.384, 0.492, -0.909, -1.615, 0.273]^T \text{ [rad]} \tag{5.6}$$

$$\boldsymbol{F}_{max} = [12, 12, 12, 5, 5, 5]^T \text{ [N]} \tag{5.7}$$

$$\boldsymbol{\alpha} = [5, 5, 5, 1, 1, 1]^T \tag{5.8}$$

$$\boldsymbol{K}_p = \text{diag}\,(350, 350, 350, 100, 100, 100) \tag{5.9}$$

$$\boldsymbol{K}_d = \text{diag}\,(50, 50, 50, 10, 10, 10) \tag{5.10}$$

Note that the initial configuration of Robot T, in the example, differs slightly from that of the virtual setup. This is due to the fact that the $\boldsymbol{q}_t$ vector used in the II simulation study of Section 4.4 revealed not to be suitable for the experiments. Indeed, the position of Σ_2 in the II simulation study was considered to be coincident with the origin of the reference frame of Robot T's end-effector instead of being equal to (5.2)(see Figure 5.6). Furthermore, consider that the initial conditions of the FT-4 case were similar to those previously illustrated although not identical, as it is evidenced further on.

The inertial parameters of the servicer spacecraft were those described by the first two cases of Subsection A.4.2 on page 138 (i. e. $m_b = 181.025\,\text{kg}$ and $45.256\,\text{kg}$), as it was evidenced in previous section.

The mass and geometry properties of the client spacecraft as well as its initial motion were the same as in Subsection 5.3.3.

Based on the experiments of the previous subsection, the test cases within this test category were designed in a similar manner. The test runs are four and are characterized by increasing general complexity. The FT-1 was performed considering the initial configuration of the HIL system described at the beginning of this subsection. The mass of the free-floating base was 45.256 kg and the position of the tool frame Σ_2 was intentionally displaced with respect to its original value for the same reason expressed in Subsection 5.3.3. The FT-2 was identical to the first run except for the mass of the Servicer which in this case was 181.025 kg.

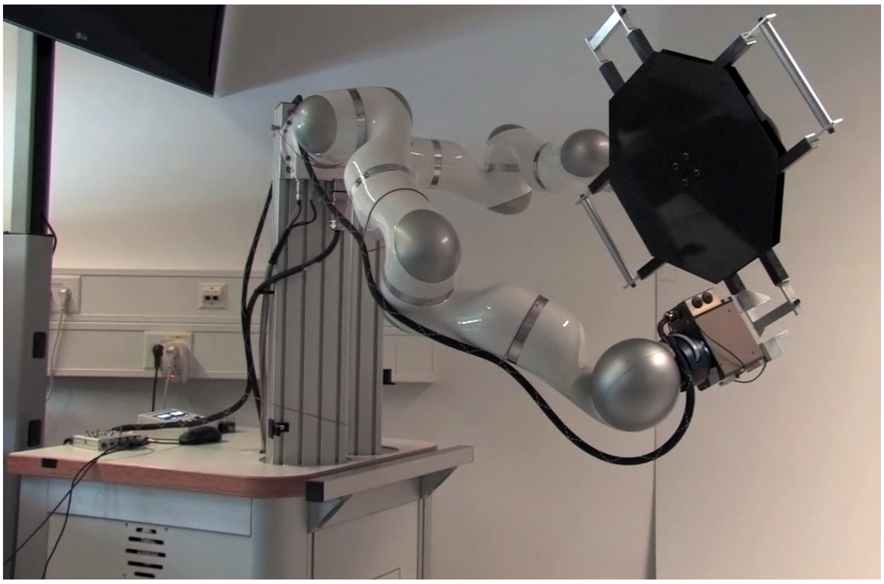

Figure 5.6: Flight test

The FT-3 was a repetition of the previous test case although this time the duration of the experiment was a bit longer. The FT-4, in the end, was conducted similarly to the previous runs with the difference that the original tool frame of Robot T, described by (5.2), was considered. In order to implement this and avoid collisions between the gripper and the satellite mockup the former was in the opened position during the whole test. The mass of the servicer spacecraft was 181.025 kg and the $\boldsymbol{K}_p$ and $\boldsymbol{K}_d$ values of the PD controller were those illustrated at the beginning of this subsection. However, the initial configuration of Robot C was different from that used in the previous cases (see (5.5)) while that of Robot T was identical to the one described by (5.6). The reason for this modification was the necessity to test the ability of the robot's control algorithm to approach the Target starting form a different initial configuration. The initial configuration of Robot C was achieved by manually acting on the joints of the robot.

5.4 Validation Criteria

The validation criteria in this study was defined as the maximum allowed variation for the errors between the physical test and relative numeric simulation. Furthermore, based on the comparison method between the results, two types of the validation criteria have been identified [50]:

- task-based;
- performance-based.

The *task-based* comparison strategy takes into account only the overall performance of the tests (e. g. success, failure, total time of the operation) without comparing their dynamical performances in time. The *performance-based* comparison method, on the other hand, takes into account detailed dynamic performance of the physical and virtual system during the experiment. Typically, the comparison is made between the transient peaks, steady-state values, frequencies, and phase differences of the target dynamic responses against the corresponding simulated quantities. This fact makes the latter comparison strategy more precise but at the same time more time consuming especially if the distinction between different types of errors (e. g. errors from dynamics models, numerical process and measurement systems), generally affecting the results, is required. The task-based strategy, on the other hand, is relatively easy to apply because it avoids detailed analysis of dynamic responses. Consequently the latter is more suitable as the first level of validation of the laboratory setup.

Consistently with the two comparison methods, described previously, two different validation criteria of the developed robotic laboratory setup have been be identified: task-based validation criteria and performance-based validation criteria. The task-based criteria are based on the task-based comparison method while the performance-based criteria are based on the performance-based comparison method.

The task-based criteria were those chosen in this study for the evaluation of the results obtained during the test cases of the last two categories (i. e. the free-flying test category and the flight test category), described in Section 5.3. The reason behind the choice of the task-based criteria instead of the much more precise performance-based criteria is to be found in the absence of the validated numerical model of the system and thus of the validate test data required for by the latter type of criteria.

The task-based criteria defined for the validation purposes were the following:

1. *Overall*: the overall dynamic behaviors of the two systems need to appear similar to an operator without significant and unexplainable abnormalities;

2. *Completion time*: the total time to complete the task (reach a point in space firmly attached to the satellite mockup) must be within the 40 s from the start of the experiment as in the numeric simulations.

The illustrated validation criteria, however, were not used for the evaluation of the results of the first two test categories. The results were evaluated only visually by an operator, based on the expected motions of the client spacecraft in response to the motions of Robot C, as explained in Subsection 5.3.1 and in Subsection 5.3.2. The reason of this decision was the unavailability of the simulation data, necessary for the comparison purposes, given that Robot C's motions were manual and thus not accurately reproducible numerically.

5.5 Results

5.5.1 Free-space tests

The results of the test cases illustrated in Subsection 5.3.1 were all extremely positive since the system responded promptly to various ranges of motion of Robot C, proving that the implementation of the (2.36) on page 62 was correct. Furthermore, only expected motions of the satellite mockup were observed in response to the motions of Robot C, demonstrating the capability of the laboratory setup to precisely simulate the free-floating dynamics of a space robot.

The adequate selection of the inertial parameters of the servicer spacecraft guarantied its motions to be both visibly appreciable by an operator and at the same time within the workspace of Robot T.

As expected, the greatest displacement of the base body were obtained while exciting the first three joints of Robot C which constitute its shoulder.

5.5.2 Applied force tests

Similarly to the results of the previous test category, those obtained from the test cases illustrated in Subsection 5.3.2 were all extremely satisfying. In fact, the system responded promptly and without any irregular dynamic behavior to various ranges of motion of Robot C and external forces applied to its c. m. Thus, the system demonstrated the capability of the laboratory setup to simulate the free-floating dynamics of a space robot having its own independent motion.

The system presented no difficulties neither with the rotation of the Client around its c. m. nor with the translation of it in the inertial space. Once again, the selection of the Client's inertial parameters revealed to be adequate thus ensuring mockup's motions both visibly appreciable by an operator and at the same time within the workspace of Robot T.

5.5.3 Free-flying tests

The results of the test cases described in Subsection 5.3.3 met the task-based criteria defined in Section 5.4. The test cases demonstrated the ability of the developed setup to successfully simulate the capture phase of the non-cooperative satellite by means of a free-flying space robot within the 40 s from the start of the experiment.

The tracking of the predefined point attached to the Target mockup also revealed to be smooth and without unpredicted configurations of LWR4, up to its mechanical limit given by the maximum joint angle range permitted.

The choice of the initial conditions of the HIL system in all test cases revealed to be adequate for the performed experiments.

5.5.4 Flight tests

The results of the test cases defined in Subsection 5.3.4 proved that the robotic HIL system is able to simulate, on ground, the capture maneuver of the DEOS mission under the conditions of the space environment. This implies that the HIL system proved to be capable of simulating, on ground, the free-floating nature of the servicer spacecraft by projecting the motion of its base body on to the client satellite, having its own motion. However, this was only possible by using the inertial parameters of the $m_b = 181.025$ kg case. The $m_b = 45.256$ kg case revealed to be inappropriate for the developed robotic system, having the initial conditions described in Subsection 5.3.4, due to the inability to perform the approach phase within the available workspace. Thus, it can be affirmed that while the FT-1 case did not satisfy the validation criteria, the remaining test cases complied with the defined task-based criteria. Moreover, the approach of the physical robot appeared to be much smoother in comparison with its approach observed in the numeric simulations, confirming the quality of the initial conditions imposed to the system for this category of tests.

Conclusions and Future Developments

Conclusions

The dynamics modeling and motion planning of a free-floating robot, such as the chaser spacecraft of the DEOS mission, are much more complicated than those of a fixed-base robot, due to the dynamic coupling between the manipulator and its base. Thus, to ensure the successful completion of a challenging in-orbit task, such as the capture maneuver of the target spacecraft, ground experimentations of the planning and control algorithms of the space robotic system are required before its launch and effective in-orbit use.

Within this context, this thesis presents the laboratory simulator suitable for the study of the approach phase of a free-floating robotic system. The fundamental idea is to use a hybrid method which combines the mathematical model of the dynamic system with the real hardware, such as the developed laboratory setup. This means, that the dynamical behavior of the whole system is simulated using appropriate dynamic models, while the physical motions of the space manipulator and client satellite are accomplished by two robots. In particular, the emulation of the free-floating base is achieved through the motion of the target spacecraft based on the relative position of the latter whit respect to the chaser spacecraft. This way, the ground setup provides a laboratory environment similar to what an astronaut or a teleoperator would observe form the servicer spacecraft during the capture phase. The developed simulation system is based on the multimodal Human Machine Interface, already used for other purposes at the DLR Institute of Robotics and Mechatronics. The system is composed of two Light-Weight Robots (LWRs) fixed to the rigid platform making the whole system less complex, more reliable and relatively inexpensive, in contrast to other setups that use specially designed robots and configurations to achieve the same task. Furthermore, the working frequency of the LWRs, of 1 kHz, assures minimal time delay between a control command and the physical reaction reaction of the manipulators, in comparison to similar hardware-in-the loop simulation facilities that employ industrial robots working at frequencies of 250 Hz. Moreover, given that the ground system is based on the virtual models of the space robot, it presents no limits regarding the complexity of the space system to be simulated while still retaining a full 6 DOF motion condition. Additionally, the system is easily extendible by small hardware and software modifications. For example, different end-effectors could be mounted and included inside the virtual model of the space robot to study different approach maneuvers. However, it must be noted that the selected system also exhibits few limits with respect to similar HIL designs. For instance, the motion of the target satellite cannot be completely arbitrary since the workspace of the system is limited. Furthermore, if the mass of the chaser spacecraft is similar to that of the manipulator the duration of the capture phase, fixed to 40 s, isn't sufficient and the capture of Target results impossible. Moreover, the workspace of the LWR does not equals that of the space manipulator that will be used. However, since the capture phase occurs generally in the immediate proximity of the client spacecraft the limited workspace of the LWR should be accetable. Furthermore, with an adequate choice of the inertial parameters of the base spacecraft the LWR can be seen as a scaled versions of the manipulator that will be employed during the DEOS mission.

The mockup of the client satellite is another important component of the developed ground facility. Thus, this work also dealt with the development of the new satellite mockup optimized for the particular case study. The design was performed according to the specific requirements, aimed to obtain a light yet rigid structure that could substitute the old mockup in the future experiments of the robotic setup. The final design of the mockup is almost entirely made of carbon-fiber-reinforced polymer and features four radial grappling fixtures, of which, two are designed for the grasping with a gripper while the other two are designed for the capture with the DLR hand.

In the end the preliminary study of an alternative method to the robotic simulation of the Client's motion is developed. The evaluated simulation method is a suspended rotating platform, since this kind of system, being passive, would overcome typical problems of an active systems such as the presence of noise, dead band limits and reaction time. Within this context, the dynamic equations of the gyroscopic pendulum were developed and the initial conditions of the regular precession of the system were found in order to achieve the motion of the platform similar to that of a free tumbling spacecraft.

Future Developments

The work presented in this thesis, like any other research work, is far form being complete and closed to alternative solutions to the problems faced during the development of the laboratory simulator. For instance, refinement of the SpaceDyn model of the free-floating manipulator is also advised, since, at current state, it doesn't include the PG 70 gripper and it does not have a feedback of the forces applied to the end-effector that could arise during the capture and stabilization maneuvers of the target satellite. Additionally, different trajectories and velocities of the end-effector, during the approach maneuver, should be analyzed in order to minimize, as much as possible, the consequent motion of the base spacecraft and optimize the performances of the implemented controller. Moreover, it could be vise to perform an additional two-step experimental validation (as mentioned in[50]) of the developed laboratory simulator by using an already validated facility (such as the EPOS facility) as a reference. This way it could be possible to increase the number of test cases in a cost-effective and time-effective manner. In fact, the task-based criteria could be used to evaluate a large number of test cases while the more time consuming performance-based criteria could be used to evaluate only a selected number of the test runs which have passed the first screening. Note that the test runs that failed in both steps should be analyzed and retested. In other words, the results of all the test cases should be able to pass the task-based criteria while only a small part them should meet the performance-based criteria.

The concept of the suspended rotating platform should be also tackled in depth, analyzing at first the advantages of such kind of system over the existing one and subsequently developing the mathematical model of the system without the approximation considered in this work. For example, dynamics of the momentum bias system should be considered instead of those of the gyroscopic pendulum.

Finally, the comparison of the two operational modes of the DEOS manipulator should be done using the developed laboratory simulator in order to comprehend in depth the advantages and disadvantages of telepresence and automatic control mode during the capture maneuver of the target satellite.

APPENDICES

A Inertial parameters of the Chaser Spacecraft

This appendix describes in detail the inertial parameters, namely the mass, centre of mass position and inertia, of the servicer spacecraft used for the creation of its numerical models. Therefore, at first the definition of the symbols used to describe the inertial parameters of the base spacecraft and its links is given in Section A.1. Subsequently, different inertial parameters are presented according to the dimensions of the mounted manipulator: Section A.2 describes the parameters used for the development of the Chaser's model with the DEOS's manipulator, while Section A.3 contains the parameters used to develop the model with the LWR III. In the end, Section A.4 is dedicated only to the description of the two sets of inertial parameters of the base satellite differing form each other in the overall density of the spacecraft.

A.1 Introduction

The Chaser spacecraft is considered to be composed of eight links, of which the base satellite is the link number zero while the others are the links of its 7 DOF manipulator. The joints of the manipulator are all rotational and the symbols, depicted in Figure A.1, used to describe the inertial parameters of the chaser spacecraft and its links are defined as follows:

${}^{i}\boldsymbol{p}_{i\to cm_i} \in \mathbb{R}^{3\times1}$ the position vector form the origin of Σ_i, centered in the joint i, to in the center of mass (c. m.) of the link i, with respect to Σ_i of the joint.

${}^{i}\boldsymbol{p}_{cm_i\to j} \in \mathbb{R}^{3\times1}$ position vector form the origin of Σ_i, centered in the c. m. of the link i, to that of Σ_j, centered in the joint j, with respect to Σ_i.

The orientation of the reference frame Σ_i, centered in the c. m. of the link i, is considered identical to the coordinate system of the joint i. On the other hand, the orientation of the latter is expressed in Euler angels ZYX or *Roll–Pitch–Yaw*

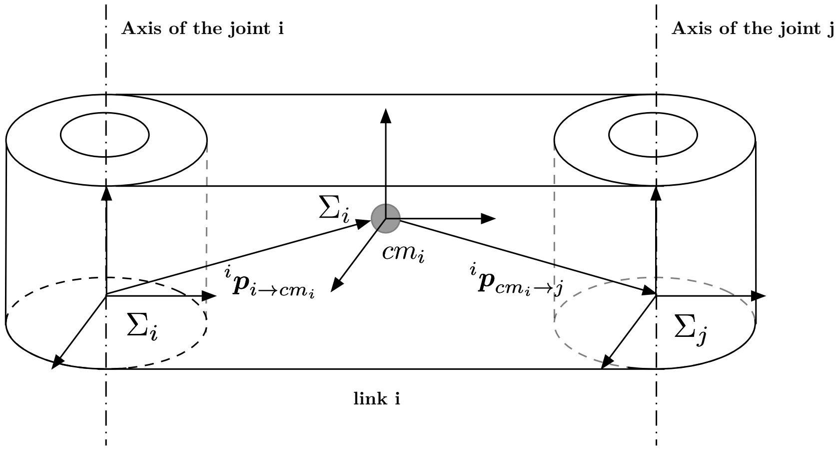

Figure A.1: Position vectors and reference frames of the link i

angles with respect to the coordinate system Σ_{i-1} of the joint $i-1$. The relative coordinate frame for the end-effector is considered to be $\Sigma_{ee} = [0, 0, 0]\,[°]$.

A.2 DEOS' Chaser Spacecraft

The chaser spacecraft in this section is considered to have the default properties of the base satellite and robotic arm, as illustrated in Subsection 3.2.2 on page 69.

The inertial parameters of the Chaser's links used for its virtual SIMPACK model, presented in Subsection 3.2.2, are described hereafter.

Link 0

$$\boldsymbol{p}_{cm_0\to 1} = [0.885, -0.012, 0.870]\,[\mathrm{m}]$$

$$m_0 = 724.10\,[\mathrm{kg}] \quad \boldsymbol{I}_0 = \begin{bmatrix} 277.21 & -11.33 & 21.85 \\ -11.33 & 410.07 & -3.8 \\ 21.85 & -3.8 & 420.26 \end{bmatrix} [\mathrm{kg}\cdot\mathrm{m}^2]$$

Link 1

$$\Sigma_1 = [0, 0, 0]\,[°] \qquad \begin{matrix} {}^1\boldsymbol{p}_{1\to cm_1} = [0, 0.042, 0.128] \\ {}^1\boldsymbol{p}_{cm_1\to 2} = [0, 0.042, 0.128] \end{matrix}\ [\mathrm{m}]$$

$$m_1 = 3.3\,[\mathrm{kg}] \quad \boldsymbol{I}_1 = \begin{bmatrix} 0.0056 & 0 & 0 \\ 0 & 0.0056 & 0 \\ 0 & 0 & 0.0056 \end{bmatrix} [\mathrm{kg}\cdot\mathrm{m}^2]$$

Link 2

$$\Sigma_2 = [-90, 0, 0]\,[°] \qquad \begin{matrix} {}^2\boldsymbol{p}_{2\to cm_2} = [0, -0.66225, 0.042] \\ {}^2\boldsymbol{p}_{cm_2\to 3} = [0, -0.66225, 0.042] \end{matrix} \;[\mathrm{m}]$$

$$m_2 = 3.3\,[\mathrm{kg}] \qquad \boldsymbol{I}_2 = \begin{bmatrix} 0.0056 & 0 & 0 \\ 0 & 0.0056 & 0 \\ 0 & 0 & 0.0056 \end{bmatrix} [\mathrm{kg}\cdot\mathrm{m}^2]$$

Link 3

$$\Sigma_3 = [90, 0, 180]\,[°] \qquad \begin{matrix} {}^3\boldsymbol{p}_{3\to cm_3} = [0, 0.042, 0.063] \\ {}^3\boldsymbol{p}_{cm_3\to 4} = [0, 0.042, 0.063] \end{matrix} \;[\mathrm{m}]$$

$$m_3 = 3.3\,[\mathrm{kg}] \qquad \boldsymbol{I}_3 = \begin{bmatrix} 0.0056 & 0 & 0 \\ 0 & 0.0056 & 0 \\ 0 & 0 & 0.0056 \end{bmatrix} [\mathrm{kg}\cdot\mathrm{m}^2]$$

Link 4

$$\Sigma_4 = [-90, 0, 0]\,[°] \qquad \begin{matrix} {}^4\boldsymbol{p}_{4\to cm_4} = [0, -0.46225, 0.042] \\ {}^4\boldsymbol{p}_{cm_4\to 5} = [0, -0.46225, 0.042] \end{matrix} \;[\mathrm{m}]$$

$$m_4 = 3.3\,[\mathrm{kg}] \qquad \boldsymbol{I}_4 = \begin{bmatrix} 0.0056 & 0 & 0 \\ 0 & 0.0056 & 0 \\ 0 & 0 & 0.0056 \end{bmatrix} [\mathrm{kg}\cdot\mathrm{m}^2]$$

Link 5

$$\Sigma_5 = [90, 0, 180]\,[°] \qquad \begin{matrix} {}^5\boldsymbol{p}_{5\to cm_5} = [0, -0.042, 0.063] \\ {}^5\boldsymbol{p}_{cm_5\to 6} = [0, -0.042, 0.063] \end{matrix} \;[\mathrm{m}]$$

$$m_5 = 3.3\,[\mathrm{kg}] \qquad \boldsymbol{I}_5 = \begin{bmatrix} 0.0056 & 0 & 0 \\ 0 & 0.0056 & 0 \\ 0 & 0 & 0.0056 \end{bmatrix} [\mathrm{kg}\cdot\mathrm{m}^2]$$

Link 6

$$\Sigma_6 = [90, 0, 0]\,[°] \qquad \begin{aligned} {}^6\boldsymbol{p}_{6\to cm_6} &= [0, 0.08225, 0.042] \\ {}^6\boldsymbol{p}_{cm_6\to 7} &= [0, 0.08225, 0.042] \end{aligned}\ [\mathrm{m}]$$

$$m_6 = 3.3\,[\mathrm{kg}] \qquad \boldsymbol{I}_6 = \begin{bmatrix} 0.0056 & 0 & 0 \\ 0 & 0.0056 & 0 \\ 0 & 0 & 0.0056 \end{bmatrix} [\mathrm{kg}\cdot\mathrm{m}^2]$$

Link 7

$$\Sigma_7 = [-90, 0, 0]\,[°] \qquad \begin{aligned} {}^7\boldsymbol{p}_{7\to cm_7} &= [0, 0, 0.24275] \\ {}^7\boldsymbol{p}_{cm_7\to ee} &= [0, 0, 0.06275] \end{aligned}\ [\mathrm{m}]$$

$$m_7 = 7.3\,[\mathrm{kg}] \qquad \boldsymbol{I}_7 = \begin{bmatrix} 0.012 & 0 & 0 \\ 0 & 0.012 & 0 \\ 0 & 0 & 0.012 \end{bmatrix} [\mathrm{kg}\cdot\mathrm{m}^2]$$

A.3 Chaser Spacecraft with LWR III

The chaser spacecraft in this section is considered to have the LWR III mounted on its base satellite, instead of the default robotic arm, as illustrated in Subsection 3.2.3 on page 70.

The inertial parameters of the Chaser's links used for its virtual SIMPACK models, presented in Subsection 3.2.3, are described hereafter.

Link 0

$$\boldsymbol{p}_{cm_0\to 1} = [\pm 0.885, -0.012, 0.980]\,[\mathrm{m}]$$

$$m_0 = 724.10\,[\mathrm{kg}] \qquad \boldsymbol{I}_0 = \begin{bmatrix} 277.21 & -11.33 & 21.85 \\ -11.33 & 410.07 & -3.8 \\ 21.85 & -3.8 & 420.26 \end{bmatrix} [\mathrm{kg}\cdot\mathrm{m}^2]$$

Note that the $\pm$ sign of the first component of the $\boldsymbol{p}_{cm_0\to 1}$ vector depends on whether the position of the manipulator should be that to obtain its motion towards (i. e. $+$) or away (i. e. $-$) from the center of gravity of the base satellite during the approach phase of the DEOS mission.

Link 1

$$\Sigma_1 = [0, 0, 0]\,[°] \qquad \begin{matrix} {}^1\boldsymbol{p}_{1\to cm_1} = [0, 0.01698, 0.14087] \\ {}^1\boldsymbol{p}_{cm_1\to 2} = [0, -0.01698, 0.05913] \end{matrix}\ [\mathrm{m}]$$

$$m_1 = 2.7082\,[\mathrm{kg}] \quad \boldsymbol{I}_1 = \begin{bmatrix} -0.022632 & 0 & 0 \\ 0 & -0.022793 & 0 \\ 0 & 0 & 0.0049639 \end{bmatrix} [\mathrm{kg}\cdot\mathrm{m}^2]$$

Link 2

$$\Sigma_2 = [90, 0, 0]\,[°] \qquad \begin{matrix} {}^2\boldsymbol{p}_{2\to cm_2} = [0, 0.1109, 0.0141] \\ {}^2\boldsymbol{p}_{cm_2\to 3} = [0, 0.0891, -0.0141] \end{matrix}\ [\mathrm{m}]$$

$$m_2 = 2.71\,[\mathrm{kg}] \quad \boldsymbol{I}_2 = \begin{bmatrix} 0.024444 & 0 & 0 \\ 0 & 0.0052508 & 0 \\ 0 & 0 & 0.023995 \end{bmatrix} [\mathrm{kg}\cdot\mathrm{m}^2]$$

Link 3

$$\Sigma_3 = [-90, 0, 0]\,[°] \qquad \begin{matrix} {}^3\boldsymbol{p}_{3\to cm_3} = [0, -0.01628, 0.13379] \\ {}^3\boldsymbol{p}_{cm_3\to 4} = [0, 0.01628, 0.06621] \end{matrix}\ [\mathrm{m}]$$

$$m_3 = 2.5374\,[\mathrm{kg}] \quad \boldsymbol{I}_3 = \begin{bmatrix} -0.012993 & 0 & 0 \\ 0 & -0.01326 & 0 \\ 0 & 0 & 0.004697 \end{bmatrix} [\mathrm{kg}\cdot\mathrm{m}^2]$$

Link 4

$$\Sigma_4 = [-90, 0, 0]\,[°] \qquad \begin{matrix} {}^4\boldsymbol{p}_{4\to cm_4} = [0, -0.10538, 0.01525] \\ {}^4\boldsymbol{p}_{cm_4\to 5} = [0, -0.09462, -0.01525] \end{matrix}\ [\mathrm{m}]$$

$$m_4 = 2.5053\,[\mathrm{kg}] \quad \boldsymbol{I}_4 = \begin{bmatrix} 0.023167 & 0 & 0 \\ 0 & 0.0048331 & 0 \\ 0 & 0 & 0.022751 \end{bmatrix} [\mathrm{kg}\cdot\mathrm{m}^2]$$

Link 5

$$\Sigma_5 = [90, 0, 0]\,[°] \qquad \begin{aligned} {}^5\boldsymbol{p}_{5\to cm_5} &= [0, 0.01566, 0.06489] \\ {}^5\boldsymbol{p}_{cm_5\to 6} &= [0, -0.01566, 0.12511] \end{aligned} \;[\mathrm{m}]$$

$$m_5 = 1.3028\,[\mathrm{kg}] \quad \boldsymbol{I}_5 = \begin{bmatrix} 0.023045 & 0 & 0 \\ 0 & 0.022408 & 0 \\ 0 & 0 & 0.0030151 \end{bmatrix} [\mathrm{kg}\cdot\mathrm{m}^2]$$

Link 6

$$\Sigma_6 = [90, 0, 0]\,[°] \qquad \begin{aligned} {}^6\boldsymbol{p}_{6\to cm_6} &= [0, 0.00283, -0.00228] \\ {}^6\boldsymbol{p}_{cm_6\to 7} &= [0, -0.00283, 0.00228] \end{aligned} \;[\mathrm{m}]$$

$$m_6 = 1.5686\,[\mathrm{kg}] \quad \boldsymbol{I}_6 = \begin{bmatrix} 0.0033636 & 0 & 0 \\ 0 & 0.0029876 & 0 \\ 0 & 0 & 0.0029705 \end{bmatrix} [\mathrm{kg}\cdot\mathrm{m}^2]$$

Link 7

$$\Sigma_7 = [-90, 0, 0]\,[°] \qquad \begin{aligned} {}^7\boldsymbol{p}_{7\to cm_7} &= [0, 0, 0.06031] \\ {}^7\boldsymbol{p}_{cm_7\to ee} &= [0, 0, 0.07569] \end{aligned} \;[\mathrm{m}]$$

$$m_7 = 0.1943\,[\mathrm{kg}] \quad \boldsymbol{I}_7 = \begin{bmatrix} 7.93\times10^{-5} & 0 & 0 \\ 0 & 7.83\times10^{-5} & 0 \\ 0 & 0 & 0.0001203 \end{bmatrix} [\mathrm{kg}\cdot\mathrm{m}^2]$$

A.4 Mass cases of the Chaser spacecraft

Two separate sets of inertial parameters of the base satellite, used inside the virtual models of the free-floating manipulator, are illustrated in this section. They take into account the same masses of the carrier spacecraft although considered its different dimensions and thus different moment of inertia tensors.

A.4.1 Fixed dimensions of the base

The first set of parameters considers the default dimensions of the servicer spacecraft while its mass and its inertia matrix are subjected to variations. The moment of inertia tensors are assumed to be diagonal and equal to that of a solid cuboid.

Case $m_b = 181.025\,\text{kg}$

$$\boldsymbol{p}_{cm_0 \to 1} = [\pm 0.885, -0.012, 0.980]\,[\text{m}]$$

$$m_0 = 181.025\,[\text{kg}] \quad \boldsymbol{I}_0 = \begin{bmatrix} 106.010 & 0 & 0 \\ 0 & 106.010 & 0 \\ 0 & 0 & 91.345 \end{bmatrix} [\text{kg} \cdot \text{m}^2]$$

Case $m_b = 45.256\,\text{kg}$

$$\boldsymbol{p}_{cm_0 \to 1} = [\pm 0.885, -0.012, 0.980]\,[\text{m}]$$

$$m_0 = 45.256\,\text{kg}\,[\text{kg}] \quad \boldsymbol{I}_0 = \begin{bmatrix} 26.510 & 0 & 0 \\ 0 & 26.510 & 0 \\ 0 & 0 & 22.840 \end{bmatrix} [\text{kg} \cdot \text{m}^2]$$

Case $m_b = 11.314\,\text{kg}$

$$\boldsymbol{p}_{cm_0 \to 1} = [\pm 0.885, -0.012, 0.980]\,[\text{m}]$$

$$m_0 = 11.314\,\text{kg}\,[\text{kg}] \quad \boldsymbol{I}_0 = \begin{bmatrix} 6.626 & 0 & 0 \\ 0 & 6.626 & 0 \\ 0 & 0 & 5.709 \end{bmatrix} [\text{kg} \cdot \text{m}^2]$$

Case $m_b = 2.829\,\text{kg}$

$$\boldsymbol{p}_{cm_0 \to 1} = [\pm 0.885, -0.012, 0.980]\,[\text{m}]$$

$$m_0 = 2.829\,\text{kg}\,[\text{kg}] \quad \boldsymbol{I}_0 = \begin{bmatrix} 1.657 & 0 & 0 \\ 0 & 1.657 & 0 \\ 0 & 0 & 1.427 \end{bmatrix} [\text{kg} \cdot \text{m}^2]$$

A.4.2 Variable dimensions of the base

The second set of parameters considers instead the dimensions of the servicer variable with its mass while maintaining the overall density of the spacecraft equal to that of the original, $119.583\,{}^{\text{kg}}/_{\text{m}^3}$. The moment of inertia tensors are assumed to be diagonal and equal to that of a solid cuboid. Furthermore, the principal moments of inertia of a single moment of inertia tensor are assumed to be equal among them, $I_1 = I_2 = I_3$.

Case $m_b = 181.025\,\mathrm{kg}$

$$\boldsymbol{p}_{cm_0\to 1} = [\pm 0.22125, -0.003, 0.6841]\,[\mathrm{m}]$$

$$m_0 = 181.025\,[\mathrm{kg}] \quad \boldsymbol{I}_0 = \begin{bmatrix} 39.7772 & 0 & 0 \\ 0 & 39.7772 & 0 \\ 0 & 0 & 39.7772 \end{bmatrix} [\mathrm{kg}\cdot\mathrm{m}^2]$$

Case $m_b = 45.256\,\mathrm{kg}$

$$\boldsymbol{p}_{cm_0\to 1} = [\pm 0.05531, -7.5\times 10^{-4}, 0.4717]\,[\mathrm{m}]$$

$$m_0 = 45.256\,\mathrm{kg}\,[\mathrm{kg}] \qquad \boldsymbol{I}_0 = \begin{bmatrix} 3.9463 & 0 & 0 \\ 0 & 3.9463 & 0 \\ 0 & 0 & 3.9463 \end{bmatrix} [\mathrm{kg}\cdot\mathrm{m}^2]$$

Case $m_b = 11.314\,\mathrm{kg}$

$$\boldsymbol{p}_{cm_0\to 1} = [\pm 0.01383, -1.9\times 10^{-4}, 0.3378]\,[\mathrm{m}]$$

$$m_0 = 11.314\,\mathrm{kg}\,[\mathrm{kg}] \qquad \boldsymbol{I}_0 = \begin{bmatrix} 0.3915 & 0 & 0 \\ 0 & 0.3915 & 0 \\ 0 & 0 & 0.3915 \end{bmatrix} [\mathrm{kg}\cdot\mathrm{m}^2]$$

Case $m_b = 2.829\,\mathrm{kg}$

$$\boldsymbol{p}_{cm_0\to 1} = [\pm 0.003457, -4.7\times 10^{-5}, 0.2535]\,[\mathrm{m}]$$

$$m_0 = 2.829\,\mathrm{kg}\,[\mathrm{kg}] \quad \boldsymbol{I}_0 = \begin{bmatrix} 3.8856\times 10^{-2} & 0 & 0 \\ 0 & 3.8856\times 10^{-2} & 0 \\ 0 & 0 & 3.8856\times 10^{-2} \end{bmatrix} [\mathrm{kg}\cdot\mathrm{m}^2]$$

B Technical Drawings of the Mockup Models

This appendix contains the technical drawings of the mockup models developed using the 3D mechanical computer-aided design program, SolidWorks. All of them have different characteristics and present increasingly optimized design needed to fulfill the requirements of the new mockup prototype.

The dimensions indicated in figures are all in millimeters. The material used for the models, along with its mass, are specified in figures. For more information about the design process of the models, presented hereafter, see Section 3.4 on page 84.

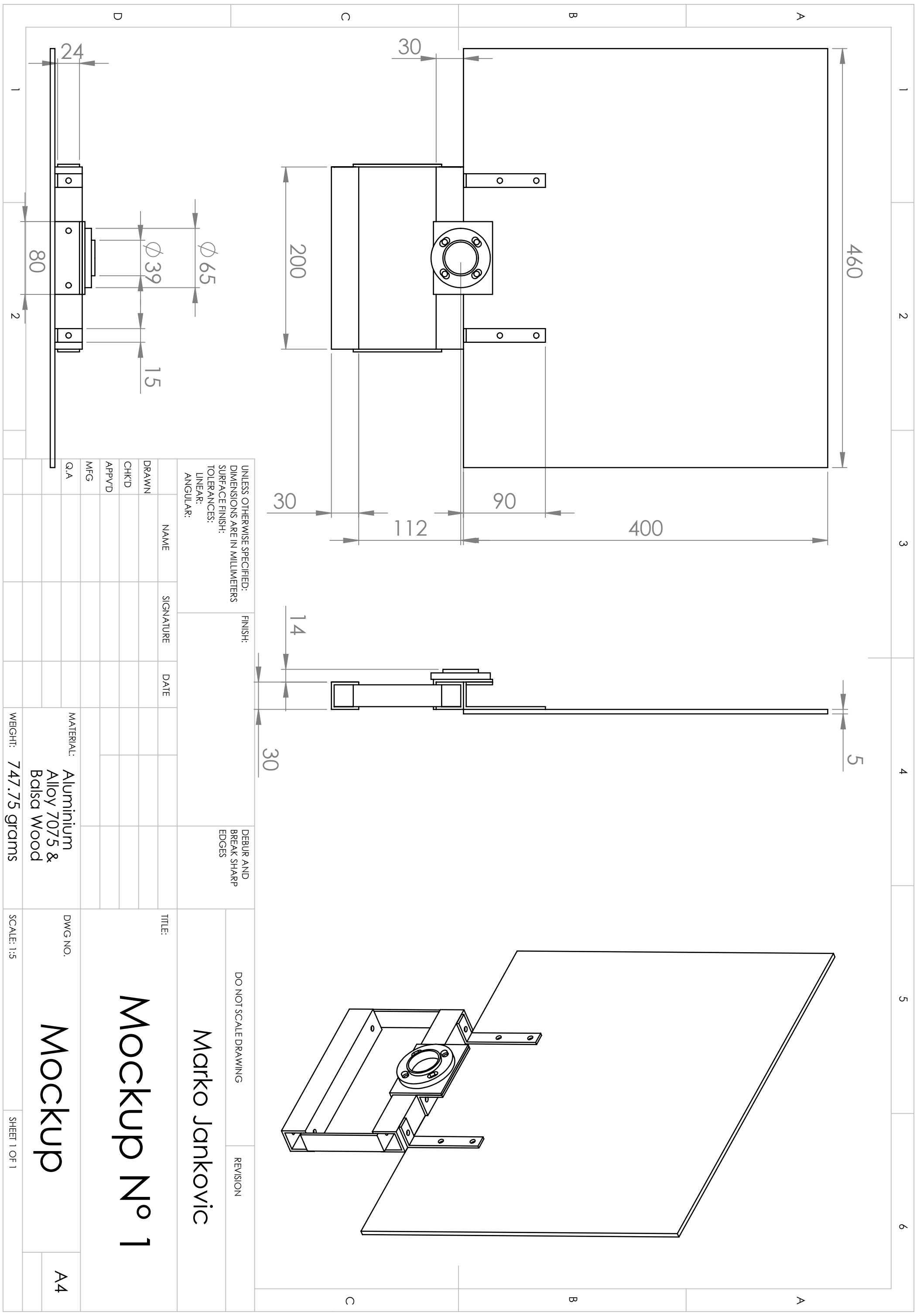

Figure B.1: Wooden model with a single handle

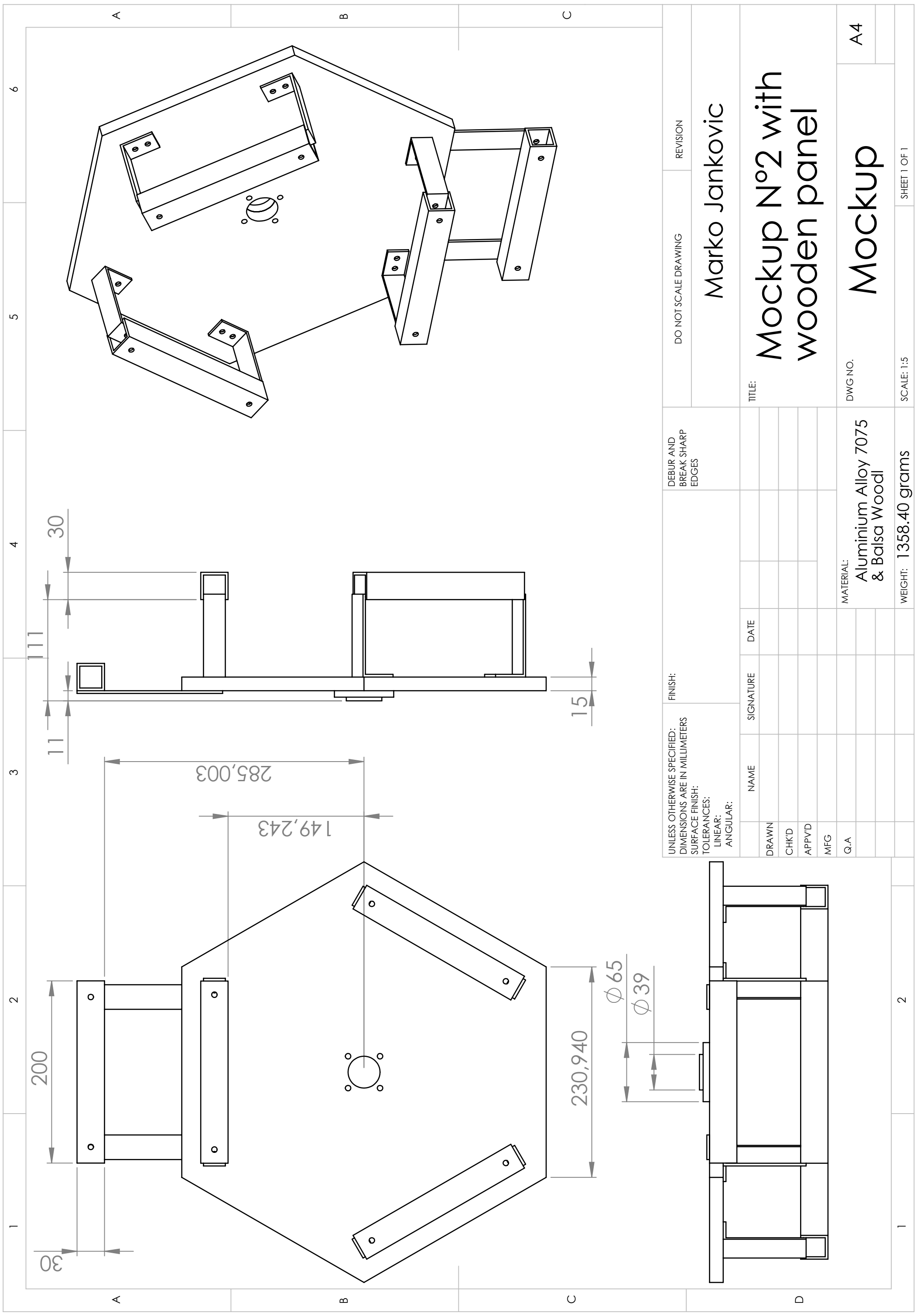

Figure B.2: Wooden model with 4 handles

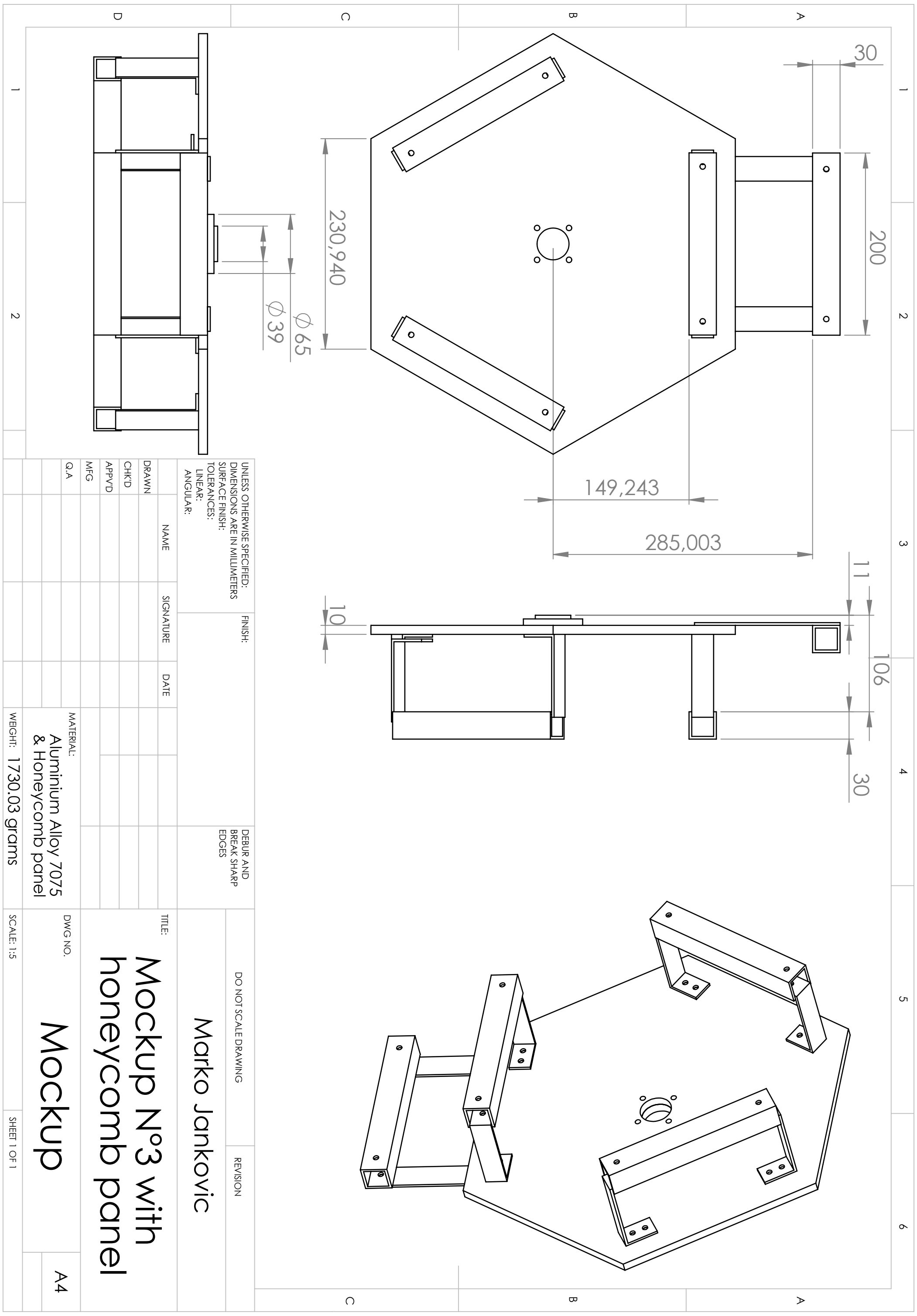

Figure B.3: Honeycomb model with 4 handles

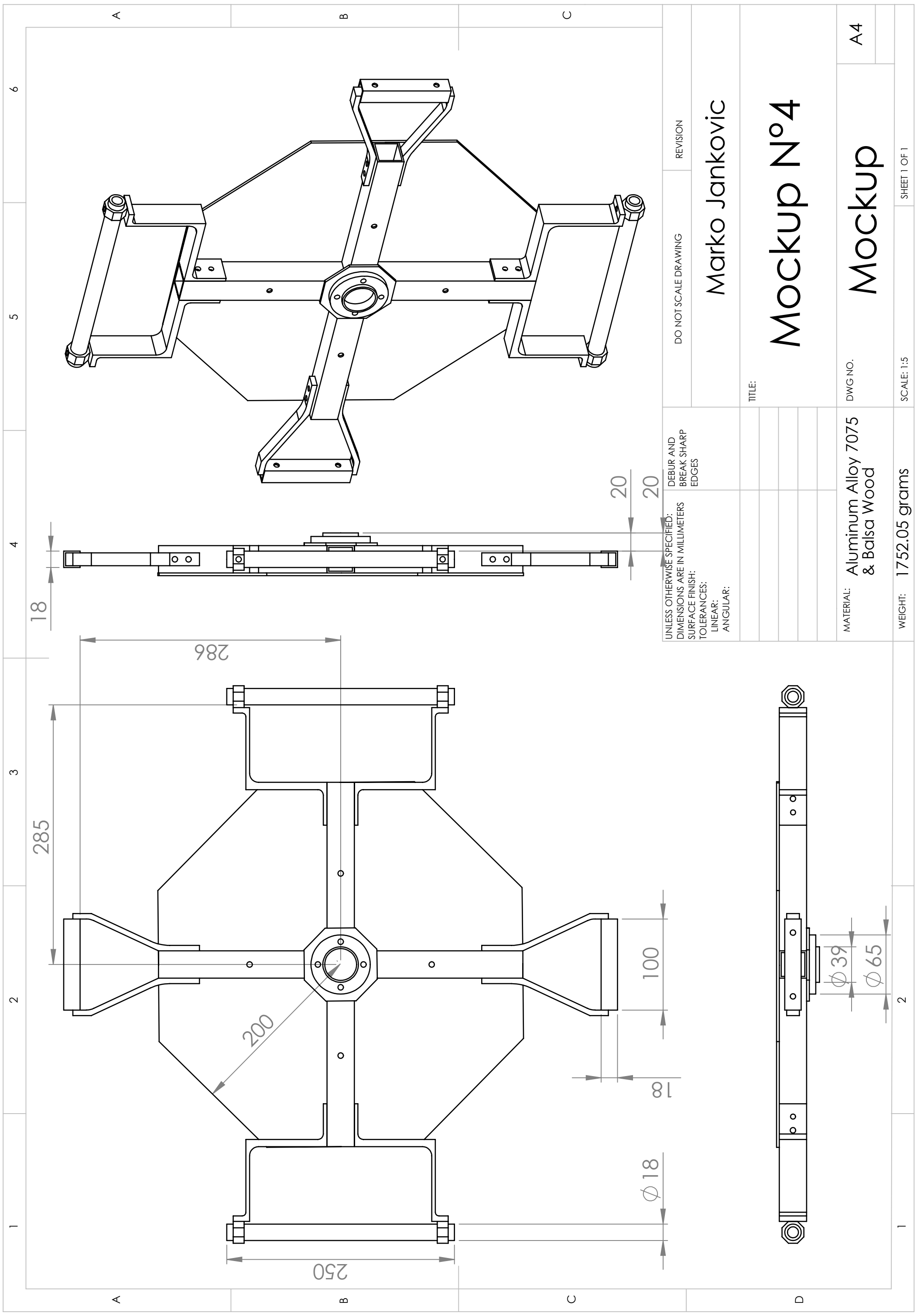

Figure B.4: Aluminum alloy 7075 model with 4 handles

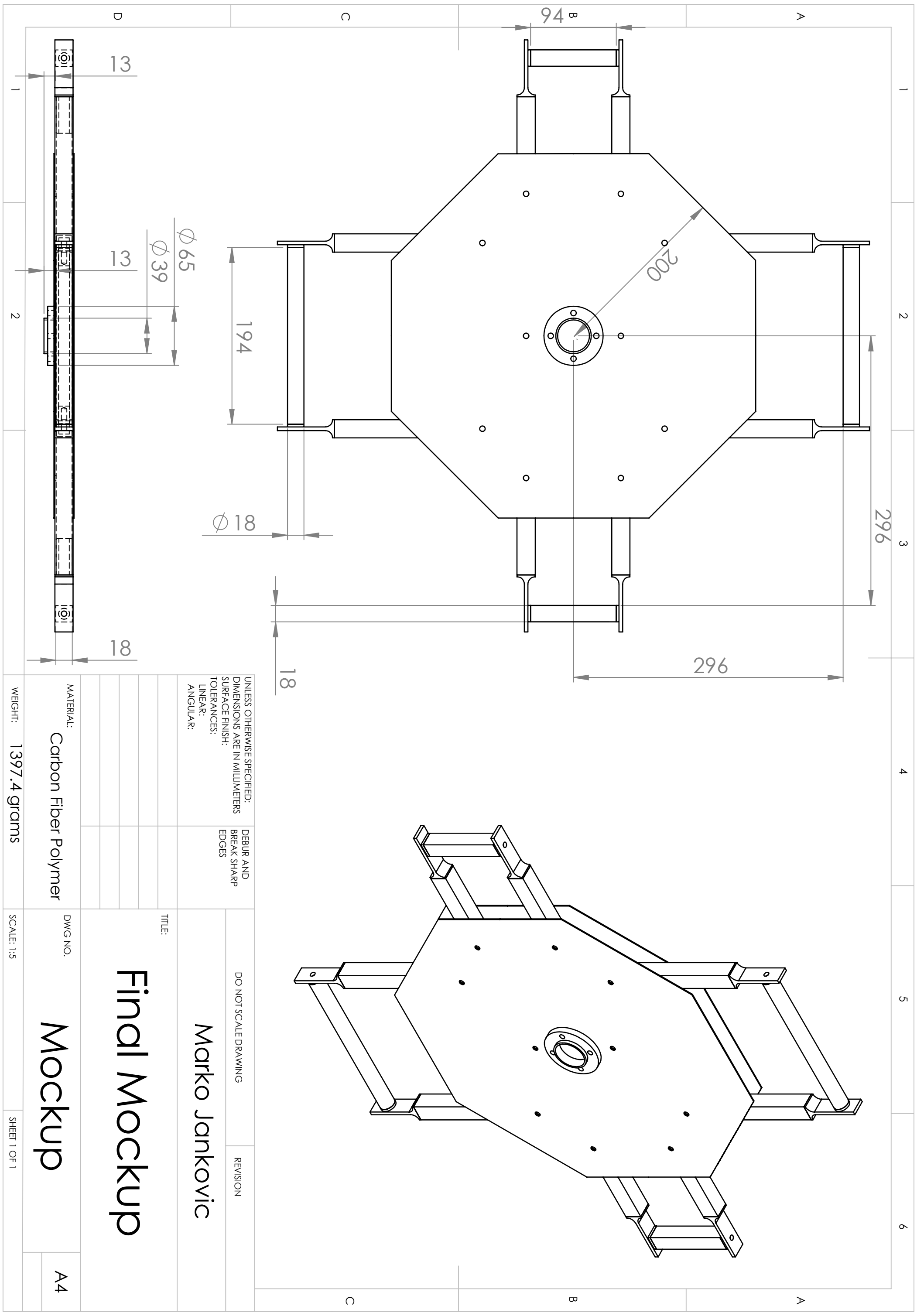

Figure B.5: Final model of the new mockup

C The Handbook of the Hardware-in-the-Loop Simulation Facility

This appendix describes the procedures and the precautions for running the laboratory setup to perform simulations of the approach phase of the DEOS mission. To this end, this chapter is divided in two main sections. Section C.1 outlines the basic rules that an operator should always have in mined, both before and during the activation of the HIL platform. Section C.2 describes in detail the start up procedures of both the robotic system and the PG 70 gripper. Furthermore, this section also contains the necessary procedures to correctly perform: the simulation of the approach phase, the shutdown of the platform and the unfreeze of the platform after an emergency stop of the robotic system.

C.1 Basic Rules

The ground experiment system developed at the DLR IRMC is composed of two LWRs of the third generation capable of exerting large forces and fast movements within their workspace. Therefore, caution should be always exercised during the use of the robotic platform since it has the potential to damage itself and to inflict serious injuries to anyone within its operating area.
Before starting a simulation always have in mind the following rules:

1. **Make sure that nobody or nothing is in the workspace of the robots;**
2. **Make sure that the emergency pedal and the panic button are in the off position.**

During a simulation, on the other hand, the most important thing to remember is to:

1. **Press the panic button to freeze the system in case of any uncertainty.**

After freezing the system, follow the *Freeze recovery procedure* described in Subsection C.2.5 to unfreeze the system and start a new experiment.

C.2 Basic Operating Procedures

C.2.1 Start up procedures of the HIL system

Assuming that the power-off state is the initial state of the system, the procedures needed to start up the simulation facility are the described hereafter.

1. Switch on the main power supply of HIL system (i. e. platform);
2. Make sure that the emergency pedal and the panic button are in the off position;
3. Connect the robots on the emergency box with the emergency pedal and the panic button.
   NOTE: on the emergency box the designation *LBRA* identifies *Robot T* (LWR3*)* while *LBRB* identifies Robot C (LWR4)*;*
4. Repeat the second step;
5. Switch on the electric motors of the desired robot/s;
6. Mount the gripper PG 70 on to LWR3 and the satellite mockup on to LWR4;
7. Log in to the *host* computer;
8. Launch the Terminal form the *host* computer and connect it to the *real-time* computer (named Loki) by running the following command:

   ```
   telnet loki
   ```

9. Check the number of running process on the *real-time* computer by entering the following command inside the Terminal of the *host* computer:

   ```
   ps
   ```

   and proceed according to the following:

   a) if just one process is present continue with the start up procedure;

b) if more running processes are present:

i. disconnect the *host* computer from the *real-time* computer by closing the Terminal;

ii. switch off the main power supply of the platform;

iii. repeat the start up procedure from the first step.

10. Open the Academic version of MATLAB on the *host* computer;

11. Open the user interface of the system, i. e. the Simulink model *HMI2010*, and compile it for the *real-time* computer, using the key binding Control-B or the menu Tools ▷ Code Generation ▷ Build Model ;

12. Load the compiled *HMI2010* model in to the *real-time* computer (menu Tools ▷ Starting HMI2010 on 'loki');

13. Verify that the only active process on the *real-time* computer is the loaded model (see 8. step);

14. Change the simulation mode of the *HMI2010* Simulink model from Normal to External (menu Simulation ▷ External);

15. Connect the model opened on the *host* computer with the one loaded into the *real-time* computer (menu Simulation ▷ Connect to target or Tools ▷ External Mode Control Panel ▷ Connect).

C.2.2 Start up procedure of the PG 70 gripper

The correct procedure to start up the PG 70 gripper, assuming that it was previously switched off, is described in detail hereafter.

1. Switch on the current and the voltage on the external power supply unit of the gripper;

2. Make sure that the values of the current and voltage of the *master* are 0.2 mA and 24 V, respectively, while those of the *slave* are 0.4 mA and 24 V, respectively;

3. Open the Academic version of MATLAB on the *host* computer;

4. Open the user interface of the gripper, i. e. the Simulink model *gripper*, that is located in the directory having the following path: /volume/USERSTORE-/tplab/entwicklung/artigas/gripper;

NOTE: it is not necessary to compile the model for the *real-time* computer since the indicated directory already contains its compiled version.

5. Enter the following terminal commands in to a new terminal window to load the necessary libraries in to the *real-time* computer:

```
telnet loki
module load /lib/modules/gripper.out.0.0.1
C gripperlosRegister
grippercontrol -a "-f /home/rtosvx/public
/SchunkGripperPG70Force.xml -fbc -snarfgei1"
grippercontrol -r
```

6. Load the compiled *gripper* model in to the *real-time* computer (menu Tools ▷ Starting gripper on 'loki');
   Otherwise enter the following terminal commands in to a new terminal window to load the compiled *gripper* model in to the *real-time* computer:

```
telnet loki
cd /volume/USERSTORE/tplab/entwicklung/artigas/gripper
./gripper.vxe
```

7. Change the simulation mode of the *gripper* Simulink model from Normal to External (menu Simulation ▷ External);

8. Connect the model opened on the *host* computer with the one loaded in to the *real-time* computer (menu Simulation ▷ Connect to target or Tools ▷ External Mode Control Panel ▷ Connect);

C.2.3 Approach phase simulation

1. Perform the 2. step of Subsection C.2.1;

2. Impose the initial configuration to the robots.

   a) To achieve this automatically, at first select the demo No. 2 (*Trapezoidal Interpolator*) with the Demo Selector of *HMI2010* model. Than, press the emergency pedal and release the panic button to start the demo;
   NOTE: the panic button must always be in the hands of the operator during the motion of the robots; in case of emergency press the panic button to freeze the system;

   b) To achieve this manually, at first select the demo No. 1(*Gravity Compensation*) with the Demo Selector of *HMI2010* model. Than, make sure that the vectors $\left[m, {}^{7}\boldsymbol{p}_{cg}\right]^{T} \in \mathbb{R}^{4\times 1}$ of the tools are equivalent to those effectively mounted on to the robots. Finally connect one robot at the time to the emergency pedal and the panic button (see 3. step of Subsection C.2.1) and change manually its configuration.

3. Stop the demo by pressing the panic button and by releasing the emergency pedal;

4. Select the demo No. 4 (*DEOS Simulator*);

5. Open the scopes of the robots and proceed according to the following:

   a) if the values of the scale appear enormous reset the scale of the scopes by pressing the Autoscale button;

   b) if one of the magnitudes of the *torque error* vector ($\in \mathbb{R}^{7\times 1}$) of LWR4 presents a value higher than $1\,\mathrm{N}\cdot\mathrm{m}$ reset the sensors of the LWR4 robot. To reset the sensors go to HMI2010 ▷ demos ▷ demo 4 ▷ demo GUI scopes and parameters and reset the two upper switches;

6. Perform the 2. step of Subsection C.2.1;

7. Repeat the 5. step;

8. Start the simulation by releasing the panic button and by pressing the emergency pedal.
   NOTE: the panic button must always be in the hands of the operator during a simulation; in case of emergency press the panic button to freeze the system.

9. Stop the simulation by pressing the panic button and by releasing the emergency pedal;

C.2.4 Shut down procedures

1. Perform the first three steps of Subsection C.2.3;

2. Power off the external power supply unit of the gripper;

3. Disconnect the robots on the emergency box with the pedal and the panic button;

4. Switch off the electric motors of the robots;

5. Unmount the gripper and the mockup from the robots;
6. Disconnect the *host* computer from the *real-time* computer by closing all opened terminal windows;
7. Close the *HMI2010* and *gripper* Simulink models on the *host* computer;
8. Close the Academic version of MATLAB on the *host* computer;
9. Log out from the *host* computer;
10. Switch off the main power supply of HIL system.

C.2.5 Freeze recovery procedures

This procedure assumes that the platform was frozen by pressing the panic button and by releasing the emergency pedal.

1. If the reason of the emergency stop of the platform was the lockup of the *real-time* computer (which most often occurs before even starting the desired demo):
   a) disconnect the *host* computer from the *real-time* computer by closing all opened terminal windows;
   b) switch off the main power supply of the platform;
   c) start over the start up procedures described in Subsection C.2.1 and in Subsection C.2.2. Obviously, skip the unnecessary steps (e. g. the 3. or the 6. step of Subsection C.2.1) if they were already performed before the lockup of the *real-time* computer.
2. If the reason of the emergency stop of the platform was something else occurred during the approach simulation, to start a new one perform, from the beginning, the procedure described in Subsection C.2.3.

Bibliography

[1] Jamshid Gaziyev, UNOOSA. (2009, July) Space debris: Orbiting debris threatens sustainable use of outer space. [Online]. Available: http://www.un.org/en/events/tenstories/08/spacedebris.shtml

[2] Space Debris Office, ESA. (2009, February) Space Debris. [Online]. Available: http://www.esa.int/SPECIALS/Space_Debris/index.html

[3] J.-C. Liou and N. Johnson, "Instability of the present LEO satellite populations," *Advances in Space Research*, vol. 41, no. 7, pp. 1046 – 1053, 2008. [Online]. Available: http://www.sciencedirect.com/science/article/pii/S0273117707004097

[4] J.-C. Liou and N. L. Johnson, "A sensitivity study of the effectiveness of active debris removal in LEO," *Acta Astronautica*, vol. 64, no. 2-3, pp. 236 – 243, 2009. [Online]. Available: http://www.sciencedirect.com/science/article/pii/S0094576508002634

[5] J.-C. Liou, N. Johnson, and N. Hill, "Controlling the growth of future LEO debris populations with active debris removal," *Acta Astronautica*, vol. 66, no. 5-6, pp. 648 – 653, 2010. [Online]. Available: http://www.sciencedirect.com/science/article/pii/S0094576509003981

[6] D. VanBeber and W. Keyzer. (2011, March) Intelsat Picks MacDonald, Dettwiler and Associates Ltd. for Satellite Servicing. [Online]. Available: http://www.mdacorporation.com/corporate/news/pr/pr2011031501.cfm

[7] S. Dubowsky, W. Durfee, T. Corrigan, A. Kuklinski, and U. Muller, "A laboratory test bed for space robotics: the VES II," in *Intelligent Robots and Systems '94. 'Advanced Robotic Systems and the Real World', IROS '94. Proceedings of the IEEE/RSJ/GI International Conference on*, vol. 3, September 1994, pp. 1562 –1569 vol.3.

[8] S. Agrawal, G. Hirzinger, K. Landzettel, and R. Schwertassek, "A new labo-

ratory simulator for study of motion of free-floating robots relative to space targets," *Robotics and Automation, IEEE Transactions on*, vol. 12, no. 4, pp. 627 –633, August 1996.

[9] W. Xu, B. Liang, Y. Xu, C. Li, and W. Qiang, "A Ground Experiment System of Free-floating Robot For Capturing Space Target," *Journal of Intelligent and Robotic Systems*, vol. 48, pp. 187–208, 2007. [Online]. Available: http://dx.doi.org/10.1007/s10846-006-9087-8

[10] M. D. Stefano, "Motion analysis of a free-tumbling satellite and experimentation of the grasping task with two fixed-base LWR robots," Deutsches Zentrum für Luft- und Raumfahrt e.V., Tech. Rep. DLR IB 572-12-05, 2012.

[11] D. J. Kessler and B. G. Cour-Palais, "Collision frequency of artificial satellites: The creation of a debris belt," *Journal of Geophisical Research*, vol. 83, no. A6, pp. 2637– 2646, June 1978.

[12] D. Rex, "Will space run out of space? The orbital debris problem and its mitigation," *Space Policy*, vol. 14, no. 2, pp. 95 – 105, 1998. [Online]. Available: http://www.sciencedirect.com/science/article/pii/S0265964698000046

[13] N. L. Johnson, E. Stansbery, J.-C. Liou, M. Horstman, C. Stokely, and D. Whitlock, "The characteristics and consequences of the break-up of the Fengyun-1C spacecraft," *Acta Astronautica*, vol. 63, no. 1-4, pp. 128 – 135, 2008. [Online]. Available: http://www.sciencedirect.com/science/article/pii/S0094576507003281

[14] J.-C. Liou, "An Updated Assessment of the Orbital Debris Environment in LEO," *The Orbital Debris Quarterly News (ODQN)*, vol. Volume 14, no. 1, pp. 7–8, January 2010.

[15] M. H. Kaplan, "Space Debris Realities and Removal," Space Department Applied Physics Laboratory, 11100 Johns Hopkins Road Laurel, MD 20723-6099, Tech. Rep., May 2010.

[16] Orbital Debris Program Office, NASA. (2009, July) Orbital Debris Research at NASA . [Online]. Available: http://orbitaldebris.jsc.nasa.gov/index.html

[17] "Space Debris," The Parliamentary Office of Science and Technology, 7 Millbank, London SW1P 3JA, POST Note 355, March 2010.

[18] J.-C. Liou, "Project Review: An Update on LEO Environment Remediation

with Active Debris Removal," *The Orbital Debris Quarterly News (ODQN)*, vol. 15, no. 2, pp. 4–6, April 2011.

[19] B. Siciliano, L. Sciavicco, L. Villani, and G. Oriolo, *Robotics: Modelling, Planning and Control*, ser. Advanced textbooks in control and signal processing. Springer, 2009, ch. Introduction, p. 1.

[20] B. Siciliano and O. Khatib, *Springer Handbook of Robotic*. Springer, 2008, ch. Introduction, p. 1. [Online]. Available: http://www.springerlink.com/content/978-3-540-23957-4/

[21] D. Reintsema, K. Landzettel, and G. Hirzinger, "DLR's Advanced Telerobotic Concepts and Experiments for On-Orbit Servicing," in *Advances in Telerobotics*, ser. Springer Tracts in Advanced Robotics, M. Ferre, M. Buss, R. Aracil, C. Melchiorri, and C. Balaguer, Eds. Springer Berlin / Heidelberg, 2007, vol. 31, pp. 323–345. [Online]. Available: http://dx.doi.org/10.1007/978-3-540-71364-7_20

[22] K. Yoshida, "Achievements in space robotics," *Robotics Automation Magazine, IEEE*, vol. 16, no. 4, pp. 20 –28, december 2009.

[23] K. Yoshida and B. Wilcox, *Springer Handbook of Robotic*. Springer, 2008, ch. Space Robots and Systems, pp. 1031–1063. [Online]. Available: http://www.springerlink.com/content/978-3-540-23957-4/

[24] Brian Dunbar, NASA. Facts and Figures. [Online]. Available: http://www.nasa.gov/mission_pages/station/main/onthestation/facts_and_figures.html

[25] Space Systems Laboratory, University of Maryland. (2005, January) Dexterous Robotics at the Space Systems Laboratory. [Online]. Available: http://robotics.ssl.umd.edu/ranger/

[26] A. Ellery, J. Kreisel, and B. Sommer, "The case for robotic on-orbit servicing of spacecraft: Spacecraft reliability is a myth," *Acta Astronautica*, vol. 63, no. 5-6, pp. 632 – 648, 2008. [Online]. Available: http://www.sciencedirect.com/science/article/pii/S0094576508001197

[27] H. Ueno, S. Dubowsky, C. Lee, C. Zhu, Y. Ohkami, S. Matsumoto, and M. Oda, "Space Robotic Mission Concepts for Capturing Stray Objects," in *Proceedings of the 23rd International Symposium on Space Technology and Science*, Matsue, Japan, May 2002.

[28] F. Sellmaier, T. Boge, J. Spurmann, S. Gully, T. Rupp, and F. Huber, "On-Orbit Servicing Missions: Challenges and Solutions for Spacecraft Operations," in *SpaceOps 2010 Conference*. Huntsville, Alabama, USA: AIAA, April 25-30 2010.

[29] T. Rupp, T. Boge, R. Kiehling, and F. Sellmaier, "Flight Dynamics Challenges of the German On-Orbit Servicing Mission DEOS," in *21st International Symposium on Space Flight Dynamics*, Toulouse, France, September 28-October 2 2009.

[30] Institute of Robotics and Mechatronics, DLR. TECSAS/DEOS. [Online]. Available: http://www.dlr.de/rm/en/desktopdefault.aspx/tabid-3825/5963_read-8759/

[31] R. Lampariello and G. Hirzinger, "Freeflying robots-Inertial Parameter Identification and Control Strategies," in *ESA Workshop on Advanced Space Technologies for Robotics and Automation (ASTRA 2000)*. ESA/ESTEC, Noordwijk, Netherlands: ESA, December 2000.

[32] P. Rank, Q. Mühlbauer, W. Naumann, and K. Landzettel, "The DEOS Automation and Robotics Payload," in *11th Symposium on Advanced Space Technologies in Robotics and Automation, 12-14 April 2011*. ESA/ESTEC, Noordwijk, Netherlands: ESA, April 2011.

[33] Institute of Robotics and Mechatronics, DLR. Telepresence. [Online]. Available: http://www.dlr.de/rm/en/desktopdefault.aspx/tabid-5014/8373_read-14285/

[34] F. Cusumano, R. Lampariello, and G. Hirzinger, "Development of teleoperation control for a freefloating robot during the grasping of a tumbling target," in *International Conference on Intelligent Manipulation and Grasping*, Genoa, Italy, July 1-2 2005.

[35] U. Hillenbrand and R. Lampariello, "Motion and parameter estimation of a freefloating space object from range data for motion prediction," in *8th International symposium on Artificial Intelligence, Robotics and Automation in Space (iSAIRAS 2005)*, Munich, Germany, September 5-9 2005.

[36] R. Lampariello and G. Hirzinger, "Modeling and experimental design for the on-orbit inertial parameter identification of free-flying space robots," in *ASME 2005 International Design Engineering Technical Conferences and Computers Information in Engineering Conference*, Long Beach, California,

USA, September 24-28 2005.

[37] S. Abiko, R. Lampariello, and G. Hirzinger, “Impedance control for a freefloating robot in the grasping of a tumbling target with parameter uncertainty,” in *IEEE/RSJ International Conference on Intelligent Robots and Systems 2006 (IROS 06)*, Beijing, China, October 2006.

[38] E. G. Papadopoulos, *Nonholonomic Behavior in Free-floating Space Manipulators and its Utilization.* Kluwer Academic Publishers, 1993, pp. 423–445.

[39] J. Schwartz, M. Peck, and C. Hall, “Historical Review of Air-Bearing Spacecraft Simulators,” *Journal of Guidance, Control, and Dynamics*, vol. 26, no. 4, pp. 513–522, August 2003.

[40] Space Systems Laboratory, University of Maryland. (2007) Facilities at the Space Systems Lab. [Online]. Available: http://www.ssl.umd.edu/html/facilities.html

[41] Human Spaceflight Research Office, ESA. (2011) Parabolic flights. [Online]. Available: http://www.esa.int/esaMI/HSF_Research/SEMU945XT9G_0.html

[42] Linda C. Elonen-Wright. (2008, January) Zero Gravity Research Facility. [Online]. Available: http://facilities.grc.nasa.gov/zerog/index.html

[43] C. Menon, S. Busolo, S. Cocuzza, A. Aboudan, A. Bulgarelli, C. Bettanini, M. Marchesi, and F. Angrilli, “Issues and solutions for testing freeflying robots,” *Acta Astronautica*, vol. 60, no. 12, pp. 957 – 965, 2007. [Online]. Available: http://www.sciencedirect.com/science/article/pii/S0094576506004279

[44] Y. Xu, J. Brown, H.B., M. Friedman, and T. Kanade, “Control system of the self-mobile space manipulator,” *Control Systems Technology, IEEE Transactions on*, vol. 2, no. 3, pp. 207 –219, September 1994.

[45] W. Xu, B. Liang, and Y. Xu, “Survey of modeling, planning, and ground verification of space robotic systems,” *Acta Astronautica*, vol. 68, no. 11-12, pp. 1629 – 1649, 2011. [Online]. Available: http://www.sciencedirect.com/science/article/pii/S0094576510004352

[46] T. Boge and O. Ma, “Using advanced industrial robotics for spacecraft Rendezvous and Docking simulation,” in *Robotics and Automation (ICRA), 2011 IEEE International Conference on*, May 2011, pp. 1–4.

[47] J. Peraire and S. Widnall, "3D Rigid Body Dynamics: Tops and Gyroscopes," On-line, July 2009.

[48] E. Butikov, "Precession and nutation of a gyroscope," *European Journal of Physics*, vol. 27, no. 5, p. 1071, 2006. [Online]. Available: http://stacks.iop.org/0143-0807/27/i=5/a=006

[49] E. Merritt, "The Trace of the Gyroscopic Pendulum," *Phys. Rev. (Series I)*, vol. 4, pp. 336–343, Jan 1897. [Online]. Available: http://link.aps.org/doi/10.1103/PhysRevSeriesI.4.336

[50] O. Ma, J. Wang, S. Misra, and M. Liu, "On the Validation of SPDM Task Verification Facility," *Journal of Robotic Systems*, vol. 21, no. 5, pp. 219–235, 2004. [Online]. Available: http://dx.doi.org/10.1002/rob.20011

[51] T. Hulin, M. Sagardia, J. Artigas, S. Schaetzle, P. Kremer, and C. Preusche, "Human-Scale Bimanual Haptic Interface," in *5th International Conference on Enactive Interfaces*, Pisa, Italy, September 2008.

[52] Institute of Robotics and Mechatronics, DLR. Light-Weight Robots. [Online]. Available: http://www.dlr.de/rm/en/desktopdefault.aspx/tabid-3803/

[53] B. Siciliano, L. Sciavicco, L. Villani, and G. Oriolo, *Robotics: Modelling, Planning and Control*, ser. Advanced textbooks in control and signal processing. Springer, 2009, ch. Differential Kinematics and Statics, pp. 124–126.

[54] J. Artigas, P. Kremer, C. Preusche, and G. Hirzinger, "Testbed for telepresent on-orbit satellite servicing," in *Proceedings of the Human-Centered Robotic Systems Conference (HCRS)*. Munich, Germany: Institute of Robotics and Mechatronics, German Aerospace Center (DLR), 2006.

[55] E. Stoll, U. Walter, J. Artigas, C. Preusche, P. Kremer, G. Hirzinger, J. Letschnik, and H. Pongrac, "Ground verification of the feasibility of telepresent on-orbit servicing," *J. Field Robot.*, vol. 26, pp. 287–307, March 2009. [Online]. Available: http://dl.acm.org/citation.cfm?id=1527169.1527173

[56] (2012) 2-finger parallel grippers. [Online]. Available: http://goo.gl/m1rnD

[57] K. Yoshida, "The SpaceDyn: a MATLAB toolbox for space and mobile robots," in *Intelligent Robots and Systems, 1999. IROS '99. Proceedings. 1999 IEEE/RSJ International Conference on*, vol. 3, 1999, pp. 1633 –1638

vol.3.